

**Synthesis and Functional Applications of  
Highly Photocatalytic TiO<sub>2</sub> Based Surfaces:  
Al/TiO<sub>2</sub> and Au/TiO<sub>2</sub> Hybrid Structures**

Dissertation

zur Erlangung des akademischen Grades

Doktor der Ingenieurwissenschaften

(Dr.-Ing.)

der Technischen Fakultät

der Christian-Albrechts-Universität zu Kiel

**MUHAMMAD ZUBAIR GHORI**

Kiel, Germany

31-07-2018

1. Gutachter: Assoc. Prof. Dr. Oral Cenk Aktas / Prof. Dr. Franz Faupel

2. Gutachter: Prof. Dr. Lorenz Kienle

Tag des Kolloquiums: 31-07-2018

*to Annika and my whole family...*

# ACKNOWLEDGEMENT

At this point, I would like to thank all the people who contributed in some way to accomplish this dissertation and made it an unforgettable experience for me.

Firstly, I would like to express my deepest gratitude to **Prof. Dr. Franz Faupel** for his fundamental role during my doctoral study. He gave me the chance to join his research group and believed in me right from the start. I am very grateful for his support and patience throughout my PhD work. It would be impossible for me to overcome all hurdles without his supervision and guidance. His appreciation upon my small achievements, encouragement during hard times and his humble nature has built a trust between us and motivated me to perform even in more better way. Without his supervision it would not be possible to accomplish this dissertation. I have had a great experience in the last seven years and it is an honor for me to be a part of his group.

I owe a very important debt to **Assoc. Prof. Dr. Oral Cenk Aktas** for the support of my PhD study and related research, for his patience and motivation. He has been a tremendous mentor for me. His guidance helped me all the time in research and writing this thesis. The joy and enthusiasm he has for the research was contagious and motivational for me, even during tough times in the PhD pursuit. His broad vision, knowledge and critical comments developed my insight to let me grow as a research scientist. As my mentor he has taught me more than I could ever give him credit for here. He has shown me by his example what a good scientist should be. I would also like to thank him for his friendship, empathy, and great sense of humor. I am extending my deepest thanks to his family for their acceptance and patience during the time we spent especially on weekends and holidays for research work and thesis preparation.

I would particularly like to thank **Dr. Oleksandr Polonskyi** for his generous support especially during the initial stage of my PhD study. Discussions with him illuminated ideas and improved my technical knowledge during the research. Due to his expertise and valuable time I could learn GAS setup and XPS analysis more deeply. He was always there for me whenever I needed some help in troubleshooting the sputter setup and additional analytical tools. I would also like to thank him for supporting me in the PhD scholarship application.

I greatly appreciate the support of **Dr. Thomas Strunskus** for his encouragement, immense knowledge, fruitful suggestions and persistent help to complete this PhD period.

Without his remarkable problem-solving ideas and strategical planning, it would have been hard for me to stay at this position.

A special thanks to **Prof. Dr. Klaus Rätzke** for his counseling (as an experienced man), wide-ranging discussions, safety instructions for lab and his great sense of humor.

Special thanks to **Dr. Jian Xiong** (Department of chemistry and chemical engineering, Hubei University of Technology, China) for supervising my successful master thesis study. I am grateful to him for introducing me to the sputtering system and other analytical techniques.

I would like to acknowledge my PhD fellow and friend **Salih Veziroglu**. Thanks for the pleasant joint work on photocatalysis, beneficial discussions and sharing ideas for improving our results during the last year. It was fun to spend the free time together especially while playing kicker (together with Cenk). Also, here thanks go to my office colleague **Brook Shurtleff** for theoretical discussions and coffee breaks.

I thank **Dipl.-Ing. Stefan Rehders** for providing technical support and assistance whenever it was needed. Besides, I would like to thank **Dipl.-Inf. Peter Sommer** for providing nice IT service and skills.

The TEM studies in this dissertation were performed by Alexander Martin Hinz and Marius Kamp (from the research group of Synthesis and Real structure of Prof. Dr. Lorenz Kienle) and I would like to thank them for their support and analysis.

Electrochemical simulations and Helium ion microscopy results used in this thesis work were performed by Assoc. Prof. Dr. Jost Adam and Assoc. Prof. Dr. Jacek Fiutowski, respectively (from the Mads Clausen Institute, NanoSYD, University of Southern Denmark). I would like to thank them for this great collaborative work with our research group.

I am also very gratified to Mohammad Emami, Khurram Saleem, Maximilian Burk, Anna Lena Obermann and Majid Hussain for their support in my experimental work. I wish them all the best for their private and professional future life.

I am enormously thankful to my recent and former colleagues of the chair of multicomponent materials (Stefan Schröder, Alexander Vahl, Alexander Martin Hinz, Sebastian Zabel, Christian Ohrt, Igor Barg, Ron-Marco Friedrich, Wiebke Reichstein, Benjamin Spetzler, Niko Carstens, Jonas Drewes, Jingxian Su and others). My special

thanks go to Stefan Schröder, Alexander Martin Hinz and Alexander Vahl for their contributions, help and nice discussions about scientific topics and beyond.

I would like to express my thanks to Dr. Victor Kaidas and Sindu Shree for introducing me to Raman Spectroscopy system.

Also, a special thanks to Dr. Mark Daniel Gerngroß for introducing SEM and giving me support when there was any problem. Thanks to him and his wife Melike for their friendship and nice gatherings. We had a lot of fun together.

Specially, I would like to acknowledge Graduate Center and Federal State Funding CAU Kiel for providing funding for my PhD study.

Finally, I would like to thank the most important persons in my life, my parents and sisters for their endless love, motivation, support and trust in my skills. Words cannot express how thankful I am that they provided me the opportunity to come to Germany for higher studies and handling this distance between us. I love and miss them a lot. My discrete gratitude goes to my fiancée Annika, for her love, friendship, support, patience and confidence in me. Also, her parents who accepted me as a member of their family and helped me a lot whenever I needed them. We always enjoyed celebrating festivals and holidays together. I am happy to be the part of this family.

# ABSTRACT

The interest in using heterogeneous photocatalysis as an alternative for environmental clean-up is continuously increasing as the water resources diminish enormously and the air pollution threatens human health seriously. TiO<sub>2</sub> is one of the mostly preferred material for heterogeneous photocatalysis due to its inertness, non-toxicity, high photocatalytic activity, recyclability and safety towards humans and nature. This dissertation covers the development of TiO<sub>2</sub> based highly photocatalytic thin films and their functional applications.

This thesis is composed of **9 Chapters**: Following *Introduction* (**Chapter 1**) and *Theory* (**Chapter 2**), *Methods* and *Experimental* processes are described in **Chapter 3** and **Chapter 4**, respectively. The *Results and Discussion*, which are originally based on peer-reviewed three publications, are presented in corresponding three chapters (**Chapters 5, 6 and 7**).

**Chapter 5 (based on Publication 1)** presents the preparation of highly active columnar TiO<sub>2</sub> nanostructures by pulsed DC magnetron sputtering. A systematic study (thermally induced crack networks and thickness control) was carried out to optimize the photocatalytic performance of deposited TiO<sub>2</sub> films. In addition to the preparation of TiO<sub>2</sub> thin films, a special attention was given to develop a proper analytic approach to reveal photocatalytic reactions occurring directly at the TiO<sub>2</sub> film surface (rather than the indirect analysis of the photocatalysis by observing decolorization of an aqueous dye solution used as model pollutant). An ultra-fast and reliable analysis method was introduced and compared with the standard analysis method (DIN 52980:2008-10). By the proposed approach first time both, reversible (conversion to colorless Leuco-Methylene Blue) and irreversible bleaching of Methylene Blue by TiO<sub>2</sub> have been quantified without using any stabilizer or sacrificial electron donor (SED).

**Chapter 6 (based on Publication 2)** covers development of Al/TiO<sub>2</sub> hybrid ultrathin film which exhibits superior photocatalytic performance. By introducing controlled amount of oxygen in Gas Aggregation Source (GAS), plasmonic aluminum (Al) nanoparticles with controlled size and crystallinity were achieved. While partial oxidation of the Al target produces stable oxygen containing seeds upon sputtering that triggered nucleation of Al nanoparticles, the ultrathin oxide layer covering Al nanoparticles protected them from further excessive oxidation. TiO<sub>2</sub> layers decorated with Al nanoparticles with primary

particle size of 20-25 nm led to much higher photocatalytic activity (95-100 %) in comparison to pristine TiO<sub>2</sub> (35-40 %).

**Chapter 7 (based on Publication 3)** focuses on the use of highly active TiO<sub>2</sub> thin films for photocatalytic deposition of high aspect ratio sharp gold (Au) nanoneedles, which can be interesting for various applications including energy harvesting, medical field as well as cell surface interaction and SERS biomolecules sensing applications. The loading of Au on TiO<sub>2</sub> film was achieved by the reduction of Au<sup>+3</sup> ions directly on the TiO<sub>2</sub> film surface via a novel photocatalytic reduction process (surfactant free). In addition to the typical photochemical loading of Au on TiO<sub>2</sub>, here patterning of Au structures on TiO<sub>2</sub> film was also demonstrated by selective activation of TiO<sub>2</sub> surface and reduction of Au structures on these active areas directly without additional lithographic processes.

Finally, a synoptic conclusion has been given to drive a general *Summary* (**Chapter 8**) and an *Outlook* (**Chapter 9**) is provided for future research activities.



# Kurzfassung

Das Interesse heterogene Photokatalyse als Alternative für die Beseitigung von Umweltbelastungen zu nutzen, steigt kontinuierlich an, da die Wasserressourcen schrumpfen und die Luftverschmutzung eine ernsthafte Bedrohung für die menschliche Gesundheit darstellt.  $\text{TiO}_2$  ist eines der bevorzugtesten Materialien für die heterogene Photokatalyse, dank seiner Inertheit, Ungiftigkeit, hohen photokatalytischen Aktivität, Wiederverwertbarkeit und Sicherheit gegenüber Mensch und Natur. Diese Dissertation umfasst die Entwicklung von auf  $\text{TiO}_2$  basierenden, photokatalytisch hochaktiven Dünnschichten und ihre funktionellen Anwendungen.

Diese Thesis ist aus **9 Kapiteln** zusammengesetzt: Nach der *Einführung* (**Kapitel 1**) und *Theorie* (**Kapitel 2**), werden die *Methoden* und *experimentellen* Prozesse in **Kapitel 3** bzw. **Kapitel 4** beschrieben. Die *Ergebnisse* und *Diskussion*, die auf drei begutachteten Publikationen basieren, werden in den jeweiligen drei Kapiteln vorgestellt (**Kapitel 5, 6 und 7**).

In **Kapitel 5** (basierend auf **Publikation 1**) wird die Herstellung von hochaktiven, säulenförmigen  $\text{TiO}_2$ -Nanostrukturen unter Verwendung von Puls-DC-Magnetron-Sputtern präsentiert. Eine systematische Untersuchung (thermisch induzierte Vernetzungen von Rissen und Kontrolle der Schichtdicke) wurde getätigt, um die photokatalytische Leistung von abgeschiedenen  $\text{TiO}_2$  Schichten zu optimieren. Zusätzlich zu der Herstellung von  $\text{TiO}_2$ -Dünnschichten wurde besonderes Augenmerk darauf gelegt, einen geeigneten analytischen Ansatz zu entwickeln, um photokatalytische Reaktionen, die direkt an der  $\text{TiO}_2$  Schichtoberfläche stattfinden, anzuzeigen (anstatt der unmittelbaren Analyse der Photokatalyse durch Beobachten des Entfärbens einer wässrigen Farbstofflösung, die als ein Kontrollschadstoff verwendet wird). Eine ultraschnelle, verlässliche Analysemethode wurde eingeführt und mit der Standardanalysemethode (DIN 52980:2008-10) verglichen. Mithilfe des vorgeschlagenen Ansatzes wurden zum ersten Mal sowohl das umkehrbare (Umwandlung zu farblosem Leuco-Methylenblau) als auch das irreversible Entfärben von Methylenblau durch  $\text{TiO}_2$  bestimmt, ohne einen Stabilisator oder Elektronendonator (SED) zu verwenden.

**Kapitel 6** (basierend auf **Publikation 2**) umfasst die Entwicklung einer Hybrid Al/ $\text{TiO}_2$ -Dünnschicht, die eine herausragende photokatalytische Leistung aufweist. Durch Einleiten einer kontrollierten Menge von Sauerstoff in die Gas Aggregation Source (GAS) wurden plasmonische Aluminium- (Al) Nanopartikel von kontrollierter Größe und Kristallinität erzielt. Während eine partielle Oxidation des Aluminiumtargets stabile

sauerstoffhaltige Kerne beim Sputtern produziert, die eine Nukleierung der Al-Nanopartikel auslöste, schützte eine ultradünne Sauerstoffschicht, die Al-Nanopartikel ummantelnd, sie vor weiterer übermäßigen Oxidation. TiO<sub>2</sub>-Schichten, die von Al-Nanopartikeln mit vorwiegender Größe von 20-25nm bedeckt waren, führten zu deutlich höherer photokatalytischer Aktivität (95-100%) gegenüber reinem TiO<sub>2</sub> (35-40%).

**Kapitel 7** (basierend auf **Publikation 3**) konzentriert sich auf den Gebrauch von hochaktiven TiO<sub>2</sub>-Dünnschichten für die photokatalytische Abscheidung von spitzen Gold-(Au-)Nadeln mit hohem Aspektverhältnis, die für diverse Anwendungen, einschließlich Energiegewinnung, Medizin, sowie Wechselwirkungen von Zelloberflächen und SERS von biomolekularen Sensoranwendungen interessant sein könnten. Das Deponieren von Au auf die TiO<sub>2</sub>-Schicht wurde durch die Reduktion der Au<sup>+3</sup>-Ionen direkt auf die TiO<sub>2</sub>-Schichtoberfläche mithilfe eines neuartigen photokatalytischen Reduktionprozesses (frei von Tensiden) erreicht. Ergänzend zum üblichen photochemischen Ladevorgang von Au auf TiO<sub>2</sub> wurde hier außerdem die Strukturierung von Au-Strukturen auf TiO<sub>2</sub>-Schichten durch die selektive Aktivierung der TiO<sub>2</sub>-Oberfläche sowie mittels direkter Reduktion der Au-Strukturen auf diese aktiven Flächen ohne zusätzliche Lithografieprozesse durchgeführt.

Abschließend wird in einem zusammenfassenden Fazit ein allgemeines *Resümee* (**Kapitel 8**) gezogen und eine *Prognose* (**Kapitel 9**) für zukünftige Forschungsaktivitäten gestellt.

# Declaration of Authenticity

I, the undersigned, Muhammad Zubair Ghori, hereby declare that this dissertation is my original work and all passages and ideas that are not mine have been fully and properly acknowledged to fulfil the purposes and objectives of this study and have not been previously submitted (in whole or part) to any other university for any academic degree. Additionally, the work was carried out under the advice of Prof. Dr. Franz Faupel and Prof. Dr. Cenk Aktas. No other persons were involved in the preparation of this work.

The work was conducted under obedience of the rules for good scientific practice of the German Science Foundation (DFG). Additionally, this dissertation has already been published and under consideration in parts in the following journals:

1. Solar Energy Materials and Solar Cells, **Entitled:** “*A comparative study of photocatalysis on highly active columnar TiO<sub>2</sub> nanostructures in-air and in-solution*”.
2. ACS Applied Nano Materials **Entitled:** “*The Role of UV Plasmonics on Photocatalytic Performance of TiO<sub>2</sub> Decorated with Al Nanoparticles*”.
3. Advanced Materials Interfaces **Entitled:** “*Photocatalytic Growth of Hierarchical Au Needle-Clusters on Highly Active TiO<sub>2</sub> Thin Film*”.

Signature

Place and date: Kiel, den 23 May 2018

# Declaration of Authorship/Co-authorship

I, Muhammad Zubair Ghori, state here the nature of my involvement to the work in the following publications which form this dissertation.

## Publication 1

*Entitled: “A comparative study of photocatalysis on highly active columnar TiO<sub>2</sub> nanostructures in-air and in-solution”, **M. Z. Ghori**, S. Veziroglu, B. Henkel, A. Vahl, O. Polonskyi, T. Strunskus, F. Faupel, O. C. Aktas, reused in chapter 5 with the permission of Solar Energy Materials and Solar Cells. Copyright (2018), Elsevier*

I prepared all the samples, performed the preparation of samples and characterization using UV-vis, XPS, SEM, Raman, all data analysis, figures and graphs, and wrote the text as a first author.

## Publication 2

*Entitled: “The Role of UV Plasmonics on Photocatalytic Performance of TiO<sub>2</sub> Decorated with Al Nanoparticles”, **M. Z. Ghori**, S. Veziroglu, A. Hinz, B. B. Shurtleff, O. Polonskyi, T. Strunskus, J. Adam, F. Faupel, O. C. Aktas, ACS Applied Nano Materials (submitted), used in chapter 6.*

I prepared all the samples, performed the preparation of samples and characterization using SEM, XPS, UV-vis, TEM sample preparation, figures and graphs, and wrote the text as a first author.

## Publication 3

*Entitled: “Photocatalytic Growth of Hierarchical Au Needle-Clusters on Highly Active TiO<sub>2</sub> Thin Film”, S. Veziroglu, **M. Z. Ghori**, J. Fiutowski, M. Kamp, L. Kienle, H. G. Rubahn, T. Strunskus, J. Adam, F. Faupel, O. C. Aktas, reused in chapter 7 with the permission of Advanced Materials Interfaces. Copyright (2018), Wiley.*

I prepared most of the samples and characterized them using SEM, TEM all analysis (including photocatalytic testing and Raman spectroscopy), figures and graphs, and wrote the text as a first co-author.

In addition, following publications were authored/co-authored during this PhD work:

#### **Publication 4**

*Entitled:* “Ultra-fast degradation of methylene blue by Au/ZnO-CeO<sub>2</sub> nano-hybrid catalyst,” S. Veziroglu, M. Kuru, **M. Z. Ghor**, F. K. Dokand, A. M. Hinz, T. Strunskus, F. Faupel, O. C. Aktas, Materials Letters (2017).

#### **Publication 5**

*Entitled:* “Tuning silver ion release properties in reactively sputtered Ag/TiO<sub>x</sub> nanocomposites”, J. Xiong, **M. Z. Ghor**, B. Henkel, T. Strunskus, U. Schürmann, M. Deng, L. Kienle, F. Faupel, Applied Physics A (2017).

#### **Publication 6**

*Entitled:* “Controlling surface segregation of reactively sputtered Ag/TiO<sub>x</sub> nanocomposites,” J. Xiong, **M. Z. Ghor**, B. Henkel, T. Strunskus, U. Schürmann, Kienle, F. Faupel, Applied Physics A (2014).

#### **Publication 7**

*Entitled:* “Synthesis of 3D Nanoporous Surfaces with Controlled Wetting properties for functional applications”, S. Schröder, **M. Z. Ghor**, S. Veziroglu, T. Strunskus, F. Faupel, O. C. Aktas, in submission.

# Symbols and Abbreviations

## List of symbols

Symbols	Symbol name	Symbols	Symbol name
$\mu$	Chemical potential	$h^+$	hole
$A$	Area	$I$	Current
$Ag$	Silver	$k$	Boltzmann's constant
$Al$	Aluminum	$k$	Rate constant
$Ar$	Argon	$l$	Path length
$Au$	Gold	$m_e$	Effective mass of electron
$c$	Concentration	$Mg$	Magnesium
$Cu$	Copper	$m_h$	Effective mass of hole
$d$	Diameter	$n$	Magnetron efficiency
$E$	Electric field	$N_A$	Avogadro's number
$e^-$	Electron	$O_2$	Oxygen
$E_{av}$	Average UV light intensity	$Pa$	Pascal
$E_b$	Binding energy	$R$	Specific absorbance
$E_c$	Conduction band energy	$Ti$	Titanium
$E_c$	Min. conduction band energy	$TiO_2$	Titanium dioxide
$E_F$	Fermi energy	$V$	Voltage
$E_g$	Bandgap energy	$V$	Volume
$E_k$	Kinetic energy	$\Delta A_\lambda$	Change in absorbance maximum
$E_p$	Photon irradiance	$\Delta t$	Change in time
$E_v$	Max. valence band energy	$\Delta T$	Change in transmission
$E_v$	Valance band energy	$\lambda$	Wavelength
$E_{vacuum}$	Vacuum level	$\xi$	Photon efficiency
$F$	Lorentz force	$\mathcal{E}$	Molar extinction coefficient
$f(E)$	Fermi-Dirac distribution function		
$h$	Plank's constant		
$\hbar$	Reduced Plank's constant		

## List of Abbreviation

Abbreviation	Full form	Abbreviation	Full form
Abs	Absorbance	OAD	Oblique angle deposition
AR	Aspect ratio	PC	Photocatalyst
B/W	Black and white	PE	Primary electron
BSE	Back-scattered electron	PVD	Physical vapor deposition
CAGR	Compound annual growth rate	QCM	Quartz crystal microbalance
CB	Conduction band	QD	Quantum dot
DC	Direct current	RF	Radio frequency
DI	De-ionized	SAED	Selected area electron diffraction
DOS	Density of states	SCCM	Standard cubic centimeter per minute
EBL	Electron beam lithography	SE	Secondary electron
FEM	Finite-element method	SED	Sacrificial electron donor
FIB	Focused ion beam	SEM	Scanning electron microscope
GAS	Gas aggregation source	SERS	Surface enhanced Raman spectroscopy
HAuNCs	Hierarchical anisotropic gold nanoclusters	SHE	Standard hydrogen electrode
HIM	Helium ion microscope	SPR	Surface plasmon resonance
HRTEM	High resolution TEM	SZM	Structure zone model
IUPAC	International Union of Pure and Applied Chemistry	TEM	Transmission electron microscope
LED	Light emitting diode	TMP	Turbo-molecular pump
LEFE	Local electrical field enhancement	UV	Ultraviolet
LMB	Leuco-methylene blue	VB	Valance band
LSPR	Localized Surface Plasmon Resonance	Vis	Visible
MB	Methylene blue	XPS	X-ray photoelectron spectroscopy
MOS	Metal oxide semiconductor		
NPs	Nanoparticles		
NSL	Nanosphere lithography		

# Table of Contents

<b>Chapter 1. Introduction .....</b>	<b>1</b>
<b>1.1. TiO<sub>2</sub>: as a Strong Photocatalyst for Environmental Remediation and Energy Source.....</b>	<b>2</b>
<b>1.2. Enhancement of TiO<sub>2</sub> Photocatalysis by Plasmonic NPs .....</b>	<b>4</b>
<b>1.3. TiO<sub>2</sub> Photocatalysis - as an Effective Tool in Chemical Synthesis .....</b>	<b>5</b>
<b>Chapter 2. Theory .....</b>	<b>6</b>
<b>2.1. Photocatalysis and Semiconductors .....</b>	<b>6</b>
<b>2.2. TiO<sub>2</sub> Photocatalysis.....</b>	<b>10</b>
<b>2.2.1. TiO<sub>2</sub> and Photoinduced Reactions.....</b>	<b>10</b>
2.2.2. Degradation Mechanism of Organics by TiO <sub>2</sub> Photocatalysis .....	12
2.2.3. Importance of Surface/Interface Engineering in TiO <sub>2</sub> Photocatalysis .....	15
<b>2.3. Enhancing Photocatalysis by Metallic NPs .....</b>	<b>17</b>
2.3.1. Plasmonic Contribution of Metallic NPs.....	17
2.3.2. Non-plasmonic Contribution of Metal NPs.....	20
<b>Chapter 3. Methods .....</b>	<b>22</b>
<b>3.1. Preparation of Thin Films and Hybrid Structures.....</b>	<b>22</b>
3.1.1. Sputtering of Thin Films .....	22
3.1.1.1. Sputtering of Metal and Metal-Oxides .....	25
3.1.1.2. Film Growth during Sputtering Process .....	27
3.1.2. Metal and Metal Oxide Clusters by Gas Aggregation Source (GAS).....	29
3.1.3. Metallic Clusters by Photocatalytic Reduction .....	32
<b>3.2. Characterization of Material and Photocatalytic Properties .....</b>	<b>35</b>
3.2.1. Material Characterization .....	35
3.2.1.1. SEM .....	35
3.2.1.2. XPS .....	35
3.2.1.3. TEM.....	37
3.2.1.4. Raman Spectroscopy .....	37
3.2.1.5. HIM.....	38
3.2.2. Photocatalytic Analysis .....	39
3.2.2.1. Photocatalysis in Aqueous Solution (Wet Conditions) .....	39
3.2.2.2. Photocatalysis In Air (Dry Conditions) .....	40



<b>Chapter 4. Experimental</b> .....	<b>42</b>
<b>4.1. Preparation of TiO<sub>2</sub> Films</b> .....	<b>42</b>
<b>4.2. Preparation of Al NPs by GAS</b> .....	<b>44</b>
<b>4.3. Photocatalytic Deposition of Au Micro- and Nano Structures</b> .....	<b>45</b>
<b>4.4. Characterization</b> .....	<b>46</b>
4.4.1. Material and Surface Properties .....	46
4.4.1.1. SEM .....	46
4.4.1.2. XPS .....	46
4.4.1.3. TEM.....	46
4.4.1.4. Raman spectroscopy .....	46
4.4.1.5. HIM.....	47
4.4.2. Photocatalytic Properties .....	47
4.4.2.1. Photocatalysis in Aqueous Solution (Wet Conditions) .....	47
4.4.2.2. Photocatalysis in Air (Dry Conditions) .....	49
4.4.2.3. Electrochemical Simulation.....	50
<b>Chapter 5. A comparative study of photocatalysis on highly active columnar TiO<sub>2</sub> nanostructures in-air and in-solution</b> .....	<b>51</b>
<b>5.1. Abstract</b> .....	<b>52</b>
<b>5.2. Results and Discussion</b> .....	<b>52</b>
5.2.1. TiO <sub>2</sub> Thin Film .....	52
5.2.2. Photocatalytic Degradation of MB in-Air (Dry condition) .....	54
5.2.3. Photocatalytic Degradation of MB in-Aqueous Solution (Wet Condition) .	61
5.2.4. Comparison of MB Degradation Analysis in-Air and -Aqueous Solution (Dry vs Wet Conditions) .....	63
<b>5.3. Conclusion</b> .....	<b>64</b>
<b>Chapter 6. The Role of UV Plasmonics on Photocatalytic Performance of TiO<sub>2</sub> Decorated with Al Nanoparticles</b> .....	<b>65</b>
<b>6.1. Abstract</b> .....	<b>66</b>
<b>6.2. Results and Discussion</b> .....	<b>66</b>
6.2.1. Controlling Deposition, Size, Morphology and Distribution of Al NCs.....	66
6.2.2. Structural and Optical Properties of Al Clusters .....	70
6.2.3. Photocatalytic Performance of Al/TiO <sub>2</sub> Hybrid Layers .....	73
<b>6.3. Conclusion</b> .....	<b>76</b>

<b>Chapter 7. Photocatalytic Growth of Hierarchical Au Needle-Clusters on Highly Active TiO<sub>2</sub> Thin Film.....</b>	<b>77</b>
<b>7.1. Abstract .....</b>	<b>78</b>
<b>7.2. Results and Discussion .....</b>	<b>78</b>
7.2.1. Photocatalytic Deposition of HAuNCs .....	78
7.2.2. The Influence of UV Light Intensity and Irradiation Time on the Growth of HAuNCs .....	82
7.2.3. Controlling the Growth of HAuNCs by the Photocatalytic Activity of TiO <sub>2</sub> ..	86
7.2.4. Patterning TiO <sub>2</sub> Target by Selective Phototacalytic Deposition of HAuNCs .....	88
<b>7.3. Conclusion .....</b>	<b>89</b>
<b>Chapter 8. Summary .....</b>	<b>90</b>
<b>Chapter 9. Outlook .....</b>	<b>92</b>
<b>Bibliography .....</b>	<b>93</b>

# Chapter 1. Introduction

The importance of heterogeneous photocatalysis as an alternative for environmental clean-up has been rising in variety of photocatalytic applications. These applications are potentially emerging in different research areas, including energy, environment and life sciences. The work on heterogeneous photocatalysis was firstly introduced by Goodeve and Kitchener in 1938, in which they reported on the oxidation of an organic substance [1]. Since 1972, heterogeneous photocatalysis has been frequently studied after the work of Fujishima and Honda on water splitting by a  $\text{TiO}_2$  electrode under UV irradiation [2].

In recent years, the use of semiconductors as photocatalysts has been focused towards the removal of ambient concentrations of organic and inorganic species from aqueous or gas phase systems, especially in environmental clean-up, drinking water treatment, industrial and health applications [3]. Photocatalysis is expected to play an important role in retaining sustainable development of human society by solving energy problems, improving the global environment and living conditions, and more. In 2015, Gagliardi et al. predicted the expected global market share value of photocatalysis to exceed from \$1.6 billion (2015) to \$2.9 billion by 2020 at a compound annual growth rate (CAGR) of 12.6% [4].

The main advantage of heterogeneous photocatalysis is its potential to incorporate solar radiation in the form of photons that can be converted into chemical energy by using semiconductors. It is well-known that the solar radiation given off by the sun in particular consists of infrared, visible and ultraviolet (UV) light [5], and the semiconductors like  $\text{TiO}_2$  are getting activated under UV light because of their wide bandgap (as energy of UV is higher than visible radiation) [6]. Most of the studies given in the literature report photocatalysis occurring at UV wavelength from 320 to 380 nm [7]. To incorporate visible light regime, nanoscale  $\text{TiO}_2$  particles are combined with the plasmonic nanoparticles (NPs) for more efficient photocatalysis [8].

Besides energy and environmental applications,  $\text{TiO}_2$  has also been used as photocatalytic initiator in various chemical reactions like in organic transformation, polymer post modification and conventional and living polymerization [9]. In such processes high energy photons are used to generate oxidative holes and free radicals that can initiate polymerization of monomers without using any toxic reducing agent [10]. Additionally,  $\text{TiO}_2$  is used as an effective electron donor in the synthesis of metallic NPs by

photoreduction process. This can result in synthesizing metallic NPs within a single step and without using any surfactant or reducing agent [11–13].

In the following subsections the discussion firstly focuses on the developments in the TiO<sub>2</sub> photocatalysis research and its importance for the industrial applications. Afterwards, the limitation in using TiO<sub>2</sub> for photocatalytic applications is discussed and a strategy to overcome this limitation by plasmonic Al NPs is described. At the end of this chapter a novel method (based on TiO<sub>2</sub> photocatalysis) to deposit Au is introduced.

## 1.1. TiO<sub>2</sub>: as a Strong Photocatalyst for Environmental Remediation and Energy Source

Over the last years, the research interest in photocatalysis has expanded drastically (*Figure 1*). While there was just small number of scientific publications about photocatalysis in the year 2000 (97, 68 with TiO<sub>2</sub> publications), the number in 2008 was already 439 (319 with TiO<sub>2</sub>). Since then, the amount of scientific publications has enormously grown, so in 2016 1440 results (629 with TiO<sub>2</sub>) and in 2017 even 2074 (815 with TiO<sub>2</sub>) could be found [14].

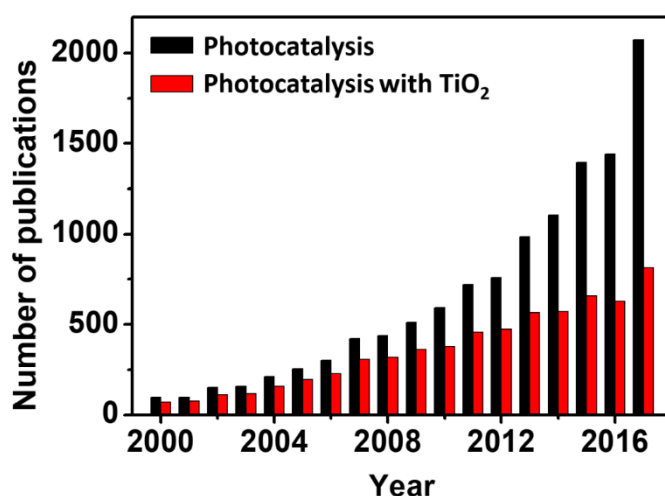


*Figure 1* Overview of the number of scientific publications on photocatalysis and photocatalysis with TiO<sub>2</sub> over the years (values are taken from Science Direct online database) [14].

TiO<sub>2</sub> has several beneficial properties towards humans and nature (as mentioned earlier) which makes it an almost ideal semiconductor and interesting for industries, as it also has low costs [15,16]. Regarding different interests, TiO<sub>2</sub> can be used for example in antiseptic and antibacterial disinfectant solutions, UV-protective cosmetics, as pigments in paint formulations, self-cleaning surfaces or in other building materials (*Figure 2*) [17–20]. As an example, in Dortmund and Detmold (Germany), a special cement (TioCem<sup>®</sup>) with

photocatalytic TiO<sub>2</sub> has been used as road material for some bus stations to reduce the air pollution in frequently used traffic areas [21].

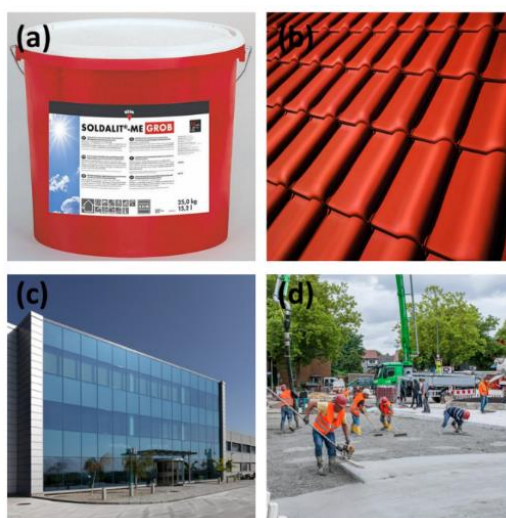


**Figure 2** The use of TiO<sub>2</sub> as self-cleaning surfaces (a) paints (b) roof tiles (c) glass windows and (d) TioCem<sup>®</sup> (cement) [21] used at the bus station in Dortmund, Germany.

The market distribution of photocatalytic products for the energy and environment industry in 2017 [22] is displayed in **Figure 3** which demonstrates that around half of the market share is covered by products for exterior material (48%), whereas interior material has 12%. Purifier own nearly 30% share and further products can be found in road materials (3%), for consumers (4%), and others (5%).

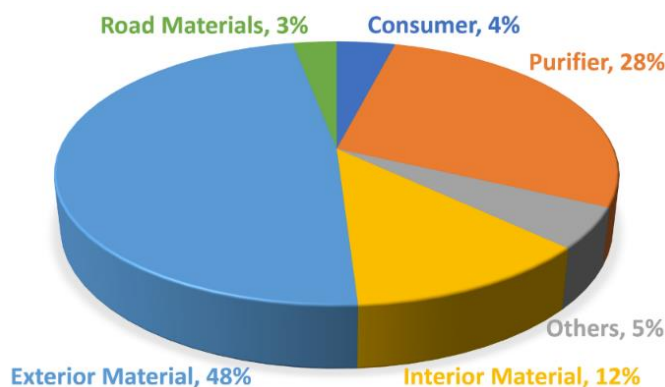


**Figure 3** Photocatalytic products and their market distribution, modified from [22].

In addition to various advantages of TiO<sub>2</sub> there are also some limitations in its use. For instance, the recombination of charge carriers within TiO<sub>2</sub> and the limited solar energy utilization (only active in UV range) are the main drawbacks. Various technical strategies have been suggested to improve photocatalytic performance of TiO<sub>2</sub>. Incorporation of metallic nanoparticles in TiO<sub>2</sub> is one of the effective approaches. In the following sub-chapter, such approaches are briefly summarized.

## 1.2. Enhancement of TiO<sub>2</sub> Photocatalysis by Plasmonic NPs

Solar energy spectrum consists of almost 52% infrared, 43% visible and 5% UV radiations (**Figure 4**), and TiO<sub>2</sub> is only active under these limited amount of UV radiations. To increase the solar activity of TiO<sub>2</sub> under broad range of solar spectrum, the most efficient way is to combine it with plasmonic metal NPs. Noble metal NPs (Au, Ag etc.) are extensively used and studied to improve photocatalytic performance under visible solar radiations [23,24]. The **localized surface plasmon resonance** (LSPR, further details in **section 2.3.1**) of noble metal NPs can be tuned and shifted from near UV to visible spectrum. In addition to noble metal NPs, Al also exhibits the property of LSPR from far UV to near-infrared spectrum. The low cost, earth abundance and broad range of plasmonics make Al NPs very special for plasmon enhanced photocatalysis due to their high plasma energy of 15.6 eV and high electron density [25,26]. Additionally, low optical loss and wide tunable range of plasmonic nature make Al an ideal material for next generation optical antennas, plasmon enhanced detectors and display technologies [27–29]. The recent developments in synthesis of Al NPs and its applications as plasmonic tools will be explained in detail in the theory **section 2.3**.

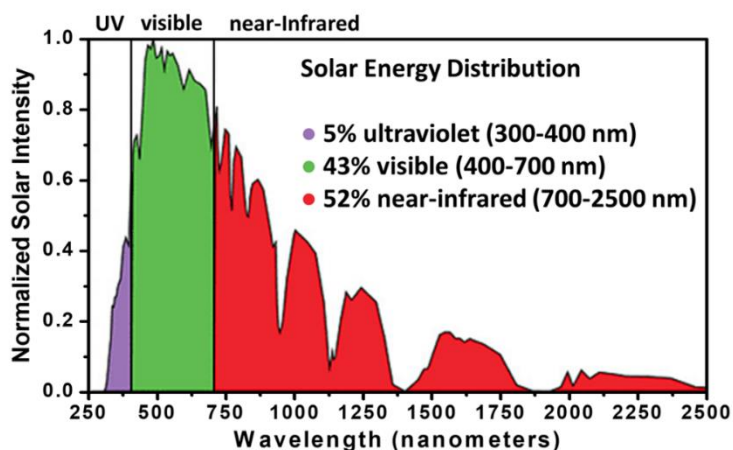


**Figure 4** Solar energy distribution from UV to Infrared region, taken from [30].

Beside the use of TiO<sub>2</sub> photocatalysis in environmental remediation, it also offers a great potential for photochemistry. The photocatalytic nature of TiO<sub>2</sub> can be used as an initiator (e.g. polymerization) or reducing agent (e.g. reduction of metal ions) in different chemical reactions. In the following sub-chapter, the use of TiO<sub>2</sub> photocatalysis in chemical synthesis as a valuable alternative to photochemistry is described.

### 1.3. TiO<sub>2</sub> Photocatalysis - as an Effective Tool in Chemical Synthesis

Photochemical processes are used to perform complex organic reactions and have various applications in the field of photochemistry. These processes are carried out under highly intense UV or visible light to initiate the reaction. Such as curing, initiator-based polymerization, reaction acceleration and termination processes. Use of the light activated toxic organic compounds for the mentioned processes are limited for several applications. Therefore, photocatalytic reduction process using TiO<sub>2</sub> is advantageous over the photochemical processes because of its superior properties such as biocompatibility and non-toxicity. The UV activated TiO<sub>2</sub> acts as an electron donor to initialize the chemical reactions. In other words, UV activated TiO<sub>2</sub> can reduce organic and inorganic compounds easily.

TiO<sub>2</sub> photocatalysis can also be used to reduce several heavy metal ions directly on its surface. Usually, photoreduction of metal ions (such as Au, Ag and Cu) in aqueous solutions has received attention for many years in photochemistry because of their unique optical (plasmonic) properties. Recently, TiO<sub>2</sub> is being considered for catalyzing various reduction reactions, which can provide a Green Chemistry as an alternative to the conventional methods that use thermal energy or reducing agents. In such a process, metal and organic ions present in an aqueous solution can be directly reduced at the surface of TiO<sub>2</sub>.

# Chapter 2. Theory

In this chapter the general definitions of photocatalysis and semiconductors and their properties are presented. The focus will be on the semiconductor bandgap, its different classifications and its energy dependency according to the size of a semiconductor. Hereafter, the TiO<sub>2</sub> photocatalysis is discussed with special attention paid to the photoinduced reactions and their application in the degradation of a standard test dye, e.g. Methylene Blue (MB). Furthermore, methods used to enhance the photocatalytic activity of TiO<sub>2</sub> are described in detail.

## 2.1. Photocatalysis and Semiconductors

The word photocatalysis originates from Greek language, where *photo* (Greek *phōs*) means light and *catalysis* (Greek *katalusis* from *kataluein*) means decompose [31]. In photocatalysis, light is used to excite a photocatalyst which accelerates the rate of a chemical reaction without involving or consuming the photocatalyst in the reaction. In general, photocatalysis occurs in the presence of light and a semiconductor.

Photocatalysis can be classified into two categories: (i) **homogenous photocatalysis** and (ii) **heterogenous photocatalysis**. In the former, the reactants and the photocatalyst exist in the same phase, whereas in the latter, reactants and the photocatalyst exist in different phases. In this work the discussion will be limited to the heterogenous photocatalysis.

To understand the mechanism of photocatalysis, first, one should be familiar with the basics of semiconductors. A semiconductor is a material that cannot conduct completely, rather its conduction ability lies in between insulators and conductors. In a pure semiconductor a bandgap exists between the **valence (VB)** and **conduction bands (CB)**. Generally, the bandgap energy ( $E_g$ ) between the highest filled VB level and the lowest unfilled CB level is of the order of one electron volt. The chemical potential  $\mu$  (known as **Fermi level**,  $E_F$ ) exists within the bandgap of a semiconductor. At zero Kelvin, available states are sequentially occupied starting from the lowest energy level; the uppermost filled level is known as the **Fermi energy** and above the Fermi energy no energy levels are occupied by electrons at 0 K. At temperatures above 0 K, the probability of finding an electron at a certain energy level can be calculated by the **Fermi-Dirac distribution function** given in formula (1). It shows that with increasing temperature, electrons have a higher probability of being found in higher energy states.



$$f(E) = \frac{1}{1 + e^{(E-\mu)/kT}} \quad (1)$$

Here,  $E$  is the energy state under consideration,  $\mu$  is the Fermi level,  $k$  is Boltzmann's constant and  $T$  is absolute temperature.

The bandgap helps to determine the optical properties of a semiconductor. If a photon of light with energy  $E > E_g$  is absorbed by the semiconductor material, an electron may be promoted from the valence band to the conduction band, simultaneously producing a hole in the valence band. This phenomenon begins to occur at a certain radiation frequency called the absorption threshold. Close to the band edge minima (in the CB) and maxima (in the VB), the energy of an electron (2) and hole (3) can be calculated as follows:

$$E_e = E_g + \frac{\hbar^2 k^2}{2m_e} \quad (2)$$

$$E_h = -\frac{\hbar^2 k^2}{2m_h} \quad (3)$$

Here,  $E_g$  is the bandgap energy,  $\hbar$  is the reduced Plank's constant,  $k$  is the wave vector,  $m_e$  is the effective mass of electron and  $m_h$  is the effective mass of hole. The effective mass depends on the inverse curvature of the band which arises from the periodic potential of the crystal. The total absorbed energy can be determined by using formula (4):

$$\Delta E = E_g + \frac{\hbar^2 k^2}{2m_e} - \left( -\frac{\hbar^2 k^2}{2m_h} \right) = \left( E_g + \frac{\hbar^2 k^2}{2m_e} \right) + \frac{\hbar^2 k^2}{2m_h} \quad (4)$$

Here,  $\Delta E$  is the total energy difference, i.e. after photon absorption, the energy of the electron and the energy of the hole. Recombination is influenced by the electronic states (minimum and maximum energy states in the CB and VB, respectively) of the semiconductor. These states are mostly characterized by crystal momentum, often described as a vector  $\mathbf{k}$  existing within the **Brillouin zone** of the crystal lattice and determine the properties of the semiconductor bandgap. A schematic illustration of electron-hole recombination processes is displayed in **Figure 5**. It can be observed that the total energy remains conserved in each recombination process. In direct transition (where electron momentum does not change), recombination energy is released in the form of photon emission only (**Figure 5a**). Materials which show direct transition are known as **direct**

**semiconductors.** In contrast, energy is released in the form of a photon and a phonon in indirect transition due to the difference in electron momentum. Such indirect transition materials are called **indirect semiconductors** (*Figure 5b*). The lifetime of the exciton is increased in indirect transitions and an excited electron is available for longer time periods for chemical reactions.

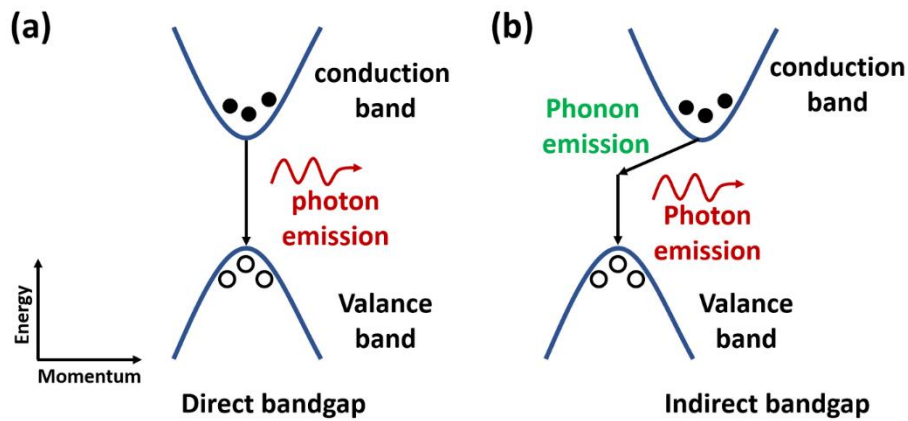


*Figure 5* Schematic illustration of electron-hole recombination in (a) direct and (b) indirect bandgap semiconductors, modified from [32].

The bandgap energy also depends on the physical dimensions of the semiconductor [33]. Bulk semiconductors have low bandgap energies compared to nanoscale semiconductors, as illustrated in *Figure 6*. As a result of quantum confinement, which is a limitation in sample dimension on the order of a particle's matter wavelength, the energy levels become discretized. In the case of a single atom or molecule (also known as **quantum dot (QD)**) discrete energy levels exist (represented by single lines in *Figure 6c*). Therefore, at the nanoscale (compared to bulk) the absorption spectrum of semiconductors shifts to lower wavelengths (blue shift).

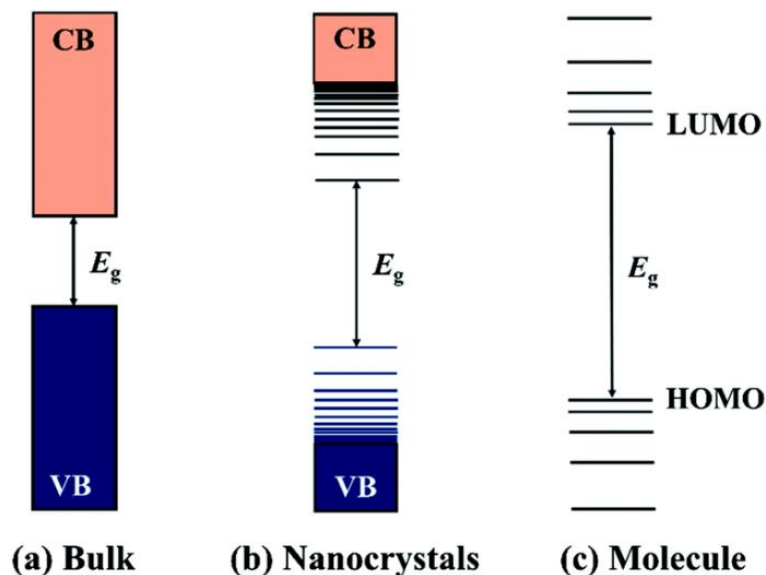


**Figure 6** Schematic illustration of electronic energy states of semiconductors at different size scales, taken from [33].

A schematic overview of the energy level structure of semiconductor nanostructures with various decreasing dimensions is given in **Figure 7**. Density of states (DOS) is defined as the number of states per energy interval per unit volume. DOS depends on the dimensional size of the sample (two, one and zero spatial dimensions of the semiconductor). In the case of a nanoparticle or quantum dot, if the charge carrier is limited in one dimension, a quantum well is formed. If the charge carrier experiences 2-dimensional confinement, it is referred to as a Quantum Wire or Quantum Rod, depending on its relative aspect ratio.

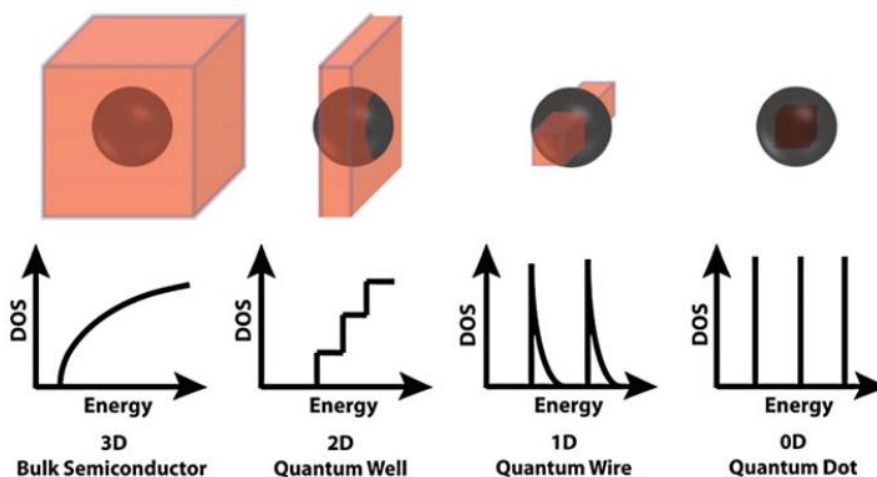


**Figure 7** Schematic illustration of the energy level structure of semiconductor nanostructures with reduced dimensionality (3D, 2D, 1D and 0D). The exciton diameter is represented by the sphere. This figure is taken from [34].

## 2.2. TiO<sub>2</sub> Photocatalysis

### 2.2.1. TiO<sub>2</sub> and Photoinduced Reactions

Titanium dioxide is a naturally occurring oxide and abundant in earth. Its empirical formula is TiO<sub>2</sub>. Like other metal oxides, it is a hard material, thermally stable and chemically resistant. It can be found in three different polymorphs: **anatase**, **rutile** and **brookite** (schematic of structures is given in *Figure 8*). All three phases show tetragonal symmetry where each Ti atom is octahedrally coordinated with six oxygen atoms. Anatase is composed of predominantly point-sharing octahedra. In contrast to this, due to the edge-sharing of octahedra in rutile, it forms long chains which makes it the most thermodynamically stable of the three polymorphs, and brookite is a combination of edge- and point-sharing. Both, anatase and rutile are the most studied phases for photocatalytic applications. Whereas, brookite is often difficult to synthesize and in general photocatalytically inactive, therefore, the properties of brookite are excluded from discussion.

Thermodynamically rutile is the most stable polymorph compared to other metastable phases of TiO<sub>2</sub>. It is a direct-bandgap semiconductor with a bandgap energy of 3.0 eV. While this bandgap is smaller than that of other TiO<sub>2</sub> polymorphs, rutile is generally not a suitable candidate for photocatalysis because of its high rate of electron-hole recombination. Anatase TiO<sub>2</sub> is metastable above 600°C but still less stable than rutile. The structured-based analysis showed that anatase is the stable phase at nanoscale due to its relatively low surface energy, that is more efficient for photocatalysis.

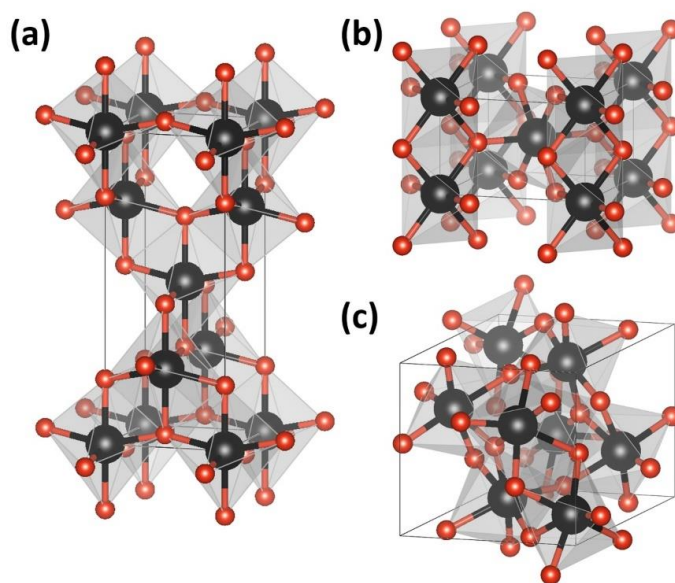


*Figure 8* Unit cells of different polymorphs of TiO<sub>2</sub>, (a) Anatase, (b) Rutile and (c) Brookite.

Anatase is an indirect bandgap semiconductor (see *section 2.2*). The bandgap of anatase is 3.2 eV, that limits its activity threshold to UV light. Excited electrons on anatase ( $E = -0.66$  eV vs. standard hydrogen electrode) are sufficiently energetic for the reduction of  $H^+$  to hydrogen, while holes ( $E = 2.54$  eV vs. standard hydrogen electrode) can oxidize water to oxygen, which helps in the degradation of many organic pollutants.

The absorption of photons by  $TiO_2$  (if photon energy exceeds the  $E_g$ ) initiates photocatalytic reactions at its surface. The primary reactions responsible for the photocatalytic effect are interfacial redox reactions by electrons and holes, labeled in *Figure 9*: (1) photon absorption by  $TiO_2$  and charge carriers are generated; (2) recombination reaction of charge carrier; (3) electron trapping in the conduction-band at Ti(III) state; (4) trapping of a valence-band hole at a surficial titanol group; (5) oxidation reaction by a valence-band hole; (6) reduction reaction by a conduction-band electron; and (7) further mineralization products.

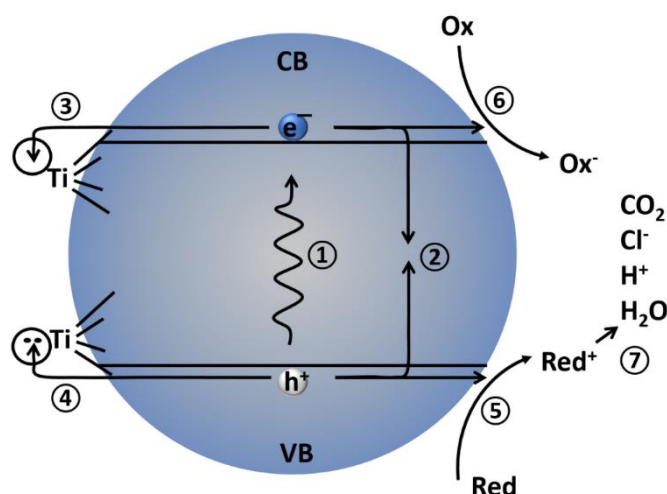


*Figure 9* Mechanism of  $TiO_2$  photocatalytic reactions by UV light exposure, modified from [35].

The dynamics (with corresponding time intervals) of different reactions of the photogenerated charge carriers in  $TiO_2$  are shown in *Figure 10*. These time intervals are usually obtained by means of time-resolved absorption spectroscopy, that is normally used for the photogenerated charge carrier formation, relaxation, recombination and transfer processes.

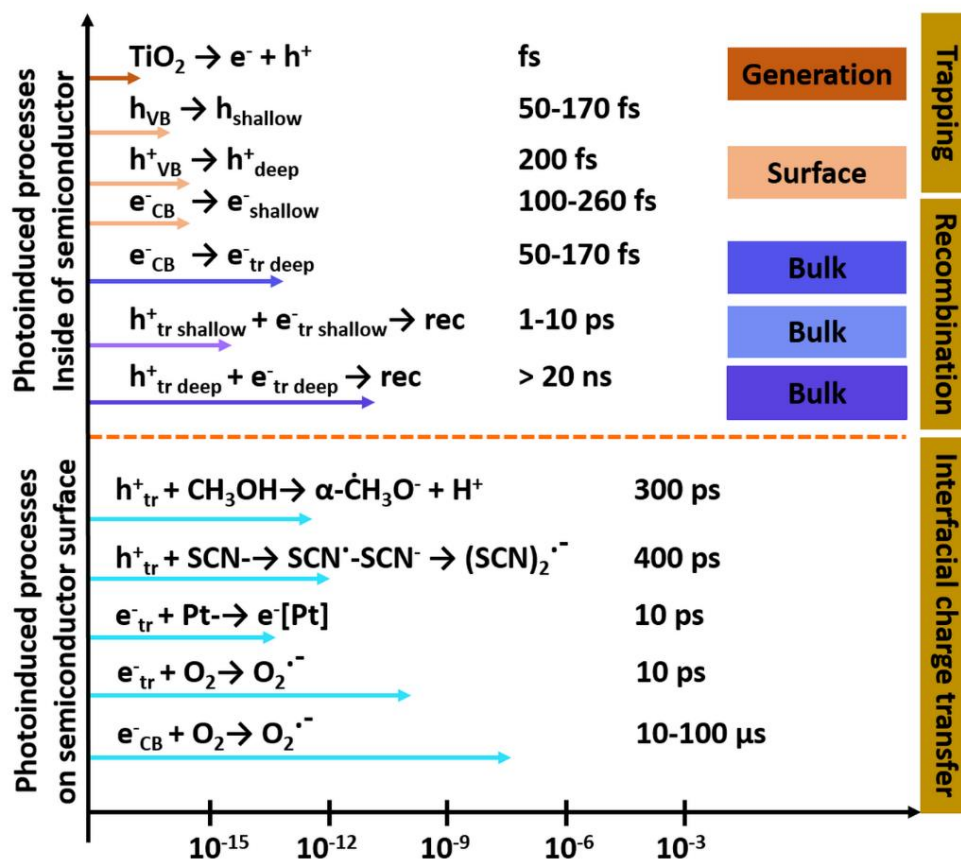
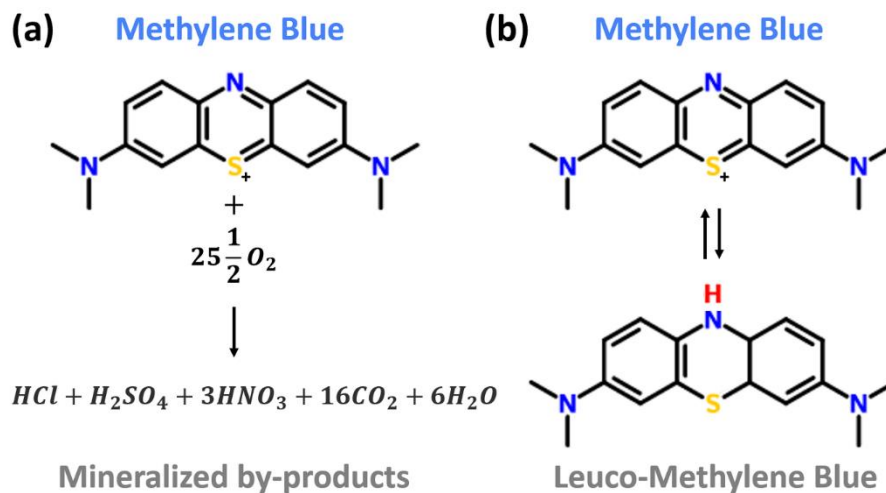


Figure 10 Photocatalytic reactions by TiO<sub>2</sub> and the corresponding time scales, based on [35].

### 2.2.2. Degradation Mechanism of Organics by TiO<sub>2</sub> Photocatalysis

Mostly, the photocatalytic activity of TiO<sub>2</sub> (in the form of particles or thin film) is analyzed by immersing it into a colorful test pollutant (typically an organic dye solution) and observing the decolorization of the solution upon exposing it to UV light. The mechanism of TiO<sub>2</sub> charge carrier generation and availability of transition states are shown in the previous section (see *Figure 8*). In the following, the mechanism of a standard test dye degradation by TiO<sub>2</sub> is described in detail. MB as the member of thiazine dye group, is most widely used organic test pollutant among various organic dye types [36]. In most TiO<sub>2</sub> photocatalysis studies the decolorization of the aqueous MB solution is used as a gauge to measure the kinetics of mineralization of carbon, nitrogen and sulfur heteroatoms into CO<sub>2</sub>, NH<sub>4</sub><sup>+</sup>, NO<sub>3</sub><sup>-</sup> and SO<sub>4</sub><sup>2-</sup>, respectively (as shown in the photochemical reaction *Figure 11a*) [37].



**Figure 11** MB reaction schemes (1) mineralization (2) conversion to colorless form (LMB) [38,39].

On the other hand, the decolorization might result from the conversion of MB to its leuco form (LMB) (see reaction in **Figure 11b**). This reduced LMB form of MB is a colorless state and can quickly be converted back to its blue-colored MB state in the presence of oxygen (oxidation reaction occurs at room temperature) [40]. The complete route of MB degradation (mineralization process by neglecting MB-LMB conversion) is presented in **Figure 12**.

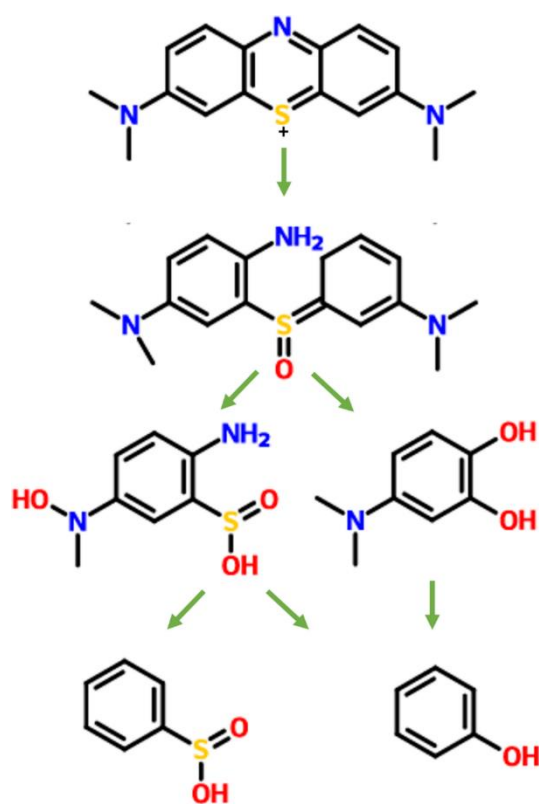


**Figure 12** Photocatalytic degradation pathway of MB, edited from [37].

The mechanism of photocatalysis and MB dye degradation is a complex process and the photocatalytic degradation of such organic molecule by  $TiO_2$  can be considered as an

indirect reaction which is basically followed by the generation of charge carriers and different radicals (e.g.  $O_2^{\bullet-}$ ,  $OH^{\bullet}$ ) formation. These photocatalytically generated charge carriers and radicals on  $TiO_2$  surface are responsible for further mineralization reactions that are given below in the form of possible reaction schemes and taken from [37].

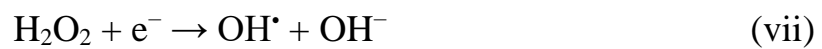
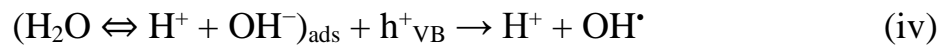
The photocatalytic reaction starts as UV light consisting of efficient photons ( $h\nu \geq E_g = 3.2 \text{ eV}$ ) is absorbed by  $TiO_2$  and generates electron-hole pair.



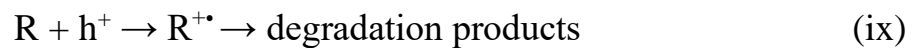
Photogenerated electrons are further transferred to oxygen and form superoxide ( $O_2^{\bullet-}$ ).  $O_2^{\bullet-}$  can selectively act as an oxidant for organic compounds.



The  $OH^-$  groups present in the solution can be neutralized by holes by producing active  $OH^{\bullet}$  radicals. These generated  $O_2^{\bullet-}$  active radicals can also be neutralized by protons by producing hydrogen peroxide that can further react with the photogenerated electrons and produce  $OH^-$  and  $OH^{\bullet}$  radicals.



Photogenerated holes can directly oxidize the organic reactants (ix) and  $OH^{\bullet}$  radicals can also attack organic reactants and produce degradation products (mineralization of organics).





### 2.2.3. Importance of Surface/Interface Engineering in TiO<sub>2</sub> Photocatalysis

As described in the previous section, a pure semiconductor like TiO<sub>2</sub> can perform photocatalysis in three steps including (i) charge generation, (ii) transfer and (iii) consumption (a complete charge kinetics process). These three steps occur within the same structure that may limit the efficiency of the system which also depends on the energy level of the valence and conduction band and its difference. In narrow band semiconductors low energy is required to carry out these steps that can perform these reactions within the visible light of solar spectrum (43% as illustrated in *Figure 4*, see *section 1.2*), but the redox ability of material is very limited (low bandgap and high recombination possibilities). Therefore, wide band semiconductors like TiO<sub>2</sub> are potentially capable to perform redox reactions but due to limitation of UV in solar spectrum (only 5%) the solar energy conversion ability is limited for such materials. In order to overcome these problems many surfaces with different architectural designs and model interfaces (formed by the combination of different materials) are proposed (see *Figure 13*) to improve the photocatalytic efficiencies of these wide band semiconductors.

The first architectural design given in *Figure 13a* consists of a single component semiconductor (homogenous structure). The photocatalytic properties of this configuration like bare TiO<sub>2</sub> can be improved by different means including crystal structure (described in *section 2.2*), particle size (increasing active surface area of NPs by decreasing size, see *Figure 35*, *section 3.2.2*) and in case of thin film by changing surface morphology (as porosity and different surface architectures play an important role in the surface activeness of the thin film).

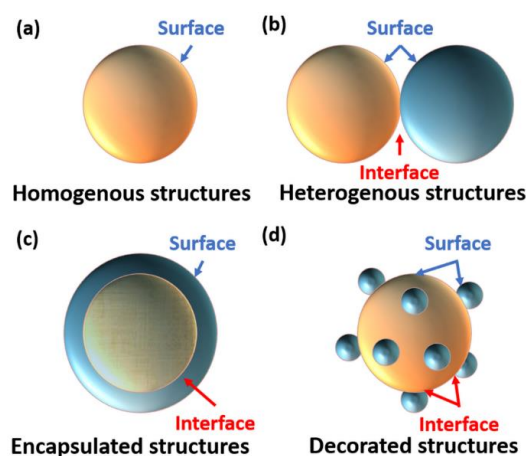


*Figure 13* Schematic illustration of interfaces and surfaces in basic photocatalytic architectural structures, modified version of [34].

Heterojunction structures (**Figure 13b**) consisting of two different semiconductors [41] (e.g. **semiconductor I**, such as TiO<sub>2</sub> with the wide bandgap and **semiconductor II**, with the narrow bandgap) form an interface that can improve the redox capability of such architectural designs by harvesting broad radiations of solar spectrum. In such scheme when broad solar light spectrum is irradiated on such interface structures, the photogenerated holes from semiconductor I with a higher valence band maximum can directly recombine with the photogenerated electrons from semiconductor II with a lower conduction band minimum through the interfacial conduction. Meanwhile, the electrons in semiconductor I with a higher conduction band minimum and the holes in semiconductor II with a lower valence band maximum will be preserved for the reduction and oxidation reactions, respectively. Such mixed-oxide structures can improve catalytic properties quite efficiently by changing the ratio of semiconductors combinations. We have illustrated, by using an appropriate ratio of semiconductors, that the photocatalytic efficiency can be enhanced [42].

Another interesting possible heterostructure is the **encapsulated structure** (**Figure 13c**). These structures resemble with the core-shell structure in which only single surface is exposed to the reaction media. Such interfaces can improve the light induced activation of the surface that is dependent on the optical and geometrical properties of core semiconductor, providing different mechanisms like multiple light scattering through the sphere and related geometrical factors as proposed by Alessandri et al. [43]. Such surfaces are mostly used for some special applications like **surface enhanced Raman scattering** (SERS).

In case of **metal/semiconductor hybrid structures**, metal decorated surfaces (**Figure 13d**) are formed where both components (metal and semiconductor) and their interfaces are exposed to reaction media. Such surfaces (metal decorated) can not only harvest broad range of solar radiation but also due to their special plasmonic property (LSPR will be described in the following section) the photocatalytic properties are improved. These hybrid surfaces are also important for their non-plasmonic properties. In which the large metallic structures in combination with the semiconductors are limited to show their LSPR properties but can enhance light harvesting properties by other effects (see following subsection), which can be used for the many useful applications like CO<sub>2</sub> reduction, and hydrogen production (water splitting).

## 2.3. Enhancing Photocatalysis by Metallic NPs

### 2.3.1. Plasmonic Contribution of Metallic NPs

Inadequate visible light response is one of the major reasons of low efficiencies of  $\text{TiO}_2$  as photocatalyst. Therefore, this section is mainly focused on the special properties of metal NPs that show characteristic opto-catalytic feature by a special interface formed by semiconductor and metal. Metal thin film and NPs can interact with UV and visible light via their unique property of surface plasmon resonance (SPR) and LSPR, respectively. In former case SPRs propagate on a metallic surface and in latter, SPRs are localized on nanoparticles that give rise to improved light harvesting and catalytic properties in combination with semiconductors.

SPR occurs when plane-polarized light interacts with a thin metal film (with a negative real and small positive imaginary dielectric constant) under total internal reflection, then, a non-radiative plasmon wave propagates parallel to the interface between the dielectric and metal thin film and creates the electron charge density (*Figure 14*) [44,45]. Similarly, plasmonic metal NPs efficiently absorb solar light through localized LSPR that is caused by the light interaction with conductive metal NPs smaller than the wavelength ( $d \ll \lambda$ ) of incident light. The exposed light on the NPs displaces the electrons from their equilibrium state (*Figure 15*). The redistribution of surface charge creates a restoring force that allows these distorted electrons to oscillate at a certain frequency and as a result a dipolar field is generated outside the particle. Furthermore, this absorbed energy can also be re-emitted in the form of light or heat.

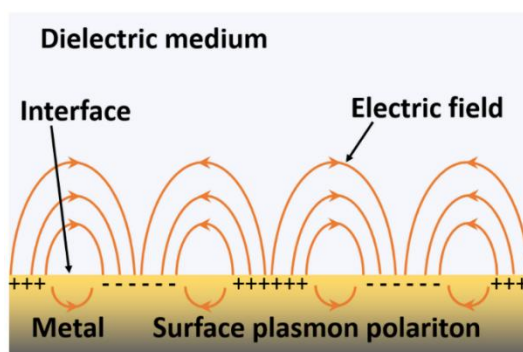


*Figure 14* Surface plasmon resonance (SPR) phenomenon at metal-dielectric interface, modified from [46].

The plasmon resonance frequency depends on many factors including type of the metal, NPs size, shape, inter-particle spacing, filling factor, as well as the dielectric function of the surrounding medium [45].

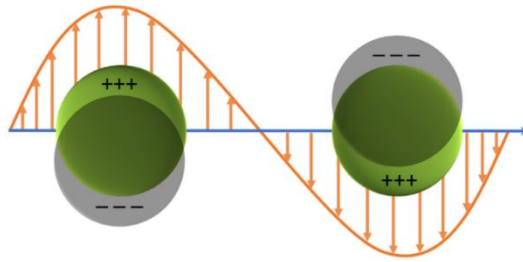


**Figure 15** LSPR phenomenon observed on so called free electron metals (like noble metals and Al) NPs, modified from [46].

Faupel et al. showed that noble metals nanoparticle (because of their low interaction) plasmon can be easily tuned by simply changing the filling factor and subsequently nanoparticle size (due to the increase in inter-particle interaction) [47]. The decrease in inter-particle distance (upon increase in particle size) strongly enhances the field between the particles (plasmon coupling) that caused the broad band absorption (**Figure 16**). Additionally, authors also showed that choosing alloy NPs and adjusting their composition also tune the plasmonic behavior. In 2004, Biswas et al. showed that plasmonic properties of single and alloy NPs consisting of Au, Ag and Cu noble metals embedded in a polymer dielectric matrix can be individually tuned, depending on the type of metal and alloy combination [23]. Similarly, many studies were performed on these noble metal NPs to observe their plasmonic and electrical properties at different filling factors, and their light scattering behavior was compared with the theoretical calculations (**Mie theory, Maxwell Garnett theory and Bruggeman effective medium approximation**) [45,47].

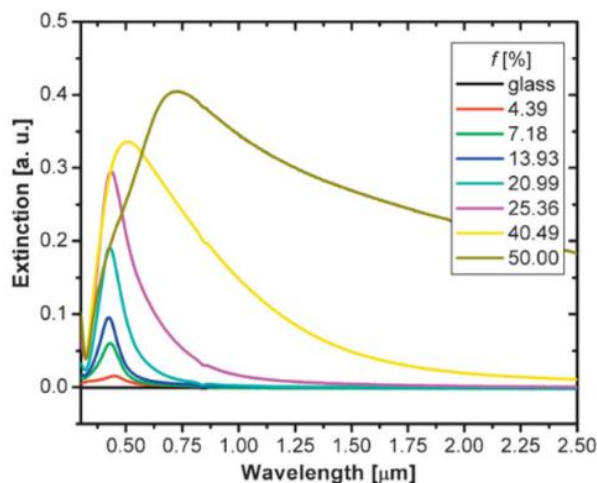


**Figure 16 (a)** UV-vis spectra of Au NPS at different filling factor. Taken from Faupel et al., edited version of [48].

Plasmonic NPs (show plasmonic behavior in the visible solar spectrum regime, from near UV to near infrared; for Ag, Au and Cu, respectively) in combination with TiO<sub>2</sub> provide outstanding properties. When these heterostructures (noble metal NPs decorated with TiO<sub>2</sub>) are irradiated with visible light, the electrons (also known as hot electrons) in the noble

metals NPs excited by LSPR can transfer to TiO<sub>2</sub>, facilitate redox reactions and enhance the photocatalytic efficiency in visible light. On the other hand, when these structures are irradiated with the UV light the noble metal NPs trap the photogenerated electrons (generated on TiO<sub>2</sub>) due to the presence of **Schottky barrier** (charge separation) and play a role as electron donors [8]. Many researchers showed that the photocatalytic efficiency of these structures is significantly higher upon UV and visible light irradiation than only under UV light. Recently, a study by Lin et al. on photocatalytic effect of Au-TiO<sub>2</sub> structures showed a systematic effect of the ratio of UV and visible light intensity on photocatalysis [49]. In this, the authors illustrated the effect of gradual increase of visible light irradiation by keeping UV irradiation constant. Initially (at very low visible light) the plasmon effect was low but became negative by increasing visible light (increased recombination of photogenerated holes at TiO<sub>2</sub> by plasmonic hot electrons transfer), and upon further increase in visible light irradiation (compared to UV) positive effect of plasmon was increased. Such studies have improved the understanding of the photocatalytic behavior and explained different phenomena occurring at the metallic NPs and semiconductor interfaces.

In addition to the noble metal plasmonics, there has been growing interest in the study of Al plasmonics. Nevertheless, due to the difficulty in the preparation of metallic nanostructures there are only a few studies in literature available so far. Al NPs (decorated on TiO<sub>2</sub>) prepared by lithography, nanosphere lithography (NSL) and other chemical synthesis methods have shown successful plasmonic photocatalysis in both, UV and visible solar spectrum.

In 2015, McClain et al. presented a systematic scattering spectrum of a series of Al nanocrystals (*Figure 17a*), which revealed a redshift with increasing nanocrystal size (SEM images in *Figure 17b*) [26]. The authors also compared the experimental dark-field spectra with the theoretical calculations obtained using Mie theory for similarly sized crystals (*Figure 17c*). Additionally, they also commented on the high stability (presence of protective oxide cover) of Al NPs, that can promote Al to be used as an alternative to gold and silver noble metals.

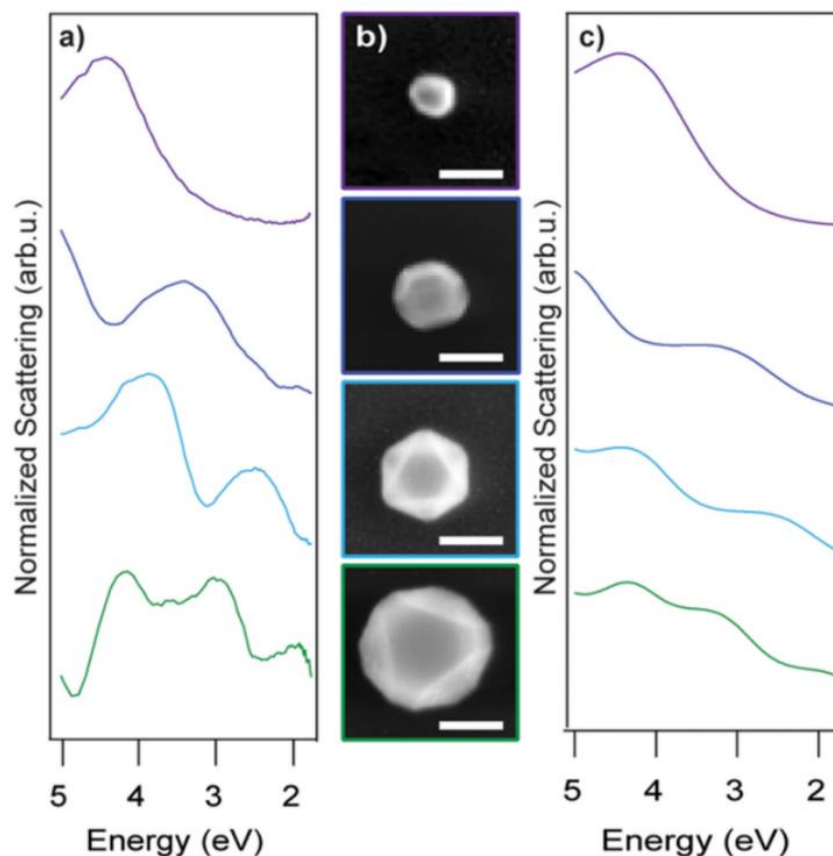


**Figure 17**(a) Experimental dark field spectra (b) SEM images (c) Theoretical calculation of 80, 120, 155, and 220 nm (top to bottom) nanocrystals (scale bar 100nm), taken from Hala et al. [26].

Recently, Honda et al. proposed that Al/TiO<sub>2</sub> structures may increase the photocatalytic properties, due to the tunable plasmonic properties of Al [50]. Authors showed that less than 40 nm Al NPs were more effective in the deep-UV region to enhance the photocatalytic activity of TiO<sub>2</sub>. Moreover, other research showed that periodic arrangement of metal NPs on TiO<sub>2</sub> leads to a strong LSPR hot-electron generation and consequent enhancement in the redox reaction rates under visible light illumination (Piot et al., 2015 [51]). In addition to photocatalytic enhancement, Al NPs aggregates are also proposed to be used for SERS enhancement applications (at around near-infrared wavelengths) where oxide cover present on metal NPs surface supports molecule-substrate interactions (Tian et al., 2017 [52]).

### 2.3.2. Non-plasmonic Contribution of Metal NPs

In addition to plasmonics, metal-TiO<sub>2</sub> hybrid structures also enhance photocatalytic efficiency by a non-plasmonic electron transfer process. As in single component, semiconductors like TiO<sub>2</sub> show low photocatalytic efficiency since the majority of the photogenerated charge carriers undergo recombination. Many studies showed Au decorated TiO<sub>2</sub> structures improve the photocatalytic properties upon UV irradiation [53]. In such

system, UV light excites electrons at the TiO<sub>2</sub> surface that are transferred to Au, functioning as charge separation and strongly enhances redox reaction. Oxidation and reduction reactions occur at Au and TiO<sub>2</sub> surfaces, respectively. Such process is alternative to plasmon enhanced photocatalysis and known as **synergistic effect of photocatalysis** [53].

In addition to synergistic effect, nano-scaled metal decorated semiconductor NPs can also improve catalytic properties as shown in *Figure 18*. Such catalytic reactions work through electron relay effect in the presence of reducing agents like NaBH<sub>4</sub> (because BH<sub>4</sub><sup>-</sup> ion has high electron injection capacity). Au NPs assist electron transfer from BH<sub>4</sub><sup>-</sup> ion to the dye molecules for enhanced dye degradation process. In 2017, we showed the ultrafast catalytic reduction of dye molecules via Au decorated ZnO/CeO<sub>2</sub> heterostructures [42]. In this, Au loading provides more prominent effect on catalytic behavior of ZnO/CeO<sub>2</sub> heterostructures.

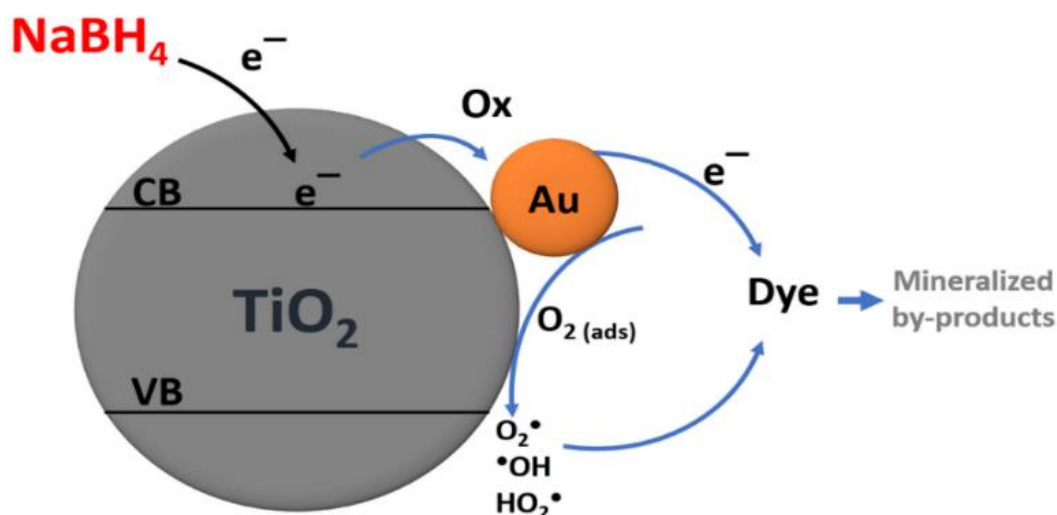


*Figure 18* Proposed mechanism for the catalytic reduction of dye by electron relay effect in the presence of NaBH<sub>4</sub>, modified form [54].

Besides NPs, microparticles of noble metals (where, particle size  $\gg \lambda$ ) with semiconductor structures have also importance in light harvesting applications. Such materials with sharp structures are proposed to show high electron transfer capabilities because of antenna effect (enhanced local electric field) which in turn leads to increased local chemical reduction (such as CO<sub>2</sub>) at their surface. Light irradiation on semiconductor surface transfers electrons into these larger structures of noble metals (which do not show plasmonic behavior) that not only enhance photocatalytic effect (energy application) but are also used for SERS applications.

# Chapter 3. Methods

In this chapter the methods relevant to the synthesis and characterization of thin films, nanoclusters and nanostructures employed for the current research are presented. Firstly, the process of sputtering and its effect on the thin film structures development are briefly explained. Then follows a description of the process of nanoclusters formation using gas aggregation source (GAS) and nanostructures growth using photocatalytic synthesis. At the end, the analytical methods used to characterize the synthesized thin films, nanoclusters and nanostructures are briefly described.

## 3.1. Preparation of Thin Films and Hybrid Structures

### 3.1.1. Sputtering of Thin Films

Sputtering is a thin film deposition technique and comes under the category of **physical vapor deposition** (PVD). During sputtering a solid surface is bombarded with energetic ions and the adjacent collisions cause the surface atoms to be detached and the morphology of the surface gets modified. It relates to the billiard ball model where the momentum of the cue ball (energetic ions) is transferred to the closed pack rack of balls (surface atoms). The principle of sputtering has been known since 1852 (introduced by W.R. Grove) [55] and developed as thin film deposition technique by Langmuir in 1920 [56]. Recently, pulsed sputtering technique is one of the mostly used sputtering processes for developing thin films.

The use of **direct current** (DC) planar diode is the simplest form of sputtering where plasma (generated by an electric discharge by applying potential difference between two electrodes) is used to produce the ionized gas to cause sputtering or erosion. The positive ions in the plasma are attracted by the negatively charged cathode (target). Depending on the energy, mass, incident angle of colliding ions and binding energy of the target atoms, these ions can bounce back, adsorb on the surface and implant or kick-off the atoms from the target surface.

If enough energy is transferred to the ions, collision can displace the atoms of the target. The minimum threshold energy is around 10 eV that provides very limited cascade (*Figure 19a*). Upon increasing ion energy above 10 eV, a series of collisions provide a linear cascade (*Figure 19b*) and at high energies, collisions occur between simultaneously



moving particles with very dense collision cascade which may lead to the local melting (*Figure 19c*).

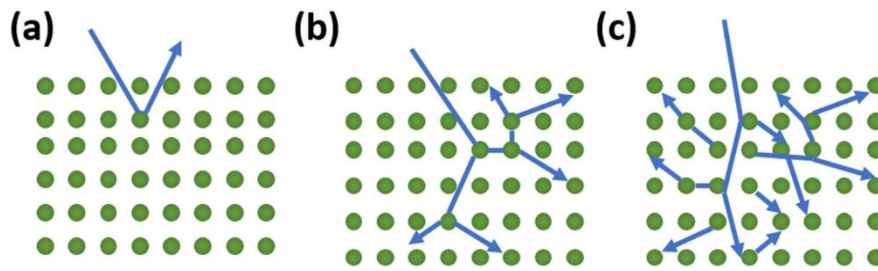


*Figure 19* Collision cascade created by ion collision to the target surface with the increasing energy (a) single collision (threshold), (b) linear cascade and (c) spike regime, modified version of [57].

Typical parameters that affect the sputtering rate are usually gas ions (their state of aggregation, energy and angle of incidence), the target material (its elemental composition, bulk and surface structure) and the target temperature (mainly on the phase transitions). Additionally, these parameters are important to determine the sputtering efficiency. The sputtering efficiency is defined in term of the sputtering yield that is the ratio between the number of sputtered target atoms and the incident number of ions.

In a simple DC sputtering, high pressure is required to maintain the plasma, as very small fraction of gas is ionized (ionization rate less than 0.1%) which leads to the low sputter rate. By decreasing the gas pressure or increasing the gas ionization efficiency the sputter yield can be improved. Gas ionization can be improved by trapping of the secondary electrons near target surface which rise the plasma density. Normally, an electron, when knocked out of the target surface, drifts almost in a straight line between cathode and anode. Electric and magnetic field, both affect the motion of electron and direction. If the both fields are aligned perpendicular to each other, the electron moves in helix path. Upon bending the magnetic field (with linear electric field), this electron helix path is also bended. The force observed on the electron can be calculated by **Lorentz Force** ( $F$ ) and can be determined by the following equation (5):

$$\mathbf{F} = q_e(\mathbf{E} + \mathbf{v} \times \mathbf{B}) = m_e \mathbf{a} \quad (5)$$

Here,  $q_e$  is the charge of electron,  $E$  and  $B$  are electric and magnetic field strength,  $m_e$  is the mass of electron and  $a$  is the acceleration.

Incorporation of magnets to the diode sputtering is named as **magnetron sputtering**. In this, a series of magnets with alternating polarity are attached to the backside of the target

in a circle that produces curved magnetic field lines in-front of the target surface which trap electrons in helical path, as shown in **Figure 20**. This highly concentrated electron region near the target ionizes gas atoms and creates a denser plasma without the need of higher pressures. The high ionization efficiency of gas is responsible for high current along the plasma. Therefore, at constant pressure, the discharge current increases with the discharge voltage. This relationship is expressed as follows in (6):

$$I = kV^n \quad (6)$$

Here,  $I$  is the current,  $V$  is the voltage,  $k$  is constant and exponent  $n$  is a measure of magnetron efficiency.

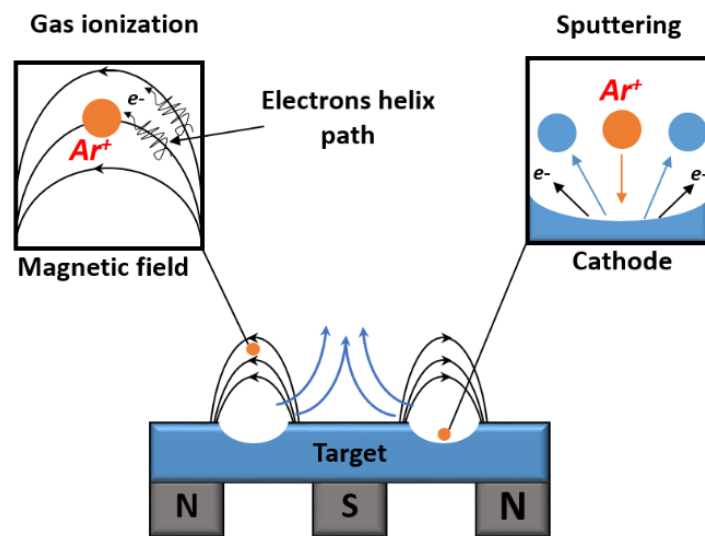


**Figure 20** Magnetron sputtering process: electrons trapping in magnetic field and ionization of gas atoms (top left) and subsequent improvement in sputtering process (top right), taken and modified from [58].

Not only the configuration of magnetic field but also the distribution of magnetic field lines affects the sputtering process. Balanced and unbalanced magnetic fields configurations are shown in **Figure 21**. The term balanced (type I) is used for the conventional magnetron in which central magnet strength is equal or stronger than outer ring magnet. In contrast, the unbalanced magnetron (type II) contains weaker inner magnet and stronger outer magnetic ring. Here, the magnetic fields produced by outer ring are not trapped by the inner magnet, so they increase the plasma length and produce ion bombardment on the substrate. The unbalanced magnetron sputtering process is beneficial for some applications where the ion bombardment increases the substrate current as well as the quality of the film.

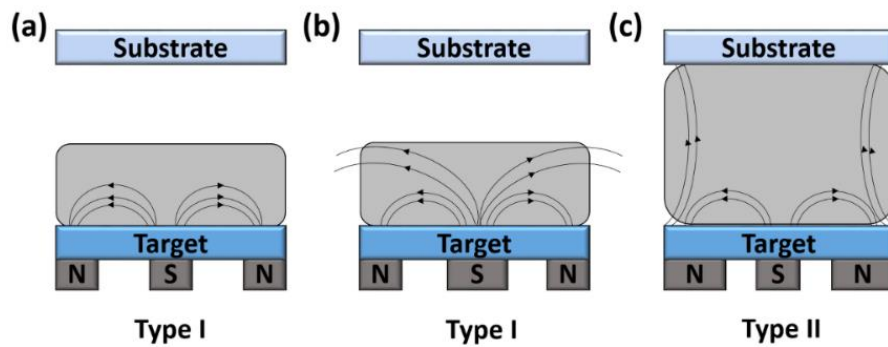


**Figure 21** (a-b) Type I magnetron (balanced) and (c) type II magnetron (unbalanced), proposed by B. Window & N. Savvides, 1986, modified version of [59].

### 3.1.1.1. Sputtering of Metal and Metal-Oxides

The DC magnetron sputtering is mostly used for the sputtering of conductive targets in which a DC power supply (a high-voltage DC source) produces a gaseous discharge. The positively charged gas ions strike the cathode (target), and the substrate and the vacuum chamber walls are the anode or at ground state. While using DC power source, the use of nonconducting target (metal-oxide) or reactive sputtering develop arc suspensions due to the charge accumulation on the target surface, that can damage a target by local melting or degrade the quality of the film.

In contrast, **Radio Frequency (RF)** magnetron sputtering offers an advantage over DC while it can sputter electrically non-conductive targets by using a high voltage RF source that is mostly at 13.56 MHz frequency. At such a high frequency the electrons (due to their low mass) can instantaneously respond to a rapid varying field without affecting heavier ions. The high energy transferred to electrons by changing electric field produces in-phase collisions. Before switching the electric field direction, a fraction of electrons is accelerated to ionize the gas, and after switching they move back in the opposite direction (towards target). In the whole process the distribution of energetic electrons increases, which leads to higher gas ionization with the decrease in the discharge impedance and as a result, no net current does flow. The main disadvantage of RF sputtering in addition to expense and reliability is the low deposition rate.

Compared to RF sputtering, the sputter rate can be efficiently enhanced with the use of pulsed DC magnetron sputtering. It can control the stoichiometry of the deposited film and arcing on the non-conductive target is hindered by using pulsing source, too. In **Figure 22a**, typical pulsed power signal supplied to the magnetron is shown. Another advantage of this technique is that the frequency used for pulsing is much lower (typically 50-250 kHz) compared to RF magnetron sputtering.

Generally, the discharge voltage cycles are highly negative with very low positive voltage. The low positive cycle attracts electrons to prevent charge buildup (*Figure 22b*) and a high negative pulse cycle produces normal DC sputtering (*Figure 22c*). The low mass and high mobility of electrons allow the cycle to be very short and provide efficient sputtering without arcing and local melting.

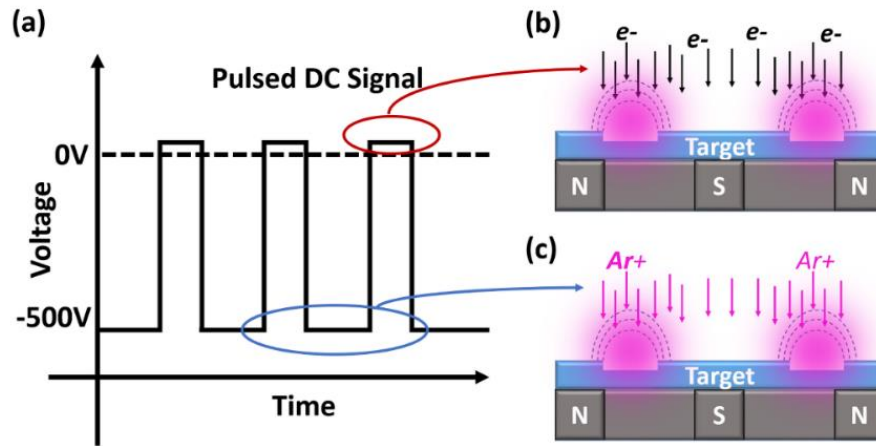


*Figure 22* Pulsed DC magnetron sputtering process. (a) Graphical illustration of time resolved pulse waveform during Pulsed DC sputtering, (b) weak positive pulsed cycle allows neutralization of the developed charge (electrons) that develops during the negative pulse cycle and (c) high negative pulsed cycle (left) allows normal sputtering of the surfaces [60].

In reactive sputtering a hysteresis behavior can be observed by gradually increasing and decreasing the reactive gas flow. A typical relation between the reactive gas flow against pressure, discharge voltage and deposition rate are displayed in *Figure 23*. Upon increasing the reactive gas amount (during sputtering), abrupt changes in the total pressure, discharge voltage and deposition rate are observed: while the total pressure is rapidly increasing and a fall in the voltage and deposition rate occurs (*Figure 23a-b*, respectively).

This hysteresis is noticed due to the change in the state of target surface that classifies this process into three different phases. The first phase is called **metallic**, where the amount of reactive gas is very low (metallic target), and high deposition rate of sputtering is achieved. In reverse, at very high amount of reactive gas, very low deposition rate is achieved because of the formation of a reactive compound on the metallic target surface; this phase is the **poisoned** one. The phase between the metallic and poisoned phases is the **transition zone** where the hysteresis behavior is observed, and the stoichiometry of the reactively sputtered film can be controlled within.

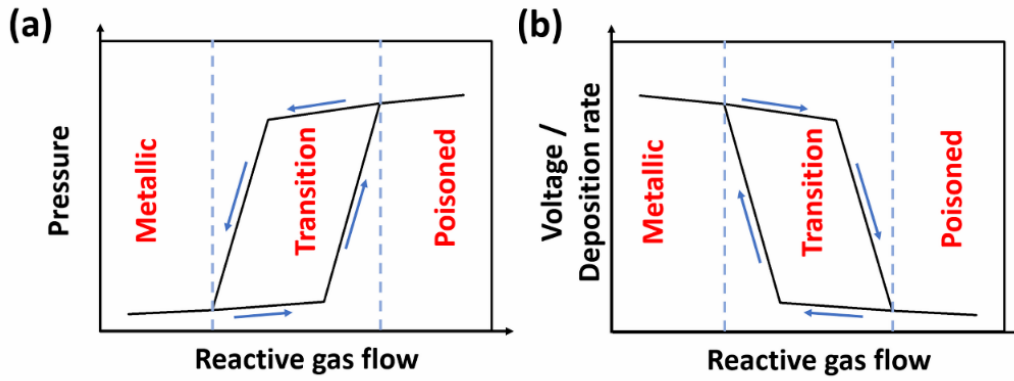


**Figure 23** Reactive gas flow as a function of (a) pressure and (b) voltage / sputter deposition rate during reactive sputtering of metallic target [55].

### 3.1.1.2. Film Growth during Sputtering Process

The microstructure and morphology of the film are related to the mobility of the adatoms during growth. The energy is transferred to the atoms by thermal effect, ionic bombardment and chemical reactions to the substrate. The effects of these mechanisms on the thin film growth can be explained by **structure zone model** (SZM). The major factors influencing SZM are substrate temperature, final working pressure, bias voltage (if applied to substrate) and thermal characteristics of target. In 1969, Movchan and Demchisshim [61] proposed that the microstructure of thin film depends on the normalized temperature that is given in (7).

$$\text{Normalized Temperature} = \frac{T_s}{T_m} \quad (7)$$

Here,  $T_s$  is the substrate temperature and  $T_m$  is the melting temperature of the target. Movchan et al. showed that in thin metallic film there are three metallic zones. The first zone is  $T_s/T_m < 0.3$ . This zone is formed by small and elongated grains, consists of columnar structure with porous morphology and weakly binding grains. The columnar structure is produced by a low diffusion, a low mobility of the atoms adsorbed by the substrate surface. In the second zone,  $0.3 \leq T_s/T_m \leq 0.45$ , the substrate temperature is increased homogeneously which leads to a higher diffusion of the adatoms, producing a dense structure with more binding among the columns. In the third zone,  $T_s/T_m > 0.45$ , the volumetric diffusion has high influence on the morphology of the film, that builds larger crystalline structures due to the re-crystallization.

Thorton et al. [62] further classified the zone model in 1974 according to the working pressure, as presented in **Figure 24**. The change in kinetic energy of sputtered ions and the mean free path of particles vary the properties of adatoms on the substrate surface. Thorton

defined  $T$  as a transition zone between first and second zones of model of Movchan et al. The  $T$  zone is prescribed as limit of the low porosity with dense and less rough surface than other two zones.

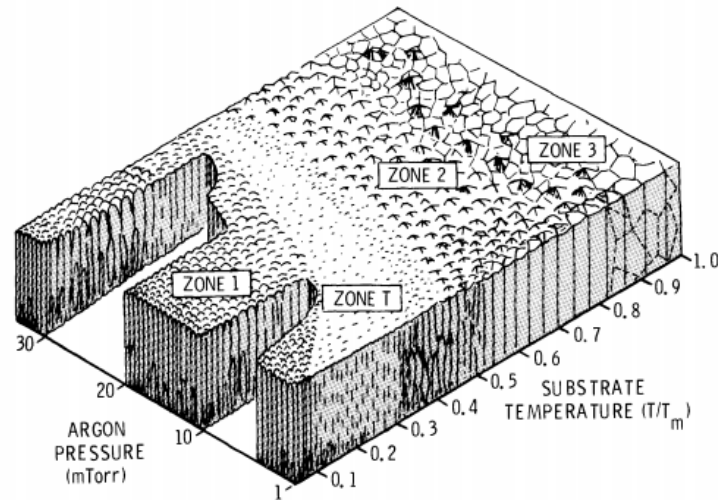


**Figure 24** Structure zone model correlating between the gas pressure (argon) and the normalized substrate temperature, Thonton, 1974 [63].

Additionally, in 1984 Messier and Giri found that the bias voltage applied to the substrate creates a non-linear limit between the first zone and T zone, because it increases the temperature due to high mobility and adsorption of the atoms, that results in the denser thin film and crystalline structures. Bias voltage above 100 V causes low adhesion between substrate and thin film and additionally increases residual stresses [64].

Interactions between adatoms and substrate surface also influence the nucleation and growth of the thin film. Depending on the interaction energies of substrate and film atoms, one of the following three models can exist (**Figure 25a-c**): **Volmer-Weber model** presents a three-dimensional separate island growth of adatoms by the nuclei until a continuous thin film is formed. When the adatoms encounter with the substrate the interaction between the neighboring atoms becomes larger than that with the substrate. In **Frank-Van der Merwe model** nuclei form monolayer island with a continuous film (layer by layer growth). Film grows two-dimensionally because the interaction between substrate and layer is stronger than neighboring layer atoms. In **Stranski-Krastanov model** both, layer by layer and three-dimensional growth are observed. Symmetry or orientation of the over-layers with respect to the substrate might be responsible for the production of this growth mode.

**Shadowing growth** is also observed in sputtered thin films after the initial layer or island growth, as shown in **Figure 25d**. It occurs due to the angular or oblique incident

deposition that results in the high film growth rate. Therefore, isolated columns are formed on these islands during the film growth [65].

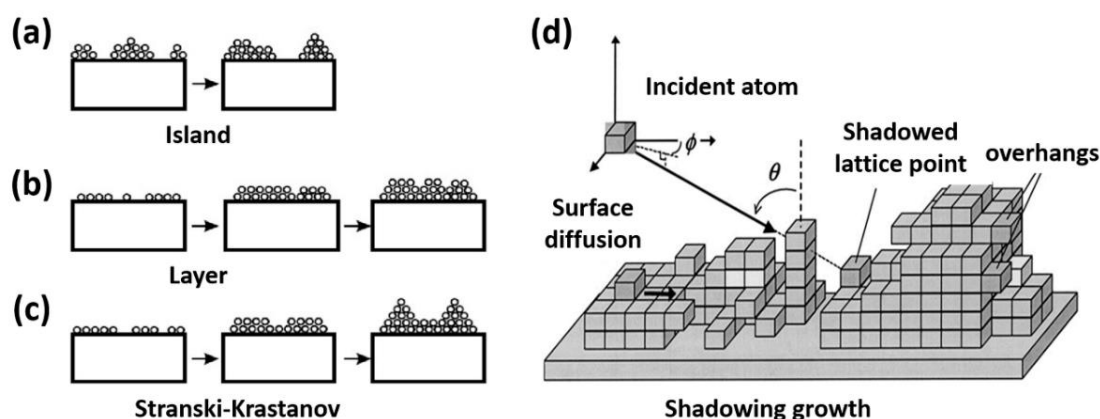


**Figure 25** Physical models of thin film growth: (a) Volmer-Weber model, (b) Frank-van der Merwe model, (c) Stranski-Krastanov model. (d) Shadowing growth, taken from [65,66].

### 3.1.2. Metal and Metal Oxide Clusters by Gas Aggregation Source (GAS)

Metal clusters are formed in the cluster source by evaporation or sputtering of metal atoms into a flow of cold inert gas at relatively high pressure between 10 to 100 Pa. In the sputtering-based GAS technique, metal clusters with large range of mean cluster sizes can be produced. The advantage of using sputtering-based cluster source is not only the production of large size range but also the high degree of ionization and possibility to sputter large variety of elements and alloys as a target material using discharge sputtering. Therefore, GAS technique can produce cluster from variety of materials ranging from metal to magnetic alloys [67,68].

Monodisperse metal and metal oxide nanoclusters are prepared by GAS [69,70]. These clusters with controllable size and morphology are primarily formed by successive single atom addition. The stability of the developed clusters is dependent on the condensation temperature, pressure and number of atoms in the cluster. Critical temperature, pressure and radius need to be controlled to stabilize a cluster. Following are the conditions to form a stable cluster:  $T < T_c$  ;  $P > P_c$ . Here,  $T$  is the temperature of aggregation zone,  $T_c$  is the critical temperature  $P$  is the pressure inside the GAS and  $P_c$  is the critical pressure.

To overcome a critical size, thermodynamics is important for the crystal stability. When atoms combine, the free energy of the formed nuclei changes (**Figure 26**) and effects the formation and stability of the clusters. Therefore, the potential to stabilize and form a cluster can be divided into three different regimes [71].



- (I) Nucleation occurs by the formation of small particles from successive combination of free atoms.
- (II) Small particles reach the size of the critical radius by passing the barrier of  $\Delta G^*$ .
- (III) Continuous growth of particles is favored.

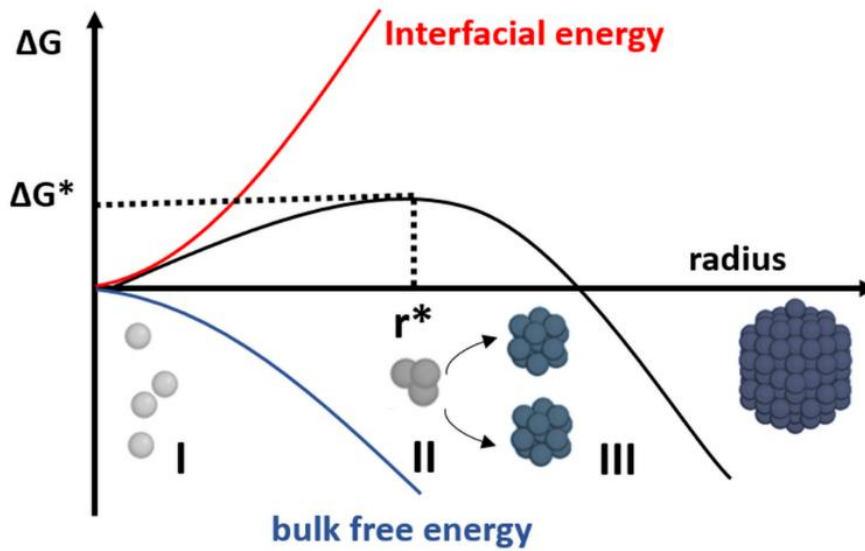


**Figure 26** The dependence of cluster free energy on the cluster radius according to the classical nucleation theory, modified from [58].

The first stable particle is obtained at the free energy maximum where a critical cluster size is obtained. Following formulas (8-9) can be used to determine critical radius of cluster:

$$r^* = -\frac{2\gamma}{\Delta G_v} \quad (8)$$

$$\Delta G^* = \frac{16\pi\gamma^3}{3(\Delta G_v)^2} \quad (9)$$

Here,  $r^*$  is the critical radius,  $\gamma$  is the interfacial energy,  $\Delta G_v$  is the bulk free energy and  $\Delta G^*$  is the critical free energy.

The schematic of complete sputtering-based cluster source is given in **section 4.2** (**Figure 32**) and the detailed description of magnetron sputtering used in the GAS is described in the **section 3.1.1.1**. In general, GAS consists of a long aggregation chamber with a small nozzle at the end that is connected to the main chamber. Therefore, the complete system consists of two sections: (1) aggregation chamber and (2) deposition chamber. The



process gas (mostly Ar or He) is introduced through the aggregation chamber (behind magnetron) and pumping is provided through the main chamber. Due to this a differential pressure is developed between these two chambers. A magnetron discharge can produce nanoclusters with variable size, depending on the magnetron power, type and flow rate of the carrier gas, temperature and length of aggregation zone, and nozzle size. The flow of process gas allows clusters to transport them out of the aggregation chamber because of the differential pressure. The flow of the nanoclusters is dependent on their size. It is hard for the big clusters to follow the gas trajectory. Also, the deposition of the clusters on the substrate follows the nozzle geometry. Circular nozzle provides circular geometry with thickness gradient (more cluster in the middle and less at the circumference). To obtain homogenous thickness of clusters on substrate, larger distance between nozzle and substrate is favorable. Clusters produced at high pressures are heavier because of the large number of collisions and low mean free path between the atoms. These heavy clusters can be lost inside the aggregation chamber as they are not able to follow the gas trajectory [72].

To produce metal oxide clusters, reactive gas is introduced in addition to the carrier gas that also affects the efficiency of cluster formation. The influence of the reactive gas mainly depends on the reactivity of the target material. Therefore, the reactive gas influences three stages of cluster formation: (i) Process on the target, (ii) cluster nucleation and (iii) further growth of cluster. If target surface is reacted with the gas (which allows the formation of the compound), sputter rate decreases dramatically. Therefore, the amount of reactive gas must be several orders of magnitude lower than the process gas. At the nucleation and growth stages, reactive gas may create the cluster seed and may also modify the binding energy, electric charge and may cause heating of the clusters. Therefore, admixture of the right amount of reactive gas is important at the nucleation and growth stage [73].

In order to improve the reactive sputtering process using DC magnetron reactive sputtering, pulsing of the DC power is decisive (see *Figure 22*). Pulsing process influences both, deposition rate and size of clusters. At high power pulses, more material from the target is sputtered which promotes number of collisions and increases cluster size. Somehow, the compound formation on the target can be controlled by varying the duty cycle, as it changes the sputtering time-on and time-off periods. During time on cycle, surface gets sputtered and time-off cycle surface reacts with the reactive gas. Thus, the decrease of time-off cycle decreases the compound on the surface of the target [74].

### 3.1.3. Metallic Clusters by Photocatalytic Reduction

Photochemistry is basically inspired by photosynthesis process and known as green chemistry. Activation of photoreactions by visible, ultraviolet and infrared radiations has advantage over thermal activation process. The second law of photochemistry described by Johannes Stark and Albert Einstein (also known as **Stark-Einstein-law**) states that for each photon of light absorbed by a chemical system, only one molecule is activated for a photochemical reaction [75]. The absorption of the photons of light by a material is described by the **Beer-Lambert Law** as follows in (10):

$$A = \epsilon cl \quad (10)$$

Here,  $A$  is the absorbance,  $\epsilon$  is the molar extinction coefficient,  $c$  absorber concentration of the absorbing specie (how strongly a specie absorbs light at a given wavelength) and  $l$  is the path length.

Wide variety of metal ions can be photoreduced using UV and visible light using certain dyes as sensitizers. The dye is the light excited specie and is reduced upon light irradiation. The reduced dye, in turn, reduces the metal ion and reverts to the normal form of the dye. By means of dye-sensitized photoreduction, those systems whose properties depend upon the valence state of a metal ion can be controlled by the light, and metal complexes have number of accessible excited states and spin multiplicity. These different states of reactivity can be tailored by electron transfer, irradiation wavelength and solvent medium. A small change in the photoreduction environment affects the electronic structure of the ion complex dramatically. In particular, the decrease in the polarity of medium increases the photoreduction process, as the medium is less polar than reactant [76].

Metals can be directly photoreduced within the solution by forming free standing metal NPs and can also be synthesized on-metal oxide surface. Chemical reduction and photochemical reduction are the two well-known methods to obtain nanohybrids. In the first method, reduction of the metal complexes can be favorably tuned using reducing agents such as ascorbic acid. In the later process, highly photoactive reducing agents (without chemical reducing agents) are used that adsorb these metal ions on the surface by forming nanohybrids. This process is also named as **photocatalytic reduction** in which metal oxides are used to reduce the metal ion complexes on the surface of semiconductor catalyst under UV irradiation [77]. The process of chemical and photochemical reduction of metal ions

(gold salt in solution) on metal oxide (TiO<sub>2</sub>) using reducing agent (e.g. ascorbic acid) and UV light is schematically illustrated in **Figure 27a-b**, respectively [78].

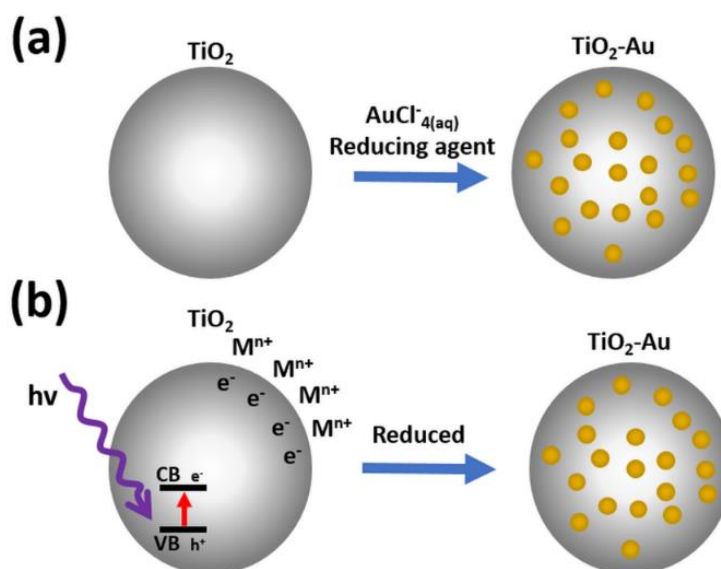
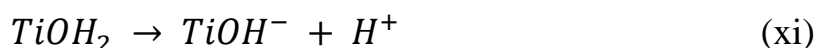


**Figure 27** Strategy for the synthesis of TiO<sub>2</sub> NPs decorated with NPs using (a) chemical reduction and (b) photoreduction, modified version of [78].

The photocatalytic reduction reaction is very slow, and the presence of organic donors (such as oxalic acid) accelerates the reduction process. Therefore, pH of the system is crucial for the photocatalytic reduction process. Change of pH of the solution changes the particle size, surface charge of reduced metal ion and band edge position of the semiconductor due to the amphoteric nature of semiconductor. High or low value of pH catalyst gets positive or negatively charged as shown in equations below by TiO<sub>2</sub> catalyst as an example (x-xi):



This amphoteric nature of semiconductor comes due to the formation of hydroxyl surface groups after chemisorption and dissociation of water molecules on the oxide surface, which is one of the main reasons that can affect the photocatalytic reduction process on semiconductor surface.

In addition to pH, many other parameters such as initial concentration of metal ion in solution, polarity, temperature, homogeneity of solution, irradiation time and intensity of UV light, photoactivity and the amount of the semiconductor metal oxide influence the effectiveness of photocatalytic reduction process [79,80].

The general mechanism of photocatalytic reduction of metal oxides is given as follows in (xii-xiii):



Here,  $MO$  is the metal oxide,  $M^{n+}$  is the metal ion,  $hv$  is the light irradiation,  $M^0$  is the reduced metal on the metal oxide surface. Additionally, the reaction mechanism of direct (by the high energy light source) and indirect reduction of  $Au^{3+}$  ions (low energetic light source and in the presence of  $TiO_2$ ) in an aqueous solution is also provided in the following **Table 1**.

**Table 1** Comparison of direct and indirect (by  $TiO_2$  thin film) reduction of  $Au^{3+}$  ions (including the overall reaction mechanism)[81].

<b>1</b>	Photoreduction of $Au^{3+}$ within the aqueous solution ( <b>Not observed</b> at low irradiation density!)	$\xrightarrow{\lambda} Au_{(aq)}^{3+} + 3e^{-} \rightarrow Au_{(s)}^0$	High Energetic Light Source (e.g. UV Laser)
<b>2</b>	Indirect photoreduction of $Au^{3+}$ at $TiO_2$ interface ( <b>Feasible</b> at low irradiation density!)	$\xrightarrow{\lambda} TiO_2 \rightarrow e^{-} + h^{+}$ $Au_{(aq)}^{3+} + 3e^{-} \rightarrow Au_{(s)}^0$	Low Energetic Light Source (e.g. UV LED)
<p><b>Over-all Reaction</b></p> $TiO_2 + hv \rightarrow TiO_2 + e^{-} + h^{+}$ $Au^{3+} + 3e^{-} \rightarrow Au^0$ $3/2H_2O + 3h^{+} \rightarrow 3/4O_2 + 3H^{+}$ $Au^{3+} + 4(OH)^{-} + 3/2H_2O + 3e^{-} + 3h^{+} \rightarrow Au^0 + 3/4O_2 + 3H^{+} + 4OH^{-}$ <hr/> <p><b>Net reaction</b> <math>Au^{3+} + 4(OH)^{-} + 3/2H_2O + 3e^{-} + 3h^{+} \rightarrow Au^0 + 3/4O_2 + OH^{-} + 3H_2O</math></p>			

In the following sub-section, the characterization techniques will be presented which are the base to determine the physical and chemical properties of the produced thin films, nanoclusters and nanostructures.

## 3.2. Characterization of Material and Photocatalytic Properties

### 3.2.1. Material Characterization

#### 3.2.1.1. SEM

**Scanning Electron Microscope (SEM)** is generally used for the surface analysis of thin films and structures. The technique is applied to observe and create an image of the surface morphology by scanning the surface (in a raster way) using high energy focused electron beam (instead of light beam). Primary electron (PE) beam scans the sample surface and produces many secondary products within the interaction volume of the surface and bulk material. This interaction volume is dependent on the energy, elastic and inelastic scattering of PE beam and the material under observation. The produced signals are backscattered electrons (BSE), secondary electrons (SE), and characteristics X-rays. SE are low energy electrons (<50eV) and generated by inelastic scattering of the primary electrons. BSE are high energy electrons (>50eV) and generated by elastic scattering in much deeper range of interaction volume and contain depth information. BSE mainly determine the material contrast, as backscatter coefficient is strongly dependent on the atomic number of the material. The most frequently used signals for the creation of images are the SE and BSE. Large number of created SE generated by the interaction of PE are efficiently detected by in-lens detector, which is placed above the objective lens (to obtain high efficiency to collect low energy SE). The quality of obtained image depends on the type of detector (SE or BSE), electron beam voltage, extractor voltage, tilt angle and conductivity of the sample. Surface charging is a major problem (due to the electrons) while analyzing non-conductive materials by SEM. To avoid this problem, surface is coated with a thin conductive film (e.g. gold or carbon graphite thin film). Additionally, materials are also identified by using generated X-rays that are analyzed using energy dispersive X-rays (EDX). EDX detector reveals the chemical composition, atomic number and phase differences of the material. Further details are given in [82].

#### 3.2.1.2. XPS

**X-ray Photoelectron Spectroscopy (XPS)** is a surface analytical technique to characterize the chemical properties of materials. It is used to precisely quantify the elemental composition including different electronic and chemical states of material. Surface analysis by XPS is carried out by irradiating monoenergetic soft X-ray beam on the

sample. Usually, Mg or Al K $\alpha$  X-rays are used with energies 1.25 keV and 1.49 keV respectively. Except helium and hydrogen all other elements can be detected by XPS. Penetration depth of these X-rays is very limited. It can make depth analysis between top 2 atomic layers up to 20 atomic layers and it is the least destructive technique between other spectroscopy techniques. To obtain depth chemical analysis of the multilayer coatings (above 10 nm), ion beam etching is employed in combination to XPS where the energetic ions beam can etch the surface of the multilayer coating and simultaneously analyzed by XPS. The basic principle of XPS is shown in *Figure 28*.

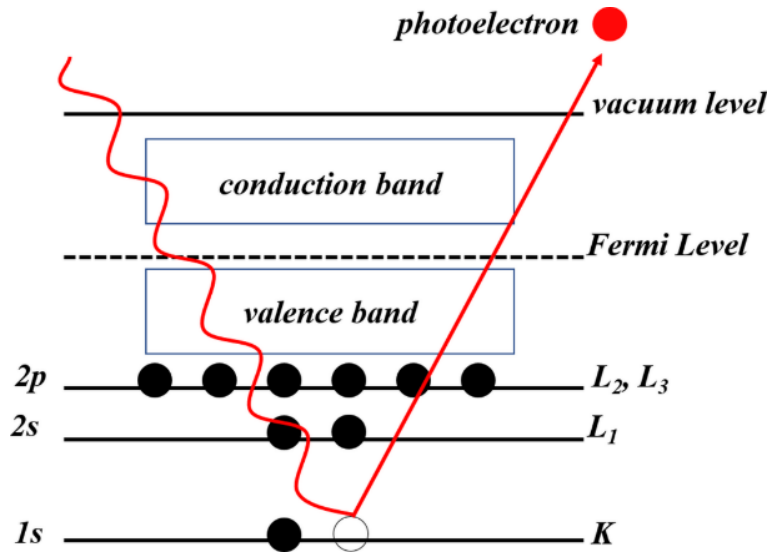


*Figure 28* Principle of XPS.

An X-ray photon with energy  $h\nu$  hits the surface of the material and knocks out an electron. Therefore, an electron with binding energy  $E_b$  with respect to the **Fermi level** is emitted from the atom with a kinetic energy  $E_k$  due to photoelectric effect by leaving a core hole behind. The binding energy  $E_b$  of the electron can be calculated by (xiv)

$$E_b = h\nu - E_k - \phi \quad (\text{xiv})$$

Here,  $h$  is Planck constant,  $\nu$  is frequency of the radiation,  $\phi$  is the work function of the spectrometer and  $E_k$  is the kinetic energy of the emitted electron.

The obtained spectrum by the analyzers (for each photoelectron) consists of the characteristic peaks of each element with respect to their kinetic energies. From the binding energy and intensity of a photoelectron peak, the elemental identity, chemical state, and quantity of a detected element can be performed. Additional details are available in [83].

### 3.2.1.3. TEM

**Transmission Electron Microscope (TEM)** is the structural analysis technique used to observe the crystallographic properties of thin films and surfaces. It can provide information about structure, texture, shape and size of the sample. To obtain TEM analysis sample needs to be electron transparent. The resolution of TEM is mostly dependent on highly focused electron beam which is defined as **probe**. The probe focuses a very small area on the specimen. The electron gun emits almost monoenergetic electrons with small wavelengths that are directly correlated with the spatial resolution. As the electrons pass through the sample, they are scattered by the electrostatic potential set up by the constituent elements in the specimen. After passing through the specimen they pass through the electromagnetic objective lens, which focuses all the electrons scattered from one point of the specimen into one point in the image plane. The image-recording system usually consists of the florescent screen for viewing and focusing the image. Both, bright field contrast (transmitted electrons) and dark field contrast (diffracted electrons) images can be obtained. Crystallographic structure of a material is estimated from the selected area electron diffraction patterns (SAED). Depending on the material properties planar defects, stacking faults, particle size, growth direction, crystalline and amorphous phases, crystal orientation and diffraction patterns can be obtained and analyzed. Additional details are available in [84].

### 3.2.1.4. Raman Spectroscopy

Raman spectroscopy is a highly used technique for crystal structural analysis of films and particles. It is a very fast method applied to analyze the molecular vibrations and reveal crystal structures by the interaction of laser light source with the sample. The characteristic spectrum produced by the light scattering depends on the vibrational and rotational modes of the molecule. Inelastic scattering of monochromatic light provides Raman scattering spectra (weak signal) that is induced by near UV, visible and near infrared range light. Filters are used to distinguish the reflected and scattered light. The signals obtained consist of anti-stokes, Rayleigh and stokes radiations as shown in *Figure 29*.

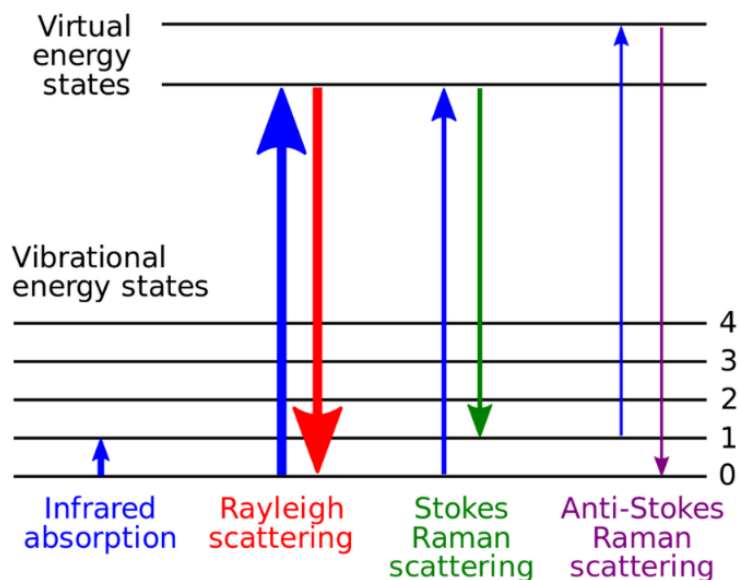


*Figure 29* Energy level diagram showing the states involved in Raman spectra.

**Rayleigh scattering** is the elastic scattering of light which is filtered out and not analyzed. Stokes radiation obtained at lower energy and anti-stokes radiations have greater energy as of Rayleigh radiation. The in-elastic scattering of light can be increased or decreased compared to the incident light which relates to the excitation of the molecular energy states. The total energy remains constant and energy difference depends on the initial and final state of molecule. If the final energy state is higher than the initial energy state, then frequency of the photons will shift to lower energy to conserve the same total energy- This shift is known as **Stock shift** and the opposite to this effect is known as **anti-stock shift**. The Raman scattering depends on the polarization change and observed as a function of frequency shift [85].

### 3.2.1.5. HIM

**Helium Ion Microscope (HIM)** is a type of microscope that is used for imaging and observing different surfaces. The main functionality is same as the one of SEM but instead of using electron beam, helium ion beam is used. The main advantage is the smaller probe size (short wavelength) and very less interaction volume. Compared to SEM, the secondary electron yield is quite high (allows imaging with extremely low current) to provide good surface resolution and better contrast compared to electron beam. The detectors provide information about topographic, material, crystallographic and electrical properties of the sample. Detailed information is available in [86].



### 3.2.2. Photocatalytic Analysis

Photocatalysis is the catalytic reaction involving light absorption by the substrate (according to IUPAC definition). To analyze the photocatalysis, most of the standards evaluate the activity of photocatalysts (upon UV irradiation) by using the test pollutants and analyze the physical or chemical change. These standards cover air purification, photosterilization, self-cleaning and water purification as listed in *Table 2*.

*Table 2* ISO standard test categories for different application of photocatalysis taken from [87].

App. Type	Test pollutant	Sample type and application
Air Purification	Removal of NO, acetaldehyde and toluene	Exterior: NO <sub>x</sub> removing paint, concrete and tiles Interior: Odor-removing paint
Photosterilization	Bacteria (antibacterial effect)	Photo-induced sterile surfaces
Self-cleaning	Methylene blue Oleic acid (water contact angle measurement)	Self-cleaning glass, concrete, tent or awning materials and tiles
Water purification	Photobleaching of methylene blue, methylene orange and Rhodamine-B Oxidation of DMSO	Water purification units

#### 3.2.2.1. Photocatalysis in Aqueous Solution (Wet Conditions)

Photocatalysis under aqueous test environment is typically performed to determine the self-cleaning and air cleaning activity of semiconductor thin films. To analyze the efficiency of the photocatalysts organic test dyes are used. Mostly used standards for testing the activity of thin film semiconductors are **ISO 10678:2010** and **DIN 52980:2008-10**. In these standards the photocatalytic activity of surfaces is determined by the degradation of the dye molecule in aqueous solution using artificial UV radiation that characterizes the ability of photoactive surfaces. Investigation of the dye degradation rate in aqueous solution is carried out via UV-vis spectrometry that is usually used to determine the color change (dye mineralization) of solution [88].

These standard analytical methods are time-consuming and determine the photocatalytic activity of the materials indirectly (not directly on the surface of the photocatalytic material), therefore new methods are under development to achieve fast and reliable analysis of photocatalytic thin films. Another method recently used to determine

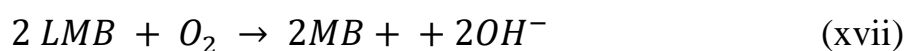
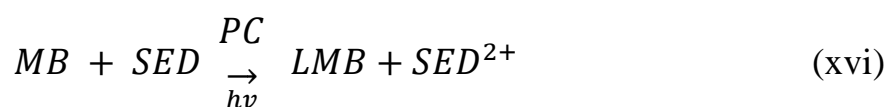
the photocatalytic activity directly on the thin film surface is provided in the following subsection.

### 3.2.2.2. Photocatalysis In Air (Dry Conditions)

In addition to standard test methods, many alternative methods are being developed to analyze the activity of semiconductors. One of the earlier approaches was inspired by photocatalyzed dye degradation in air–solid systems (self-cleaning surfaces) in which the colorful organic dye was applied on the surface of photocatalyst and analyzed by UV-vis reflection spectroscopy upon light irradiation [89]. Such analytical approach showed the direct surface analysis of photocatalytic activity of semiconductor thin films. The simplest form of the complex reaction occurring on the photocatalyst (PC) surface is given as follows in (xv):



Recently, to obtain fast and rapid analysis of photocatalytic thin films *The Explorer* surface activity indicator ink has been developed [90]. The ink can be applied on the surface of the photocatalyst in the form of brush or by manual writing. The images of the indicator ink in the form of two different products are shown in *Figure 30*. This blue colored ink consists of chemically modified MB (MB in combination with sacrificial electron donor (SED), such as glycerol) [91]. The SED transforms MB into its colorless state LMB (instead of mineralization) upon activating photocatalyst. The LMB is as mentioned earlier the reduced state of MB that can revert to its blue color (MB) as it reacts with the atmospheric oxygen. The mechanism of this reaction is shown in (xvi-xvii) [92].



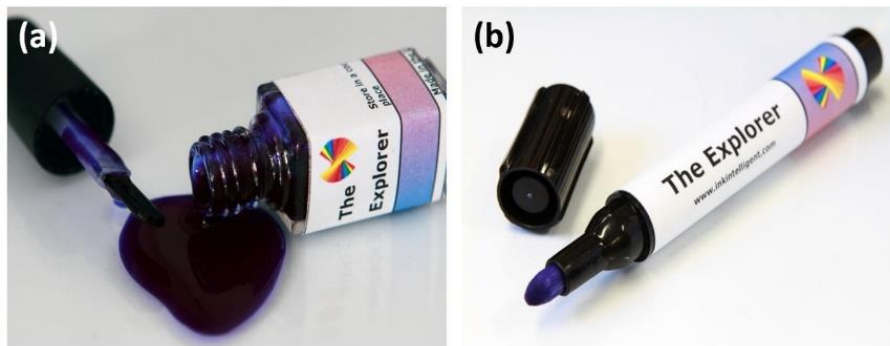


**Figure 30** The market products (**the Explorer**) of photocatalytic test ink used for assessing photocatalytic activity of photocatalytic materials, in the form of (a) ink (applied on samples by paintbrush on the photocatalyst surface) and (b) pen (the ink is applied by writing on the sample surface).

The use of stabilizing agents within these test products and uncertainty of the deposited ink thickness (using paintbrush) may lead to the improper photocatalytic analysis. Additionally, the chemical reactivity of the sample with these reducing agents may also trigger the color conversion of the test ink which may also lead to the inappropriate analysis and comparison between different materials. Therefore, a new approach to overcome these limitations is developed in the current study (without using any SED and additional reducing agents). The mechanism of the analysis is described in *section 4.4.2.2*.

# Chapter 4. Experimental

In this chapter the detailed experimental procedures to prepare TiO<sub>2</sub> thin films, Al nanoclusters and Au nanostructures on TiO<sub>2</sub> films are presented. Firstly, the procedure of TiO<sub>2</sub> films preparation by sputtering and spin coating is described and then, the Al nanoparticles development by sputtering-based GAS technique is explained. Afterwards, a synthesis process of Au nanostructures growth on photocatalytic TiO<sub>2</sub> films is introduced.

## 4.1. Preparation of TiO<sub>2</sub> Films

A highly photocatalytic TiO<sub>2</sub> thin film was prepared by pulsed DC reactive magnetron sputtering (see *section 3.1* for detailed information) using custom-made vacuum deposition chamber. The magnetron consisted of water cooled copper head (with additional grounded housing) and planar neodymium permanent magnets (cubic dimension) that were arranged in circular configuration, as of a balanced magnetron. The intensity of their magnetic field lines running out through the target was reduced due to the target thickness, but was still intense enough to trap electrons, ionize gas and increase sputter rate. The metallic titanium target of 3 mm thickness was mounted in front of the magnetron. This complete assembly of magnetron was shielded with stainless steel cap (surrounding the magnetron) with less than 1 mm gap between the magnetron and the shield to prevent unwanted discharge. Argon (process gas) was introduced through this shield containing small ducts that provide directional flow to the gas towards the target surface. Additionally, a rotatable substrate holder and quartz crystal microbalance (QCM) were placed opposite to the sputter target. The complete chamber was kept under vacuum to produce high purity TiO<sub>2</sub> thin films via turbomolecular pump (TMP) (Pfeiffer Vacuum, HiPace 400) assisted by a rotary pump (Agilent Technologies, SH-110). The schematic of the sputtering system used for TiO<sub>2</sub> sputtering is depicted in *Figure 31*.

Prior to the sputtering, the base pressure of the chamber was adjusted about  $5 \times 10^{-5}$  Pa. The substrate and the chamber housing were kept at ground state and magnetron source was connected to DC power supply having pulsed signal produced by pulsed generator. The output power was pulsed at a frequency of 50 kHz with 55 % duty cycle to reduce the oxidation and the poisoning of the target surface. The trigger signal was rectangular with a peak-to-peak amplitude of 5 V.

The plasma was generated by the ionization of argon, and to acquire a high sputter yield, argon gas (flow rate of 250 SCCM) was applied directly to the Ti target in the presence of controlled oxygen flow (flow rate of 10 SCCM).

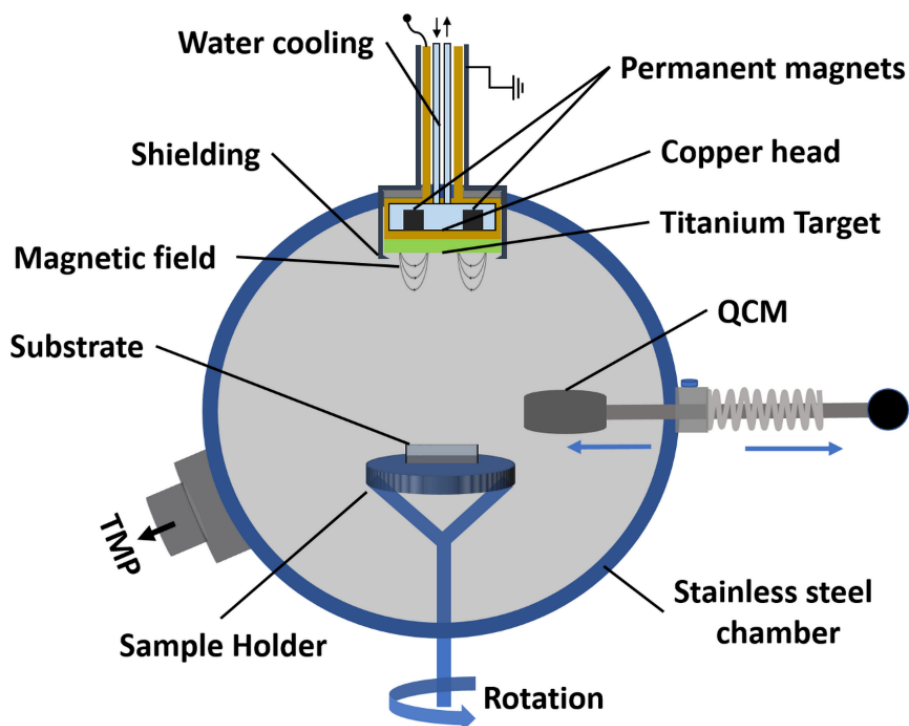


**Figure 31** Schematic cross-section of sputter deposition system used to deposit TiO<sub>2</sub> thin films.

Before sputtering, substrates (polished quartz glass and silicon) were cleaned in the ultrasonic bath using three different solvents (acetone, isopropanol and water, respectively) and subsequently dried with nitrogen gas. Following the sputtering, TiO<sub>2</sub> thin films were heat-treated by directly placing the sample into an oven, which was pre-heated to 650-700 °C for 1 hour, and afterwards quenched in air.

Reference TiO<sub>2</sub> thin film was prepared by spin-coating. 5 % (w/v) aqueous slurry of TiO<sub>2</sub> NPs (Sigma Aldrich 637254) with homogenous solution was prepared by ultrasonication for 15 minutes. In order to form thin film, 50 µl of the TiO<sub>2</sub> NPs slurry was dropped on the center of the pre-cleaned polished quartz glass substrate. Then, the substrate was rotated at high speed of 1800 rpm for 30 s in the N<sub>2</sub> gas atmosphere. Here, at the start the centripetal force combined with the surface tension of the solution pulls the slurry into an even covering. During spinning the solvent was evaporated by leaving the homogenous coating on the substrate. The film was then heat-treated in an oven at 200 °C for 1 h.

## 4.2. Preparation of Al NPs by GAS

Gas aggregation source was used to prepare Al NPs. The construction of the cluster source is shown in **Figure 32**. GAS chamber was mounted on secondary vacuum chamber (stainless steel), where the vacuum was applied via TMP and both chambers were separated by the small nozzle. The argon gas was introduced from the magnetron that creates a differential pressure between the GAS chamber and the secondary chamber. Furthermore, a rotatable substrate holder and quartz crystal microbalance (QCM) were placed opposite to the nozzle (in the secondary chamber). In this setup, differential pump, mass spectrometer, liquid nitrogen cooling and mass separator (mostly used in the usual Haberland type setups, [93]) were not applied. This has not only simplified the setup but also increased the productivity.

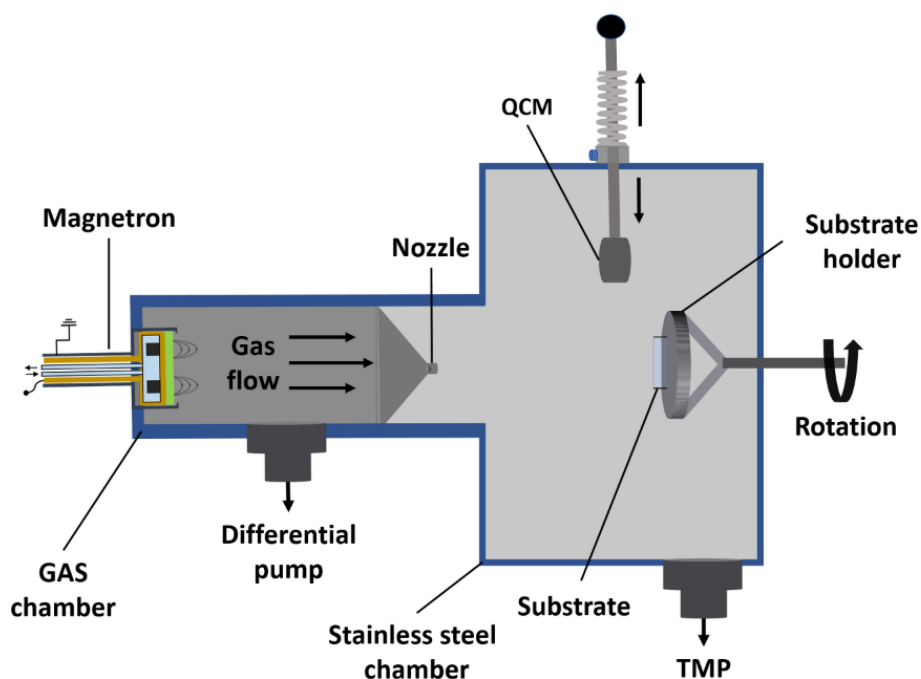


**Figure 32** Schematic cross-sectional view of GAS source

The cylindrical-shaped aggregation chamber consists of 10 cm diameter with 9 cm aggregation length and a nozzle (dimension: 0.3 cm length and 0.15 cm diameter) opening at the end connecting to the other chamber. Al clusters were produced using DC magnetron sputtering using 3 mm thick target. In addition to Ar (process gas), extremely low amount of O<sub>2</sub> was introduced during Al sputtering. Substrate to deposit prepared clusters was placed outside the aggregation chamber and the distance between the orifice and the substrate was around 30 cm. Main chamber was pumped with turbomolecular pump and kept under ultrahigh vacuum whereas pressure inside the cluster source was maintained at 10 to 15 Pa. Cluster size was controlled by changing the magnetron power and the deposition rate was

controlled by using QCM. Substrate was rotated during deposition to obtain homogenous distribution of clusters. Further parameters and the process are given in *section 6.2*.

### 4.3. Photocatalytic Deposition of Au Micro- and Nano Structures

To synthesize Au structures on TiO<sub>2</sub> films, Gold(III) chloride solution (Sigma Aldrich 16903-35-8) was used. A custom-made setup was constructed to perform photocatalytic reduction of Au nanoclusters on TiO<sub>2</sub> film. The setup consisted of a quartz glass cuvette, Teflon sample holder, magnetic stirring system with magnetic pill and UV LED mounted on the holder with LED power regulator. The schematic of the setup is shown in *Figure 33*.

TiO<sub>2</sub> thin film deposited on quartz glass or silicon substrate was immersed in 6.5 ml volume of 0.8 nM aqueous HAuCl<sub>4</sub> solution filled in the quartz glass cuvette (as shown in the schematic). Solution was stirred continuously by using magnetic stirrer. Further details to load gold on highly active TiO<sub>2</sub> films are given in *section 7.2.1*.

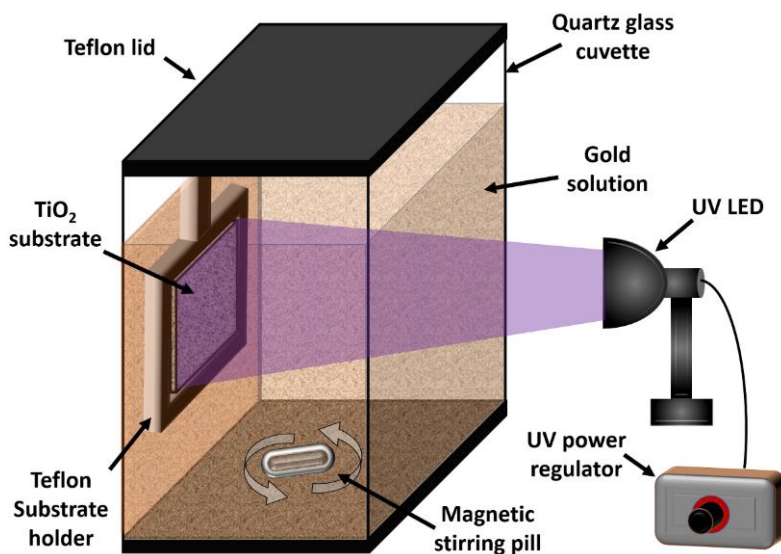


*Figure 33* Schematic representation of photocatalytic loading of Au on TiO<sub>2</sub> by photoreduction method.

Additionally, selective Au clusters structuring was performed by using a non-contact polymer mask. The polymer mask was placed on the quartz glass cuvette (in between the TiO<sub>2</sub> sample and UV LED) to block UV radiation and create shadowing of UV irradiation on the TiO<sub>2</sub> substrate. The illuminated and activated regions on TiO<sub>2</sub> film surface by UV irradiation (filtered by shadow-mask) provided high electron density to reduce gold on these significant areas similar to the patterns available on the mask template (see *Figure 71*, *section 7.2.4*).

## 4.4. Characterization

The analytical techniques including experimental parameters to reveal the properties of the prepared structures and samples are provided within this section.

### 4.4.1. Material and Surface Properties

#### 4.4.1.1. SEM

The morphology of the structures was studied by Supra55VP-Carl Zeiss, scanning electron microscope operated at low beam energy of 3 kV with a standard aperture size of 30  $\mu\text{m}$ . No conductive coatings were applied to the samples prior to SEM analyses in order to preserve the sample surface information.

#### 4.4.1.2. XPS

XPS analysis of the samples was obtained by Omicron Full Lab XPS system (VG Microtech XR3E2) with a double Al/Mg anode (VG Micro-tech XR3E2) and a hemispherical analyzer (VSW Instruments EA 125). The Al anode was operated at the power of 266 W (14.8 kV, 18 mA). X-ray beam was irradiated on the samples to quantify the kinetic energy and number of electrons on the sample's surface. Signals produced up to 10 nm surface depth were detected by the analyzer. Broad range of XPS spectra (using multiple detectors) were obtained for each sample and compared by the representative standard spectra given in the handbook of X-ray photoelectron spectroscopy [94].

#### 4.4.1.3. TEM

Structural analysis of samples was characterized via TEM using a Tecnai F30 STwin microscope (300 kV, field emission gun (FEG) cathode, spherical aberration coefficient Cs 1/4 1.2 mm). The samples for TEM investigations were also prepared by focused ion beam (FIB) milling using a lift-out method with a FEI Helios Nanolab system. Bright field images and SAED patterns were recorded to reveal structural properties.

#### 4.4.1.4. Raman spectroscopy

The Raman spectra of prepared samples was collected using confocal system equipped with a laser operating at a wavelength of 532 nm. Signals were obtained by the inelastic scattering of monochromatic light interaction with the sample. Many filters were used to screen the reflected and scattered light. The signals obtained were consisted of anti-



stokes, Rayleigh and stokes radiations. The Raman scattering obtained was dependent on the polarization change of the crystals and observed as a function of frequency shift

#### 4.4.1.5. HIM

The morphology of the structures was studied (in cooperation with University of Southern Denmark) by Orion NanoFab-Carl Zeiss, helium ion microscope at 30 keV beam energy and a probe current ranging from 0.5 to 1.1 pA. No conductive coatings were applied to the samples prior to HIM analyses in order to preserve the sample surface information

### 4.4.2. Photocatalytic Properties

#### 4.4.2.1. Photocatalysis in Aqueous Solution (Wet Conditions)

To determine the photocatalytic activity of the prepared films by standard test method, sample was immersed in an aqueous test solution of colorful MB dye (model organic pollutant). The photocatalytic properties were observed by observing the change in the color of the aqueous solution (by activating the TiO<sub>2</sub> surface upon UV irradiation) via UV-Vis spectroscopy. The schematic diagram of the setup used for the current work is given in *Figure 34*. Where the TiO<sub>2</sub> thin film deposited on quartz glass substrate is immersed into 6.5 ml aqueous MB solution (with an initial concentration of C<sub>0</sub>=10±0.5 μmol/l) filled in a quartz cell container and subsequently exposed to the UV light. While a UV LED (4.50 mW/cm<sup>2</sup>) operating at a wavelength of 365±10 nm was activating TiO<sub>2</sub> thin films, the in-situ change in the absorption spectra (at a wavelength of 664 nm) was recorded using in-situ UV-Vis spectroscopy system.

Additionally, to determine the photon efficiency following formula given in (27) is used:

$$\xi = \frac{R}{E_p} .100 \quad (11)$$

Here,  $R$  is specific absorbance and  $E_p$  is the photon irradiance. The specific absorbance of MB is calculated by the following formula given in (28):

$$R = \frac{\Delta A_\lambda V}{\Delta t \mathcal{E} d A} \quad (12)$$

Here,  $\Delta A_\lambda$  is the change in absorbance at maximum wavelength,  $\Delta t$  is change in time,  $V$  is the volume of the organic test solution,  $\mathcal{E}$  is the molar extinction coefficient,  $d$  is the

measured dye solution path length for UV-vis spectrometry and  $A$  is the area of the photocatalytic surface irradiated by UV light. Photon irradiance is determined by using following formula given in (13):

$$E_{p,av} = \frac{\lambda_{max} E_{av} 3600}{h c N_A} = \lambda_{max} E_{av} 30740 \quad (13)$$

Here,  $E_{av}$  is the average UV light intensity,  $\lambda_{max}$  is the maximum wavelength of UV light,  $h$  is the Planck's constant,  $c$  is the concentration of organic test dye,  $N_A$  is Avogadro's number.

These standards are basically inspired by the photocatalysis of NPs suspension, where the NPs with large surface can degrade bulk volume of test organic dye solution faster because of the extreme increase in specific active surface area. The increase of the active surface area of spherical nanoparticle with the decrease in its size is shown in the following *Figure 35*.

This mineralization process of the dye occurs on a longer timescale for thin films than the oxidative photobleaching of the dye, therefore, such methods are used for the lab scale testing applications where reliability and reproducibility of the process are the key parameters.

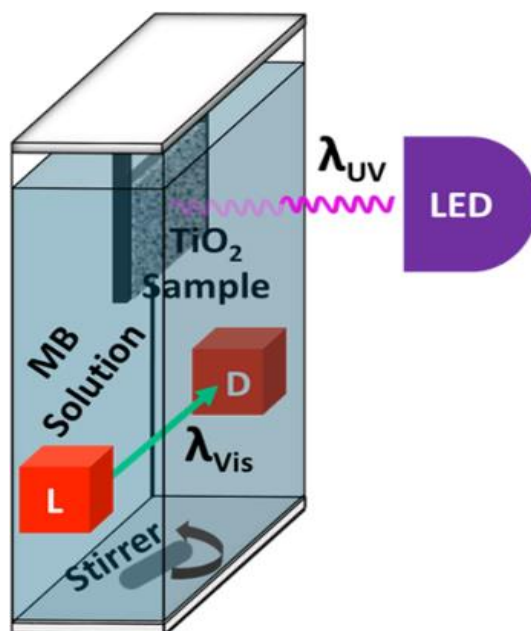


**Figure 34** Schematic representation of standard analysis method used to determine the photocatalytic performance of  $\text{TiO}_2$  thin films by observing in-situ bleaching of MB in-aqueous solution.

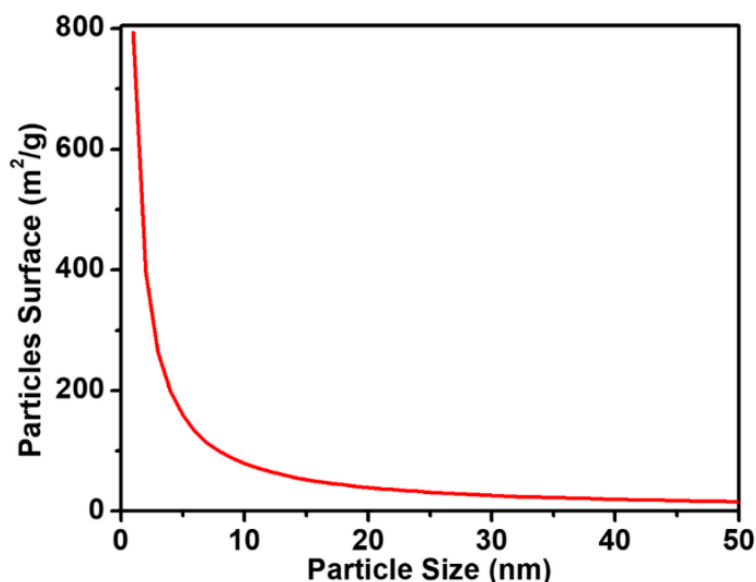


**Figure 35** Exponential increase of spherical particles specific surface area per unit mass with decreasing NP size.

#### 4.4.2.2. Photocatalysis in Air (Dry Conditions)

The photocatalytic performance of TiO<sub>2</sub> thin films is determined by observing bleaching of MB in-air. First, a thin MB layer was spin-coated on sputter-deposited and reference TiO<sub>2</sub> thin films. Prior to the spin-coating a diluted MB solution using de-ionized (DI) water was prepared. Following the ultrasonication at 20 kHz and 200 W for 30 min. and the MB solution was mixed by a magnetic stirrer operating at 200 rpm for 3 hours to make a homogenous solution. Before the spin coating the solution was filtered to eliminate any undissolved or agglomerated solid particle. Various spinning speeds and MB concentrations were tested to achieve homogenous MB thin layers. The thinnest MB layer was prepared using a MB concentration of 1.8 mg/ml and a spinning speed of 7000 rpm for 30 sec. Following a drying step at 40 °C for 6 hours, the bleaching of the MB solid layer (the change in the absorption at 580 nm) was tracked in-situ by UV-vis spectroscopy during UV exposure (4.50 mW/cm<sup>2</sup>). The schematic diagram of the analysis method used for the current work is given in **Figure 36**. The obtained results by using this technique are provided in **section 5.2**.

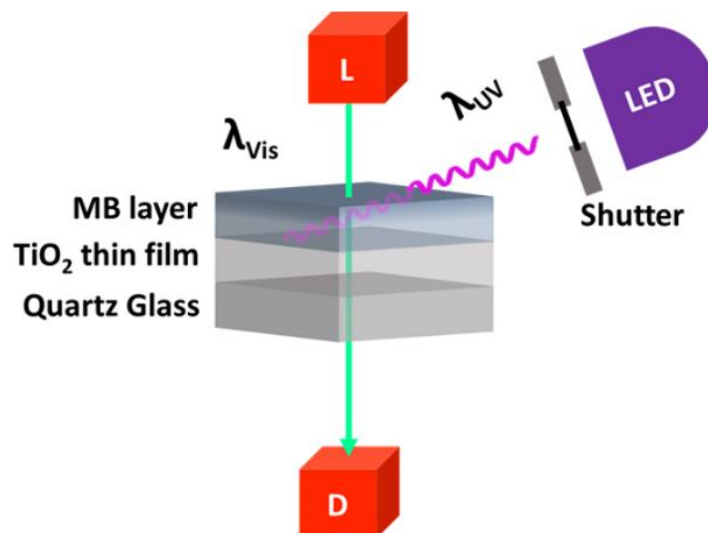


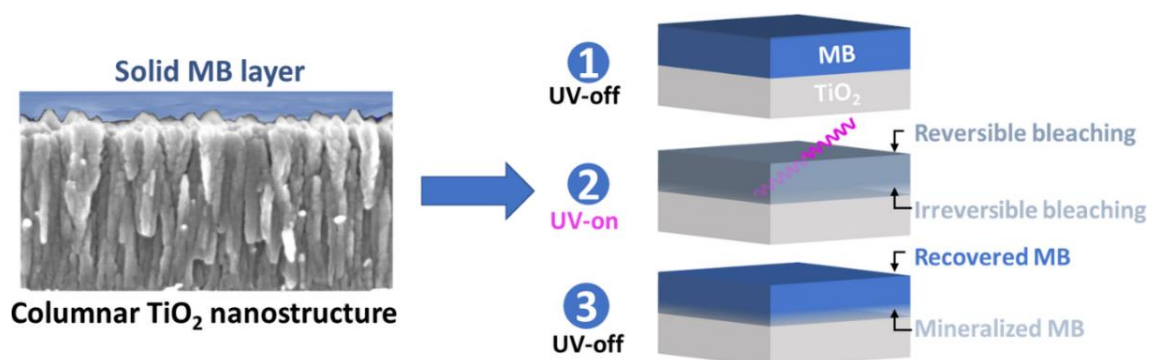
**Figure 36** Schematic representation of analysis method used for determining photocatalytic performance of TiO<sub>2</sub> thin films by observing bleaching of MB in-air.

#### 4.4.2.3. Electrochemical Simulation

Electrochemical simulation was performed (in cooperation with University of Southern Denmark) to determine the growth mechanism of the Au structures (developed on TiO<sub>2</sub> thin films) obtained by photocatalytic reduction process. Electrostatic field calculations based on the finite-element method (FEM) were performed using the commercially available FEM software COMSOL Multiphysics. A constant voltage (1 V) between a top and a bottom electrode (the latter carrying the Au nanostructure) in a capacitor arrangement filled with the aqueous solution was applied. Without the nanostructure, this leads to a homogeneous electric field, used as a reference for normalizing the local electrical field concentration (LEFC) values ( $E_0 = 1.33 \times 10^6$  V/m for a capacitor with a thickness of 300 nm). Based on this, for a better comparability, we calculated the resulting nanostructure-induced electrical field enhancement as the (unit-less) ratio  $|E/E_0|$ . See **Figure 65** for a more detailed numerical analysis on the influence of aspect ratio and needle tip radius on the local electrical field enhancement.

# Chapter 5. A comparative study of photocatalysis on highly active columnar TiO<sub>2</sub> nanostructures in-air and in-solution

In this chapter, the abstract, results and discussion as well as conclusion of the first research paper are presented. This includes, characterization of TiO<sub>2</sub> thin films (developed by sputtering and spin coating) via SEM and Raman analysis. Further, the photocatalytic activity of the prepared films was evaluated and compared by using two different analytical approaches (to compare the photocatalytic properties in air and in aqueous solution) supported by in-situ UV-Vis spectroscopy and XPS analytical method (refer to *section 4.1* for description of the preparation of thin films).



## 5.1. Abstract

While there is continuous progress in development of new photocatalytic thin films and coatings, the lack of a reliable and standard procedure for measuring the photocatalytic performance of such active surfaces makes it difficult to compare results between research groups and different measurement setups. Here, a comparative study was carried out to demonstrate the high photocatalytic activity of sputter-deposited TiO<sub>2</sub> film with self-organized nanocrack networks by using two different analytical approaches: (i) bleaching of a thin Methylene Blue (MB) solid layer on photocatalytic TiO<sub>2</sub> thin film (in-air) and (ii) the decolorization of a MB aqueous solution in the presence of TiO<sub>2</sub> thin film (in-solution). While the decolorization of aqueous MB solution provides an indirect observation of the photocatalytic effect imposed by the TiO<sub>2</sub> film, the use of a solid MB layer as an indicator allows monitoring of photocatalytic reactions at the solid-air interface directly. We showed the applicability of this approach as a complementary and a fast analysis method to reveal the photocatalytic efficiency of thin films by comparing it with the state-of-the-art inks (based on MB and other similar organic dyes) used as photocatalysis indicator.

## 5.2. Results and Discussion

### 5.2.1. TiO<sub>2</sub> Thin Film

High aspect ratio (AR) columnar structures of sputter-deposited film shown in **Figure 37** revealed by cross-sectional SEM (inset in **Figure 37**) remind of a typical morphology (transition zone and zone 2) proposed by the structure zone model (SZM) for sputter-deposited thin films [95]. In addition, we observed a network of deep trenches (nanocracks) between these high AR columnar structures, oriented perpendicular to the substrate. Recently, we have shown that sputtering at high oxygen partial pressures and low deposition rates leads to the formation of such high AR structures with weak inter-columnar bonding [96]. During the heat treatment, oxygen saturated bonds seem to act as a barrier between individual columnar structures, and this hinders their coalescence. Crystallization during heat treatment leads to the densification of the columnar structures which resulted in a significant shrinkage. Additionally, these dense columns seem to be subjected to a preferential shrinkage along their flanks to minimize the compressive stress occurring at the heating step due to the difference in thermal expansion coefficients (quartz=5.0x10<sup>-7</sup> 1/K and Si=8.6x10<sup>-6</sup> 1/K). This difference in thermal expansion coefficients also induces a tensile stress in TiO<sub>2</sub> thin film (which contracts to a higher extent than the quartz substrate) upon cooling. The absence of a strong bonding between individual columns promotes a

preferential cracking during heating and air quenching cycle (compression-tension cycle) and consequently a network of nanoscopic cracks forms.

The reference TiO<sub>2</sub> film, prepared by spin-coating, had a porous structure composed of spherical TiO<sub>2</sub> nanoparticles, which were well distributed and maintained their original size (25-30 nm) and shape (*Figure 38*).

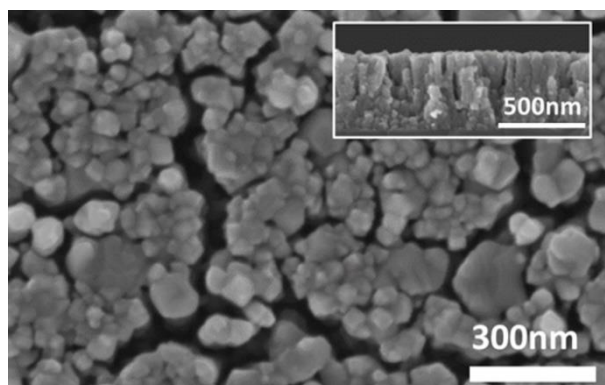


*Figure 37* SEM images of sputter-deposited TiO<sub>2</sub> film after the heat treatment (HT) inset show cross-sectional SEM micrographs.

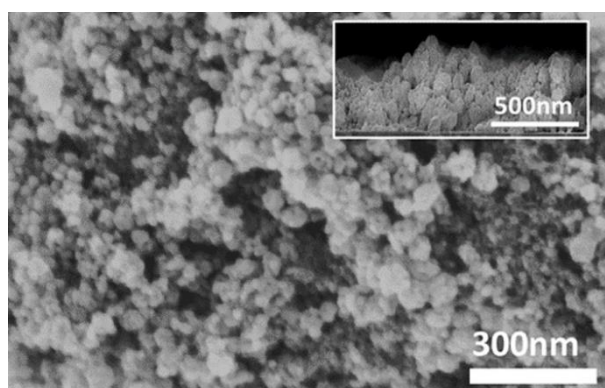


*Figure 38* SEM images of spin-coated reference TiO<sub>2</sub> film and inset show cross-sectional SEM micrographs.

A special attention was given to keep thicknesses of both (sputter-deposited and the reference) thin films about 400-450 nm for a reliable comparison. It is reported that commercial TiO<sub>2</sub> nanoparticles, which were spin-coated, consist of anatase crystallites [97]. Our analysis (*Figure 39*) for sputter-deposited and reference TiO<sub>2</sub> thin films showed consistent results as bands observed at 143 cm<sup>-1</sup>, 395 cm<sup>-1</sup>, 517 cm<sup>-1</sup> and 637 cm<sup>-1</sup> correspond to anatase phase [98].

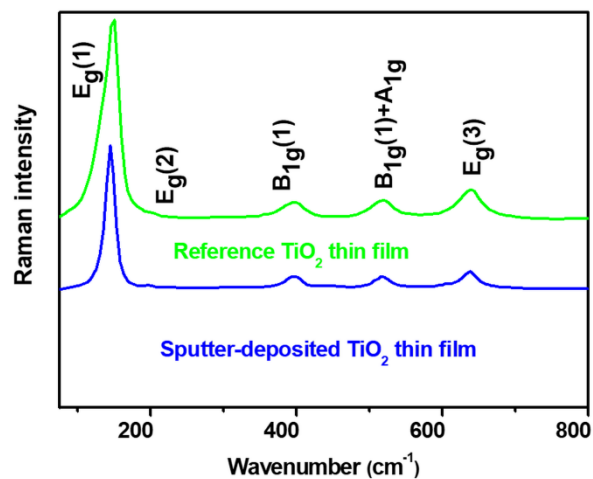


**Figure 39** Raman spectra of prepared TiO<sub>2</sub> thin films.

### 5.2.2. Photocatalytic Degradation of MB in-Air (Dry condition)

Photocatalytic activity of sputter-deposited and reference TiO<sub>2</sub> thin films were analyzed by using solid MB layer as test pollutant. First, we monitored the decolorization of the solid MB layer deposited on sputter-deposited TiO<sub>2</sub> to get a better understanding of the photocatalytic bleaching taking place in air, which is important to reveal the performance of outdoor applications of photocatalytic TiO<sub>2</sub> thin films.

MB layer (60-80 nm) deposited on TiO<sub>2</sub> sample was exposed to UV light and in-situ UV-vis spectroscopy analysis was conducted to reveal the change in the absorption at 580 nm. It is well known that MB exhibits an absorption maximum at 664 nm (absorption band corresponding to  $n-\pi^*$  transitions, where  $n$  is the free doublet on the nitrogen atom of C=N bond and free doublet of S atom on S=C bond) of MB solution by the UV exposure time [99]. On the other hand, we observed the shift of the absorption maxima to 580 nm for MB solid layer. Similarly, Honda et al. reported such a shift of the absorption maxima [50] which can be attributed to dimer aggregates as shown by Ishizaki et al. [100].

The transmission increased directly after the UV exposure and the absorption was recovered partially after blocking the UV light source (after 60 sec. exposure) as shown in **Figure 40a**. While the recovery in the absorption of the MB layer can be attributed to the reversible bleaching by the  $MB \rightleftharpoons LMB$  conversion (as schematically explained in **Figure 40b**), the difference in the initial and final absorptions can be explained by simultaneously occurring irreversible bleaching (mineralization). Honda et al. reported such a recovery in the color of the solid MB layer deposited on a photocatalytic thin film just after stopping the UV irradiation, but authors did not quantify the change in the absorption and moreover,



they did not comment on the underlying mechanism at all [23]. When we prolonged the UV exposure time (longer than 5 min.) we did not observe any recovery in the absorption (*Figure 40c*) which indicates fully bleaching of the MB layer by the irreversible mineralization as schematically depicted in *Figure 40d*.

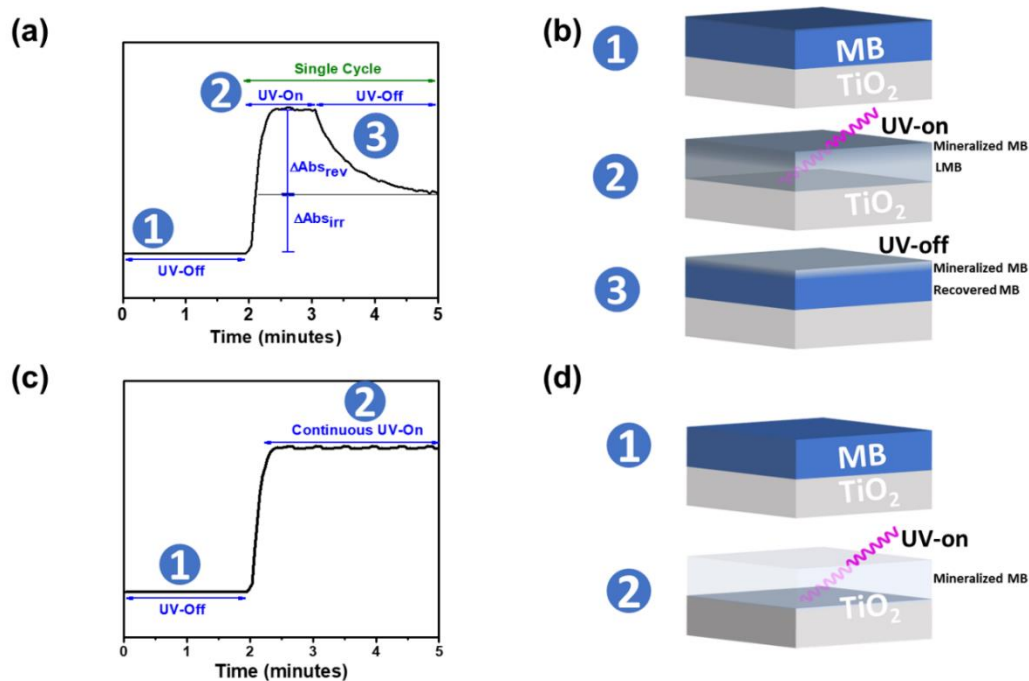


**Figure 40** (a) Transmission spectrum (at 580 nm) recorded during a UV-on-off single cycle and (b) Schematic presentation of photocatalytic reaction steps within a UV-on-off single cycle, Step 1: UV light is off and no bleaching takes place, Step 2: UV lights on and it induces both reversible (light blue layer) and irreversible bleaching (dark blue), Step 3: UV light is off and reversible bleaching is over after 2 min. of light off (color of the light blue layer is recovered) but the irreversible bleaching leads to the decolorization (top layer). (c) Transmission spectrum (at 580 nm) recorded during continuous UV-on (no recovery of MB was noticed) (d) Schematic presentation of reaction steps within continuous UV on (Step 1: UV light is off, and no bleaching takes place and Step 2: UV light is continuously on and it reveals irreversible bleaching (light blue))

To get insights of the reversible and irreversible photocatalytic bleaching of MB layer deposited on TiO<sub>2</sub>, we monitored the change in the absorption (in-situ transmission spectroscopy) during short UV-on-off cycles (60 sec. on / 120 sec. off). After exposing the MB deposited TiO<sub>2</sub> sample to UV light, the transmission increased slightly (*Figure 41a*). When the UV light source was switched off the transmission went down gradually and the same was observed in following UV-on-off cycles. After five UV-on-off cycles the consecutive increase-decrease behavior in the transmission spectrum became less distinguishable. When we compared the transmission spectrum of the MB layer deposited on the control substrate (non-active quartz glass), we observed no change upon the UV exposure (*Figure 41b*). This clearly showed that the change in the absorption might not be attributed to UV induced photobleaching of MB. Some studies reported that bleaching of

MB takes place in oxygen-rich aqueous solution upon UV irradiation (300-400 nm) in the absence of any photocatalyst [101].

We tabulated the change in transmission ( $\Delta T$ ) after every UV-on-off cycle by calculating the difference in the transmission before and after the UV exposure as shown in **Figure 41c**.  $\Delta T$  gradually decreases after each UV-on-off cycle and this may be explained by the irreversible reaction (mineralization) of MB gradually after every irradiation cycle. In addition, the active oxygen adsorbed in MB layer (as residual water content) and at MB/TiO<sub>2</sub> interface (functional surface groups as -OH, etc.) might be diminishing at repeating irreversible reaction cycles and this might also slow down overall decomposition reaction. Based on the cumulative change in the transmission after every UV-on-off cycle, we correlated the percentage of reversible and irreversible photobleaching with their corresponding contributions to  $\Delta T$  (as shown in **Figure 41d**). This empirical correlation shows that at the beginning the reversible bleaching was dominant, but afterwards we have observed a nearly constant ratio between reversible and irreversible bleaching (70% reversible bleaching and 30% irreversible bleaching). While the exact quantification of such a ratio is not trivial, it is clear that the contribution of reversible reaction to the bleaching was higher than that of irreversible reaction at every cycle. This may be explained by the fast reduction of MB to LMB in comparison to the indirect and relatively slower mineralization of MB by TiO<sub>2</sub>. In such a typical mineralization reaction, first, photogenerated electrons are trapped by the oxygen and hydroxyl groups (-OH), then these reactive species decompose MB into ionic by-products. In comparison MB $\rightleftharpoons$ LMB conversion takes place by the direct electron transfer from TiO<sub>2</sub> [35,91].

The change of the absorption after every short UV-on-off cycle clearly shows that the irreversible mineralization is not completed yet. When the MB layer is not fully mineralized upon UV exposure, the color (absorption) recovery can be observed due to possible MB $\rightleftharpoons$ LMB conversion. Mills et al. presented that re-oxidation of the LMB to MB is extremely fast and this leads to the fast re-colorization [101]. They suggested using an additional sacrificial electron donor (SED) to block such a reversible reaction. On the other hand, if the UV exposure time is sufficient for the full mineralization of the MB layer, there will be no need for a SED to block the color recovery [102].

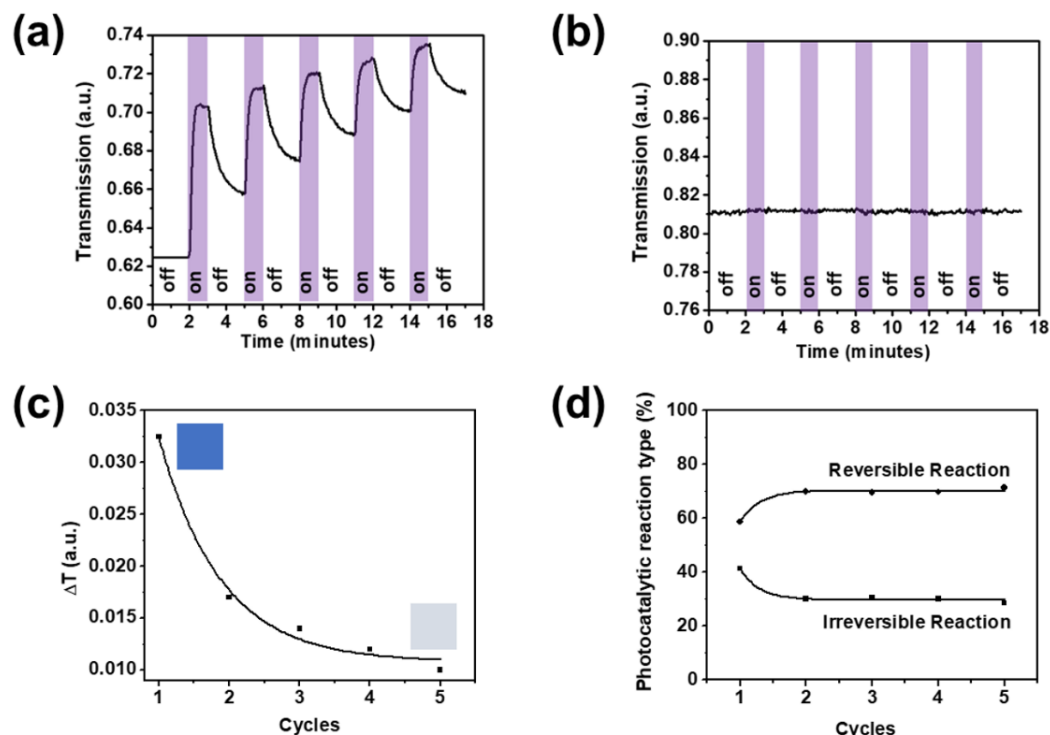


**Figure 41** Transmission spectra of thin MB layer (a) on photoactive TiO<sub>2</sub> layer and (b) on quartz glass (control substrate) after UV-on-off cycles. (c) Cumulative change in the transmission of MB layer after UV on-off cycles (insets indicate the initial and final color of MB/TiO<sub>2</sub> bi-layer) (d) Quantification (%) of reversible and irreversible bleaching (% of irreversible bleaching vs. % of reversible bleaching).

We carried out a systematic study to reveal the effect of the UV exposure (continuous) time on the MB mineralization. We prepared identical MB layers in terms of thickness (60–80 nm) and exposed them to UV light for different time intervals (1–8 min.). Before and after UV exposure the transmission of MB deposited TiO<sub>2</sub> samples was recorded by UV-vis spectroscopy. We observed a gradual increase in the transmission by the exposure time (**Figure 42a** shows normalized transmission in terms of percentages, %). It is clearly seen that at longer exposure time the absorption reached to a maximum value and stayed constant regardless from further exposing the sample to UV light. This indicates, the MB layer was totally mineralized at longer UV exposure time.

UV exposure time needed for a full mineralization depends on the amount of deposited MB layer. The control of the solid MB layer amount is one of the critical parameters to get reliable results. The significant difference in the decolorization time of MB (loaded on photocatalytic thin films) measured by Mills et al. and Ollis et al might be attributed to the uncertainty of the loaded MB amount [102–104]. We prepared MB layers with different thicknesses (**Figure 42b**) and compared their transmission after exposing to UV light for 8 min (**Figure 42c-d** show SEM micrographs before and after UV exposure, respectively). It is clearly seen graphically in **Figure 42b** that the increase in the

transmission was almost negligible when the layer thickness exceeded 250 nm. While 100-130 nm thick MB layer was almost totally bleached after 8 min UV exposure and we did not observe any color change in case of thicker MB layers (250 nm). Thickness of 60-80 nm and above 250 nm MB layers on TiO<sub>2</sub> films is analyzed by SEM as depicted in *Figure 43a-b*.

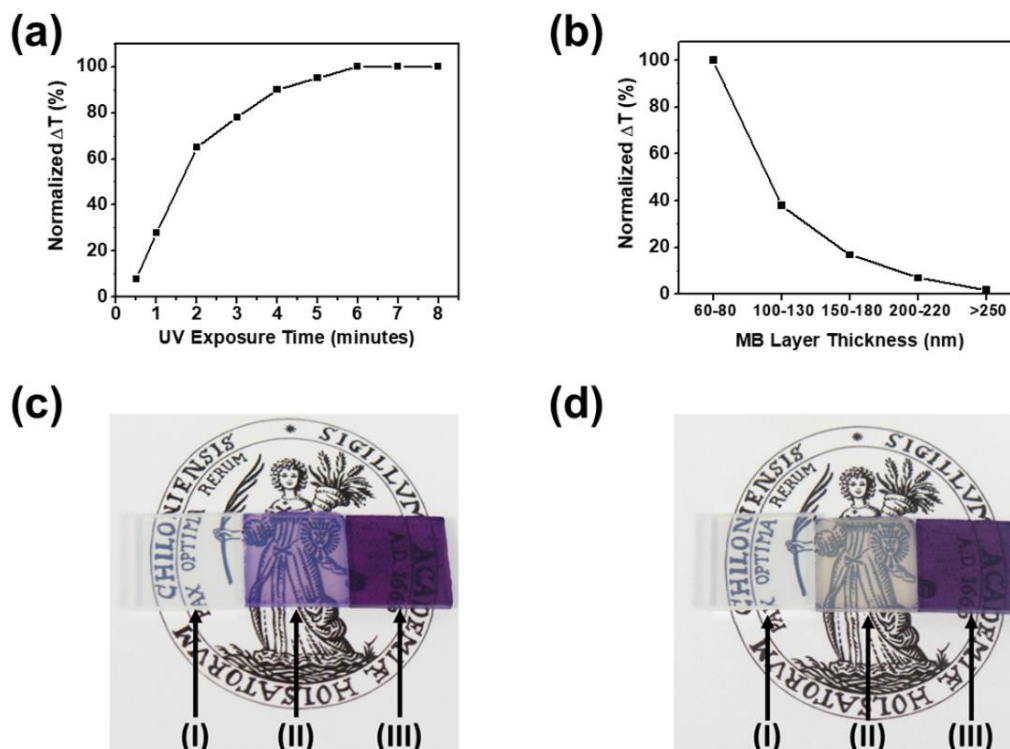


**Figure 42** (a) Transmission of 60-80 nm thick MB layer after different UV exposure time intervals, (b) Transmission of MB layers with different thicknesses (60-250 nm) for a fixed time interval (8 min.), Photographs of (I) uncoated, (II) 100 nm MB coated and (III) 250 nm coated MB samples (c) before UV exposure and (d) after UV exposure.

In case of using a solid MB layer as the test pollutant, the number of oxygen-containing groups adsorbed on the TiO<sub>2</sub> surface should be very critical in comparison to using an aqueous test environment where an excess amount of dissolved oxygen species is present. O<sub>2</sub> captured from the air and -OH adsorption from the moisture may enhance the photobleaching. We carried out all experiments under the identical conditions (the humidity and the temperature were kept about 55 % and 24 °C, respectively) to achieve comparable results. Therefore, it is believed that the limited active oxygen-content on TiO<sub>2</sub> surface seems to be insufficient for the photocatalytic bleaching of thicker MB layers completely.

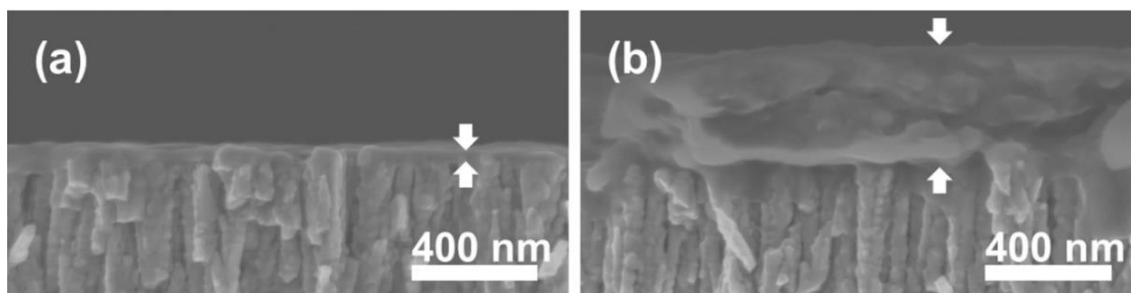


**Figure 43** Thickness analysis of MB dry film by cross-sectional SEM: (a) 60-80 nm thick MB layer (b) >250 nm thick MB layer.

We used X-ray photoelectron spectroscopy (XPS) to reveal the effect of the surface oxygen content on the photocatalytic bleaching of MB layer on sputter-deposited TiO<sub>2</sub> film. 60-80 nm thick MB layer deposited TiO<sub>2</sub> sample was illuminated by an UV LED (4.50 mW/cm<sup>2</sup>) for 8 min. **Figure 44** shows a high-resolution O1s XPS spectrum of the TiO<sub>2</sub> film before and after the UV exposure in-air. Recorded spectra were composed of three peaks (529.5 eV, 531 eV and 532 eV) which correspond to three oxygen states: lattice oxygen (Ti–O), chemisorbed oxygen (Ti–O=O or C=O species, and hydroxyl radical (Ti–OH) or C–O species [105]. The number of oxygen-containing groups has been changed after UV exposure; while lattice oxygen and adsorbed oxygen decreased slightly, and the amount of hydroxyl groups increased (numerical values are given in **Figure 44**). The decrease of the adsorbed oxygen content may be attributed to the desorption of oxygen-containing groups in the form of CO<sub>2</sub> upon the photocatalytic reaction. Such a photocatalytic reaction is basically triggered by superoxide anion (O<sub>2</sub><sup>•-</sup>) formation after exposing TiO<sub>2</sub> to UV light in oxygen atmosphere [106]. Total decolorization of the deposited MB solid layer (**Figure 42c-d**) is consistent with XPS analysis and both clearly confirm an efficient photocatalytic reaction.

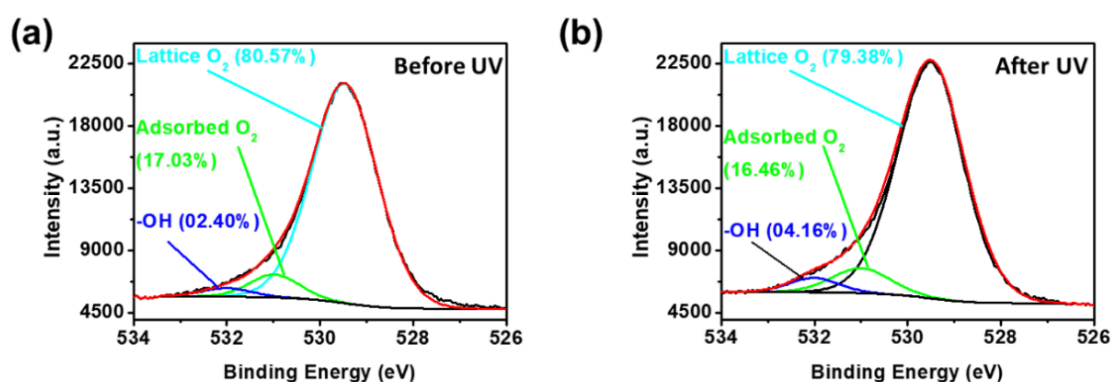


**Figure 44** High resolution O1s XPS spectra from sputter-deposited TiO<sub>2</sub> thin film coated with a 60-80 nm thick MB solid layer (a) before and (b) after UV exposure for 8 min (Red colored: fitted model and Black colored: recorded data).

Using MB solid layer as a test pollutant leads to fast analysis of photocatalytic thin films, and this method also allows testing performance of photocatalytic materials on-site without any need for sophisticated and expensive analytical tools and as well as idealized laboratory conditions. To get more insights of the photobleaching kinetics we quantified the degradation of 60-80 nm thin MB solid layer deposited on TiO<sub>2</sub> thin film using in-situ UV-vis spectroscopy, as shown schematically in **Figure 45a**. Decolorization of 60-80 nm thick MB layer on sputter-deposited TiO<sub>2</sub> after UV exposure for 8 min is displayed in **Figure 45b**. **Figure 45c-d** show the linear fit and normalized absorbance data, respectively, for the photocatalytic bleaching of a MB layer deposited on sputter-deposited and reference TiO<sub>2</sub> thin film. To achieve 90% bleaching ( $\ln(\text{Abs}/\text{Abs}_0) \approx -2.5$ ), sputter-deposited TiO<sub>2</sub> film takes 4.95 min. versus about 25 min. for reference TiO<sub>2</sub> thin film. Ollis et al. introduced a similar study on the photocatalytic bleaching of a dye layer deposited on immobilized TiO<sub>2</sub> nanoparticles [107]. Although they mentioned that organic dye forms a monolayer on TiO<sub>2</sub> nanoparticles, a closer look at their study reveals that a dynamic reflection analysis (using **Kubelka–Munk method**) was conducted from a huge volume of dye (a test holder full of excessive amount of dye-coated nanoparticles). They reported that the 90 % decolorization of the organic test dye took about 500 min. and this may not be the case for the bleaching of a monolayer. There is an uncertainty in the amount of test dye loaded on TiO<sub>2</sub> nanoparticles (amount per nanoparticle or total amount). Authors used a similar approach to monitor the photocatalytic bleaching of the dye layer on Pilkington Active™ glass and they reported that 90 % dye decolorization took even much longer time (longer than 1000 min.) [107]. The lack of information about the loaded dye volume and the relative amount of rutile and anatase phases in the TiO<sub>2</sub> thin film make it difficult to compare their results with theirs [103] and as well as with ours. On the other hand, the extremely long lasting decolorization of the organic dye, which they observed, may result due to the poor photocatalytic performance of Pilkington Active™ glass. It was reported that this glass contains only a 20 nm thick active TiO<sub>2</sub> layer and such a small amount of active catalyst could be insufficient to decompose thick dye layers [107].

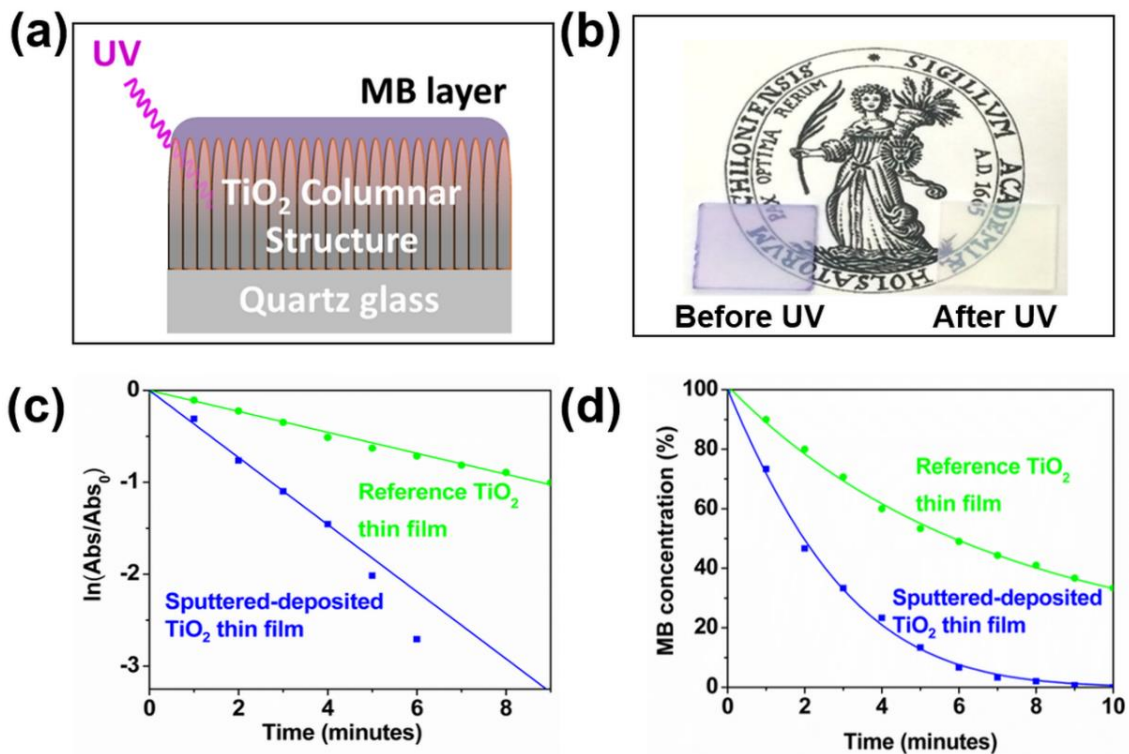


**Figure 45** (a) Schematic presentation of photocatalytic bleaching in-air, (b) Decolorization of 60-80 nm thick MB layer on sputter-deposited TiO<sub>2</sub> after UV exposure for 8 min, (c)  $\ln(\text{normalized absorbance})$  vs time plot and (d) Normalized bleaching (plot) of 60-80 nm thick MB layers on sputter-deposited and reference TiO<sub>2</sub> films.

### 5.2.3. Photocatalytic Degradation of MB in-Aqueous Solution (Wet Condition)

We also compared the photocatalytic activity of the sputter-deposited and the reference TiO<sub>2</sub> films by a conventional analysis method which is based on monitoring the decolorization of the aqueous MB solution (solid-aqueous interface) as depicted schematically in **Figure 46a**. The change in the absorbance was correlated to the MB concentration using the Beer-Lambert Law [108] and decolorization of MB aqueous solution in quartz glass cuvettes at different time laps is shown in **Figure 46b**. The graphs in **Figure 46c-d** show the linear fit and normalized absorbance data, respectively for the photocatalytic bleaching of MB layer deposited on sputter-deposited and reference TiO<sub>2</sub> thin film. The obtained result in **Figure 46c** clearly indicates a first-order rate model for the bleaching of the MB solution. After an hour of UV exposure, sputter-deposited TiO<sub>2</sub> film showed a photocatalytic efficiency of 29.5 %, whereas the efficiency of the reference thin film was only 12 %.

The total photocatalytic bleaching of MB test solution (by sputter-deposited TiO<sub>2</sub> thin film) lasted longer than 8 hours. In literature, much faster degradation rates have been shown, but most of these studies cover the use of suspended TiO<sub>2</sub> nanoparticles rather than



thin films. There are only a few studies which demonstrated full bleaching of MB solution by TiO<sub>2</sub> thin films at shorter time intervals in comparison to our findings [109]. On the other hand, one can see significant differences between our and these analytic studies (TiO<sub>2</sub> polymorph type, size of the substrate, wavelength of the light source, intensity of the light, temperature of dye solution, stirring speed and concentration of the dye solution) therefore, it is difficult to compare them properly with each other and as well as with ours [110].

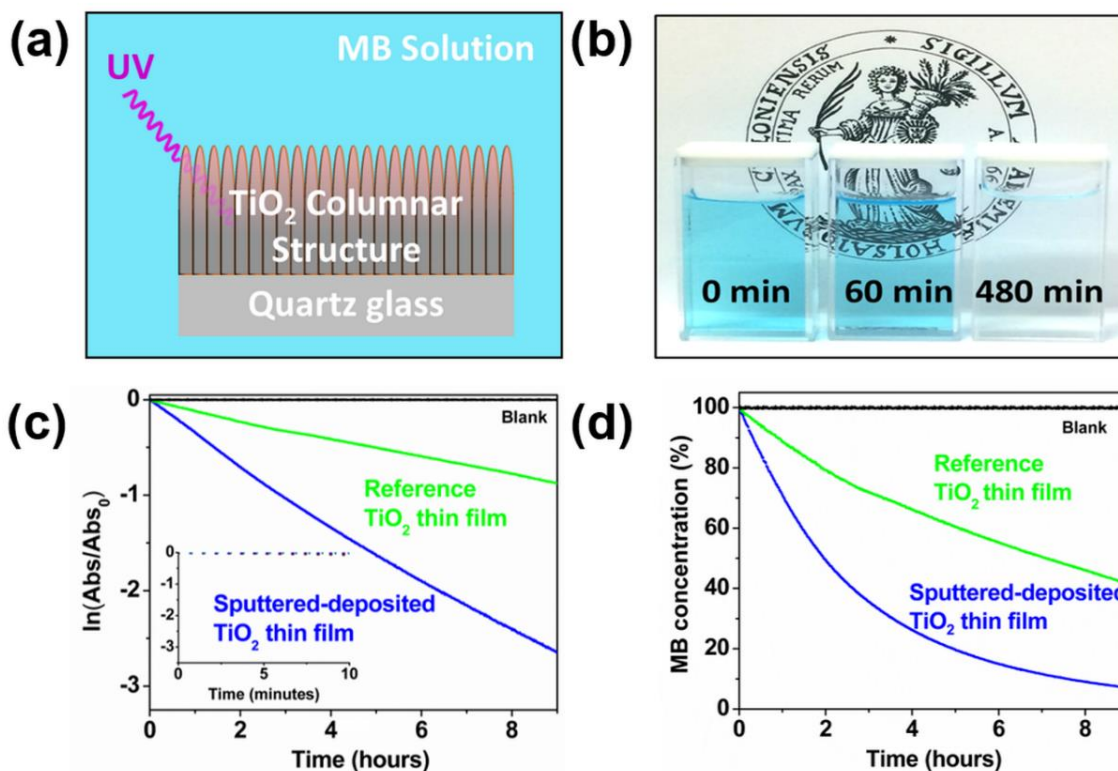


**Figure 46** (a) Schematic presentation of photocatalytic bleaching of MB aqueous solution, (b) Decolorization of MB aqueous solution in quartz glass cuvettes at different time laps (c)  $\ln(\text{normalized absorbance})$  vs time plot and (d) Normalized bleaching (plot) of MB in the solution (long term) sputter-deposited and reference TiO<sub>2</sub> films quartz substrate (given as blank) is used as the control substrate.

By immersing a TiO<sub>2</sub> coated tiny (10 x 10 mm<sup>2</sup>) quartz substrate (active solid volume is estimated about 7.5-8.0x10<sup>-4</sup> ml) into the excessive volume of aqueous MB test solution (6.5 ml) we are bounded to an indirect monitoring of the photocatalytic bleaching. Here, the cumulative bleaching cannot be correlated to instant photocatalytic degradation rates and this restricts the direct monitoring of photocatalytic reactions. Inset in **Figure 46c** shows that it was not possible to distinguish the differences in the photocatalytic bleaching of MB solution, rather it needed several hours to get a reliable comparison of decolorization rates.

The mechanism of MB bleaching in an aqueous environment (in the presence of TiO<sub>2</sub>) is extremely complex. In such an oxygen rich medium, the degradation of MB is mainly attributed to the decomposition of MB (conversion of organic carbon into harmless gaseous



CO<sub>2</sub> and that of nitrogen and sulfur heteroatoms into inorganic ions, such as nitrate and ammonium, and sulfate ions, respectively) by photocatalytic generation of active oxygen species: hydroxyl radical (OH<sup>•</sup>), superoxide anion (O<sub>2</sub><sup>•-</sup>) and hydrogen peroxide (H<sub>2</sub>O<sub>2</sub>) [35]. One should also take it into account that TiO<sub>2</sub> contributes directly to the decolorization by reducing MB and generation of oxygen singlet (<sup>1</sup>O<sub>2</sub>) upon UV exposure [37]. On the other hand, it is difficult to reveal all these reactions individually in an aqueous medium.

We used a standard model to linear fit (**Figure 46c**) by using an asymptote analysis as presented by various research groups [103] and normalized absorption vs. time curve (**Figure 46d**).

#### 5.2.4. Comparison of MB Degradation Analysis in-Air and - Aqueous Solution (Dry vs Wet Conditions)

Rate constants achieved from the decolorization of dry MB layer on sputter-deposited (k<sub>1</sub>) and reference TiO<sub>2</sub> (k<sub>2</sub>) thin films (k<sub>1</sub> (in-air) ≈ 0.365 min<sup>-1</sup> and k<sub>2</sub> (in-air) ≈ 0.114 min<sup>-1</sup>, respectively) are much higher than those calculated from the decolorization of MB aqueous solution (k<sub>1</sub> (in-solution) ≈ 0.00507 min<sup>-1</sup> and k<sub>2</sub> (in-solution) ≈ 0.00163 min<sup>-1</sup> respectively). This significant difference between rate constants calculated in-air and in-solution may be attributed to the direct surface contribution of TiO<sub>2</sub> thin film to the photocatalytic reactions, which is difficult to reveal in an aqueous dye solution (due to the excessive amount of oxygen rich medium and the limited surface area of photocatalytic thin films). Thus, the use of aqueous medium (volumetric analysis) is more relevant to analyze photocatalytic activity of free standing particles rather than thin films which have relatively limited surface area.

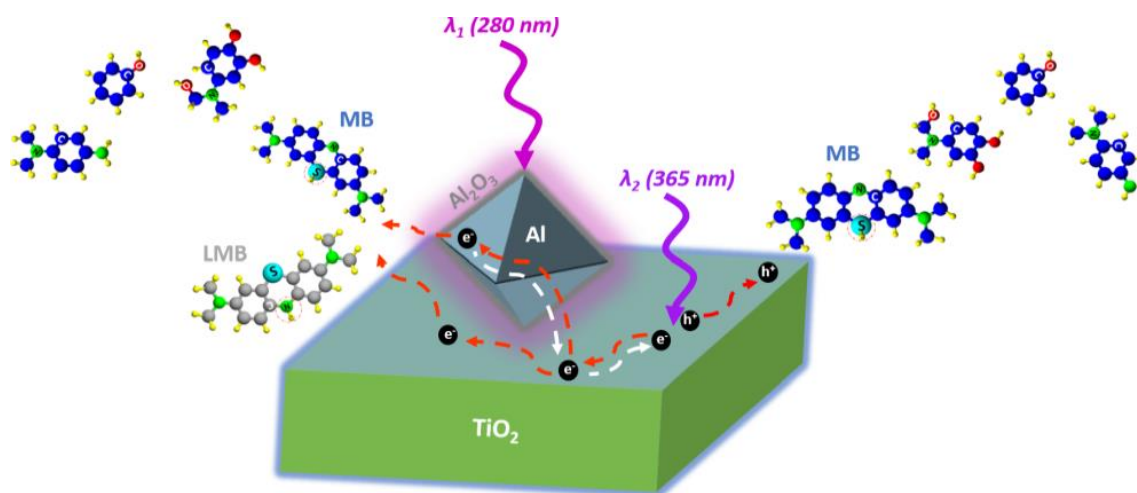
In comparison to reported studies on the degradation of solid dye layers deposited on photocatalytic thin films, our analytic approach has provided reliable results within much shorter time intervals (8-10 min. vs. 500-600 min.). We successfully showed a good correlation between MB bleaching rate constants measured in-air and in-solution as (k<sub>1</sub> (in-air) / k<sub>1</sub> (in-solution) ≈ k<sub>2</sub> (in-air) / k<sub>2</sub> (in-solution)). Therefore, MB bleaching in-air can be used as a fast and reliable method for a comparative study of photocatalytic thin films.

### 5.3. Conclusion

We demonstrated that sputter-deposited TiO<sub>2</sub> film with self-organized nanocrack networks exhibits extremely high photocatalytic efficiency in comparison to a reference TiO<sub>2</sub> thin film composed of immobilized anatase nanoparticles by using two different analytical approaches: (i) bleaching of MB solid layer on photocatalytic TiO<sub>2</sub> thin film (in-air) and (ii) the decolorization of MB aqueous solution in the presence of TiO<sub>2</sub> thin film (in-solution). The significance of both, reversible (MB $\rightleftharpoons$ LMB conversion) and irreversible reactions (mineralization) on the photocatalytic bleaching of MB has been shown successfully. We correlated the photocatalytic bleaching of MB solid layer and the decolorization of aqueous MB. The analysis based on the decolorization of aqueous MB solution provides an indirect observation of the photocatalytic effect imposed by the TiO<sub>2</sub> film, since it monitors basically the indirect decomposition of MB by active oxygen species generated by the photocatalysis. In comparison, using a solid MB layer deposited on TiO<sub>2</sub> film as an indicator allows monitoring of photocatalytic reactions at solid-air interface directly. This can be applied as a complementary and a fast analysis method to reveal the photocatalytic efficiency of thin films. The method may act as a more reliable test model to study the performance of photocatalytic thin films and coatings used for outdoor applications such as self-cleaning windows, building exteriors and paints.

# Chapter 6. The Role of UV Plasmonics on Photocatalytic Performance of TiO<sub>2</sub> Decorated with Al Nanoparticles

In this chapter, the abstract, results and discussion as well as conclusion of the second research paper are presented. This includes synthesis and influence of different parameters on Al nanoclusters stability and their coverage on substrate by using SEM analysis and QCM system, respectively. Afterwards, the crystallinity and structural properties of prepared Al clusters were analyzed by TEM, XPS and UV-vis spectroscopy. Finally, the photocatalytic activity of prepared Al/TiO<sub>2</sub> hybrid layers was observed by new developed analytical method (described in *section 5.2.2*). Preparation method of TiO<sub>2</sub> thin films and Al nanocluster is already described in *sections 4.1* and *4.2*, respectively.



## 6.1. Abstract

We present a facile method, combining sputtering and gas aggregation techniques, to prepare a photocatalytic TiO<sub>2</sub> thin film decorated with stable Al plasmonic nanoparticles (NPs) to reveal the localized surface plasmon resonance (LSPR) effect on TiO<sub>2</sub> photocatalysis under UV irradiation. We demonstrate for the first time the negative and positive influences of LSPR on UV photocatalysis by irradiating Al NPs/TiO<sub>2</sub> hybrid structures at two different UV wavelengths: both at and above the plasmonic absorption of Al NPs.

## 6.2. Results and Discussion

Highly photocatalytic TiO<sub>2</sub> layers decorated with stable and well-defined (shape- and size-controlled) Al NPs were synthesized. Following the sputter deposition of TiO<sub>2</sub> thin film, a GAS technique [73,111,112] was used to decorate underlying TiO<sub>2</sub> film with Al NPs.

### 6.2.1. Controlling Deposition, Size, Morphology and Distribution of Al NPs

Magnetron sputtering combined with gas aggregation chamber, introduced by Haberland et al. [93] (customized GAS chamber as shown in **Figure 47**) [73,113] was used to decorate Al NPs. In addition to argon (Ar) (process gas) we introduced extremely low amount of oxygen (O<sub>2</sub>) (reactive gas) during the sputtering of Al NPs. While the Ar flow rate was kept constant at 0.700 SCCM, the O<sub>2</sub> flow was varied between 0.001 SCCM and 0.400 SCCM to achieve stable Al clusters.

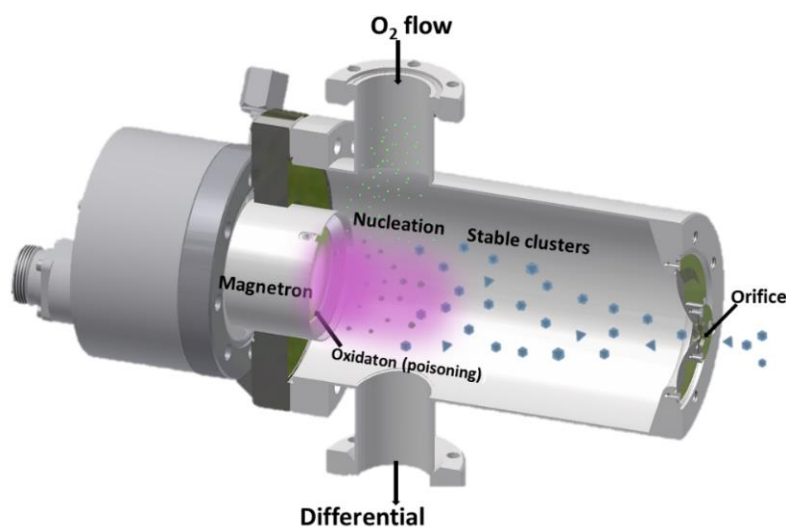


**Figure 47** Schematic presentation of the gas aggregation source (GAS) used to produce the Al NPs.

Below 0.001 SCCM O<sub>2</sub> flow no cluster formation was recorded by the quartz-crystal-microbalance (QCM) system. At 0.001-0.400 SCCM O<sub>2</sub> flow range we were able to produce Al clusters which was confirmed by both, in-situ QCM monitoring (*Figure 48*) and ex-situ SEM analysis (*Figure 49a*, *Figure 50* and *Figure 51*).

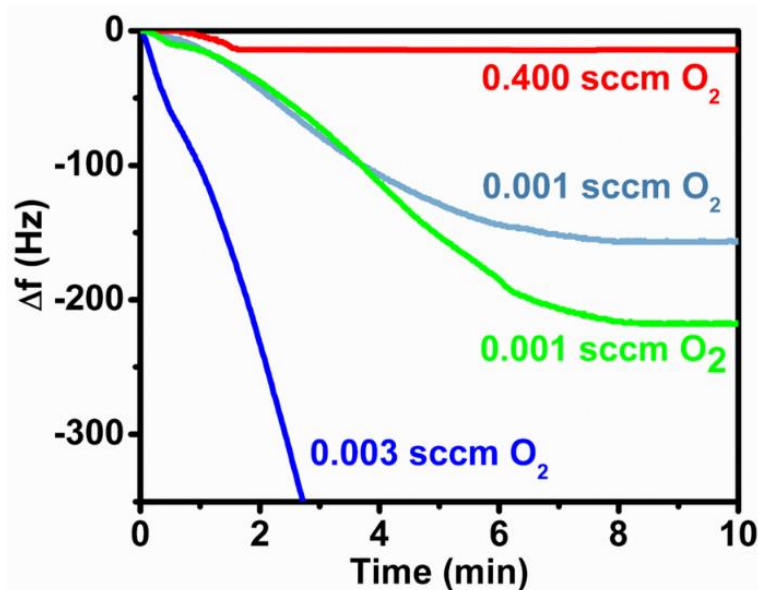


**Figure 48** In-situ analysis of Al NPs deposition rate by monitoring the change in the resonance frequency of quartz crystal microbalance (QCM) at different oxygen flow.

Adding a certain amount of O<sub>2</sub> seems to promote Al cluster nucleation by binding oxygen to sputtered Al atoms [69,73,114]. In comparison to low dimer binding energy of Al–Al (2.736 eV), Al–O binding is quite stable (5.203 eV) [115]. However, at higher O<sub>2</sub> flow (>0.400 SCCM) we did not observe any cluster formation (*Figure 49a*) which might be attributed to the target poisoning (oxidation). Furthermore, we were able to control the size of Al NPs (*Figure 49b*) and their surface coverage (*Figure 49c*) efficiently within a specific O<sub>2</sub> range by changing magnetron power.

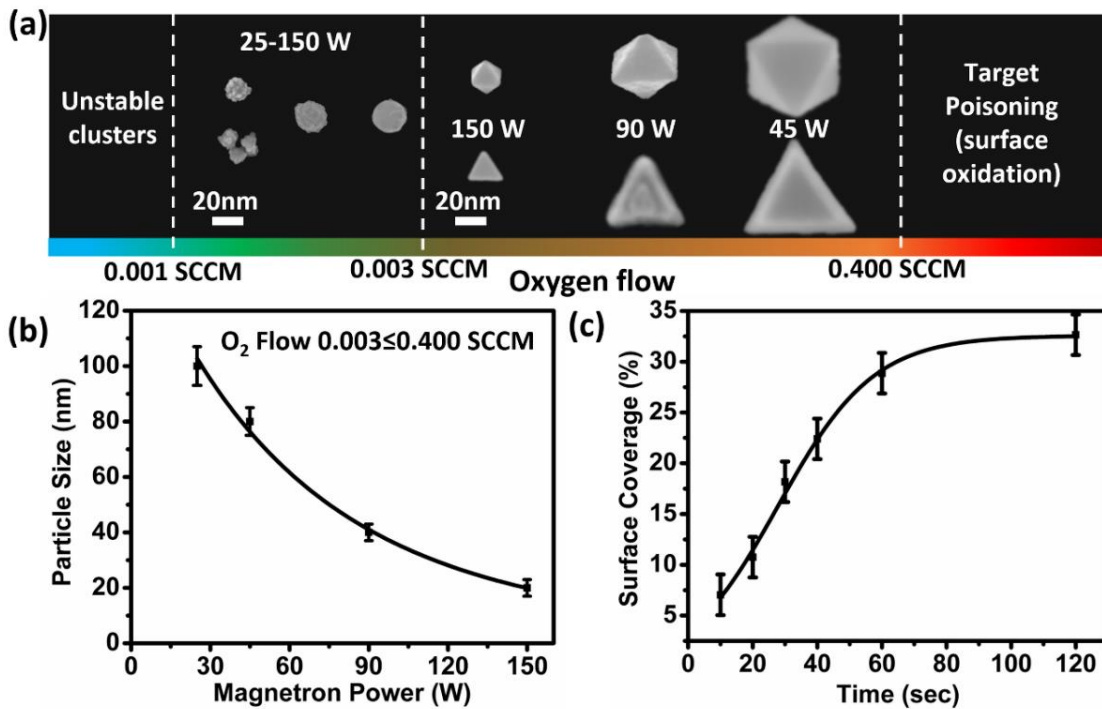


**Figure 49** (a) Schematic representation of the influence of O<sub>2</sub> flow rate on the shape and size of Al NPs (images of single NPs are implemented from SEM images given in **Figure 50** and **Figure 51**), (b) primary particle size of Al NPs as a function of the magnetron power and (c) surface coverage of Al NPs as a function of deposition time (details are provided in **Figure 52**)

The difficulty in maintaining an equilibrium between oxygen induced cluster nucleation and target poisoning has been reported by some researchers [114], but up to our knowledge a systematic study is missing for understanding the effect of the oxygen on the morphology of Al clusters.

Development in the Al NPs crystals is clearly noticed at different O<sub>2</sub> amount in **Figure 50**. At first, amorphous and premature crystals were observed at limited oxygen amount which turned into a semi crystalline structure on increasing oxygen partial pressure. Fine crystallites with defined shape were obtained at O<sub>2</sub> flow rate >0.003 SCCM consisting of octahedron and truncated triangular bipyramid structures.

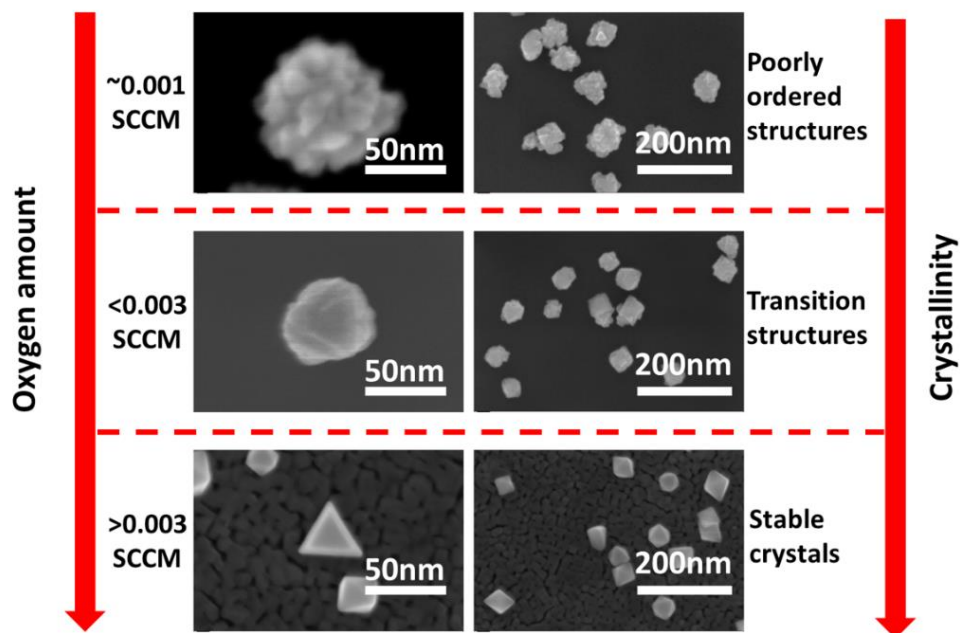


**Figure 50** SEM images of Al NPs at different oxygen flow (oxygen flow vs. crystallinity correlation).

At high magnetron power, small NPs were formed (vice versa) which may be attributed to the high sputter rate of nuclei and their stabilization by oxidation. Such a thin and stable oxide led to the consistency in the particles size and no further aggregation was observed after oxidation. In **Figure 51** we evidently showed three different sized Al NPs synthesized at specific magnetron power (80nm, 40nm and 20nm Al NPs at 45W, 90W and 150W, respectively). Similarly, the coverage of Al NPs was controlled by increasing deposition time at specified magnetron power. The gradual increase in the coverage of 20nm Al NPs was calculated with binary (B/W) SEM images using **ImageJ** program (**Figure 52**).

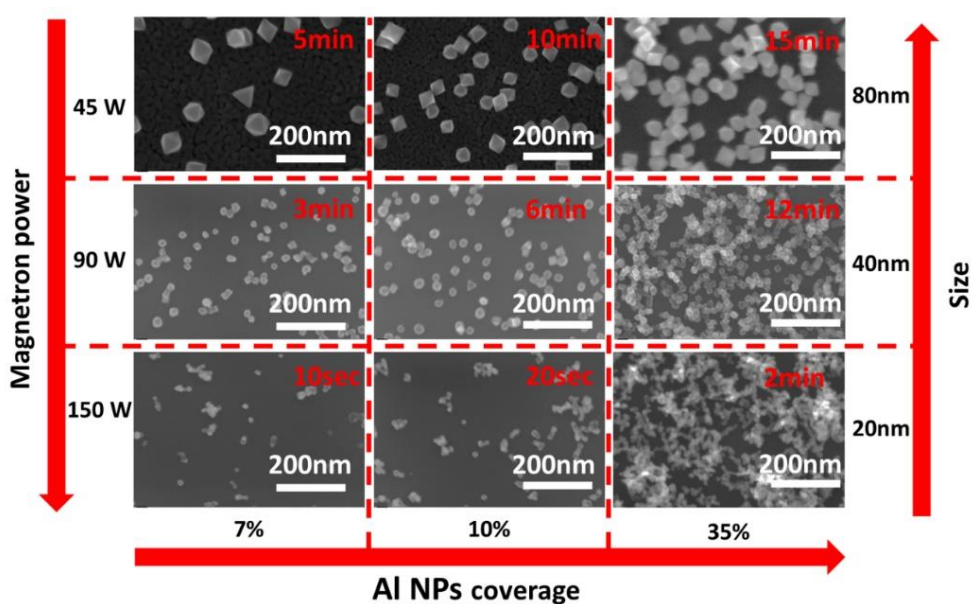


**Figure 51** SEM images of Al NPs prepared at different magnetron power and deposition time (particle size and coverage).



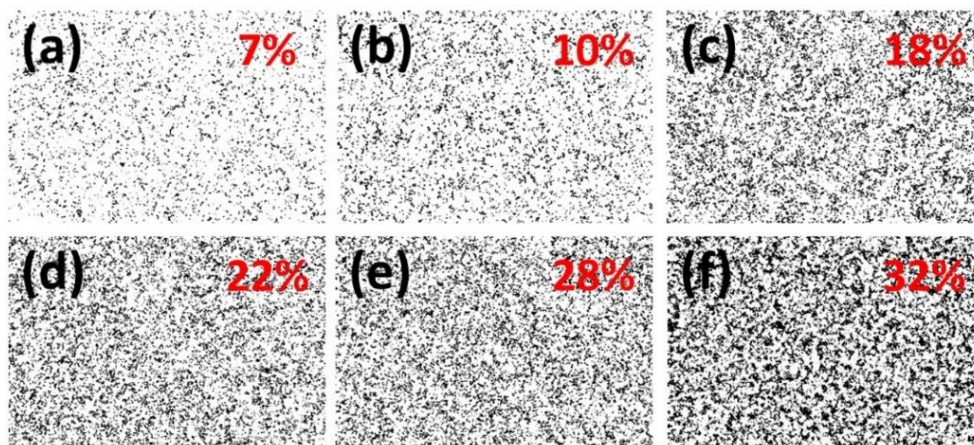


**Figure 52** (a-f). Binary (B/W) SEM images showing the gradual increase in the Al NPs surface coverage at time 10 s, 20 s, 30 s, 40 s, 60 s and 120 s, respectively.

## 6.2.2. Structural and Optical Properties of Al Clusters

In order to perform structural analysis of prepared Al clusters via GAS under (controlled ad-mix oxygen condition), TEM and XPS analysis techniques were applied. TEM analysis showed that majority (> 95 %) of the deposited Al NPs had a projected rhombus shape (**Figure 53a**) and sizes of about  $20 \pm 3$  nm. Further investigation by SEM showed that Al NPs were mostly octahedron (**Figure 51**) and the rest exhibited truncated triangular bi-pyramid structure (seen as projected triangular shape in **Figure 53b**). SAED analysis indicates that (given in **Figure 53c**) rings could be indexed as FCC Al. **Figure 53d** shows the HRTEM image of a single Al NP with octahedral structure exhibiting a metallic core (proven by the lattice fringes) and the surrounding shell of stable oxide about 2 nm thick. This oxide shell protects Al NPs from further oxidation and contamination.

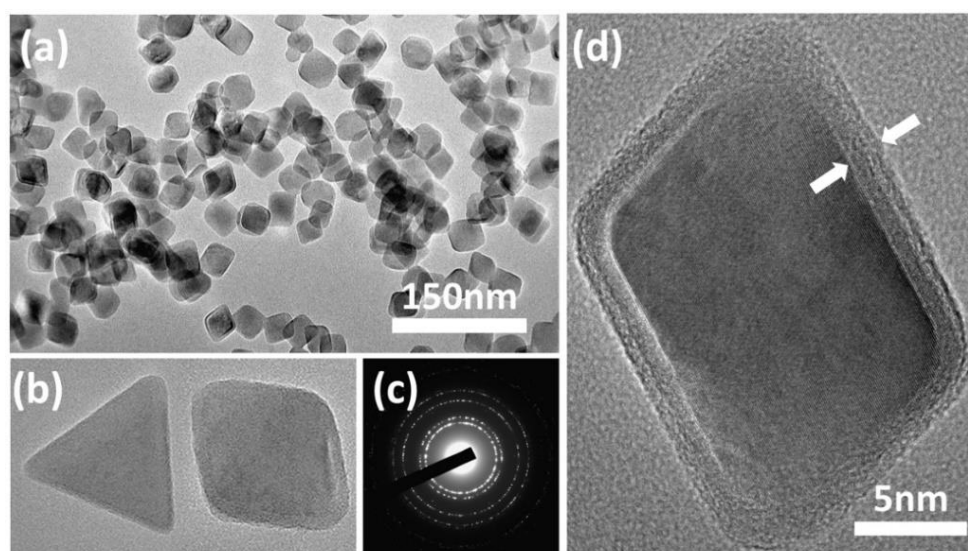


**Figure 53** TEM images of (a) Al NPs, (b) an octahedron and a truncated triangular bi-pyramid Al NPs, (c) SAED analysis is given as inset and (d) HRTEM image of an octahedron Al NP (arrows indicate the stable oxide shell surrounding the Al core)



XPS spectrum shown in **Figure 54** verifies the co-existence of an ultra-thin oxide shell and the metallic Al core observed by TEM [25,115].

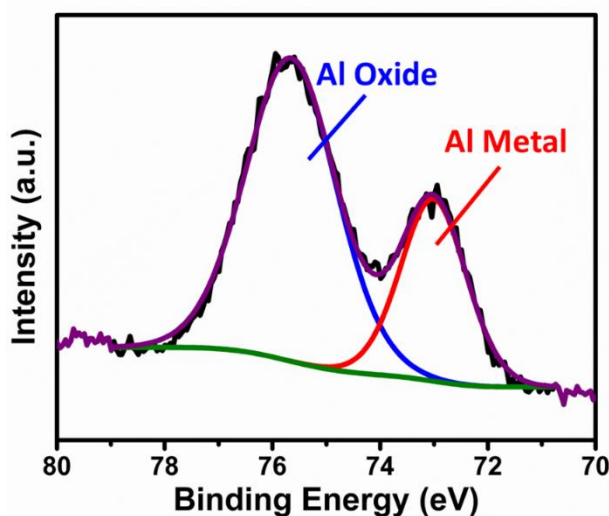


**Figure 54** XPS spectrum of Al NPs

The spectral response of Al NPs deposited on quartz substrates (three different types of surfaces composed of 20 nm, 40 nm and 80 nm Al NPs) was calculated (as shown in detail, **Figure 55**)

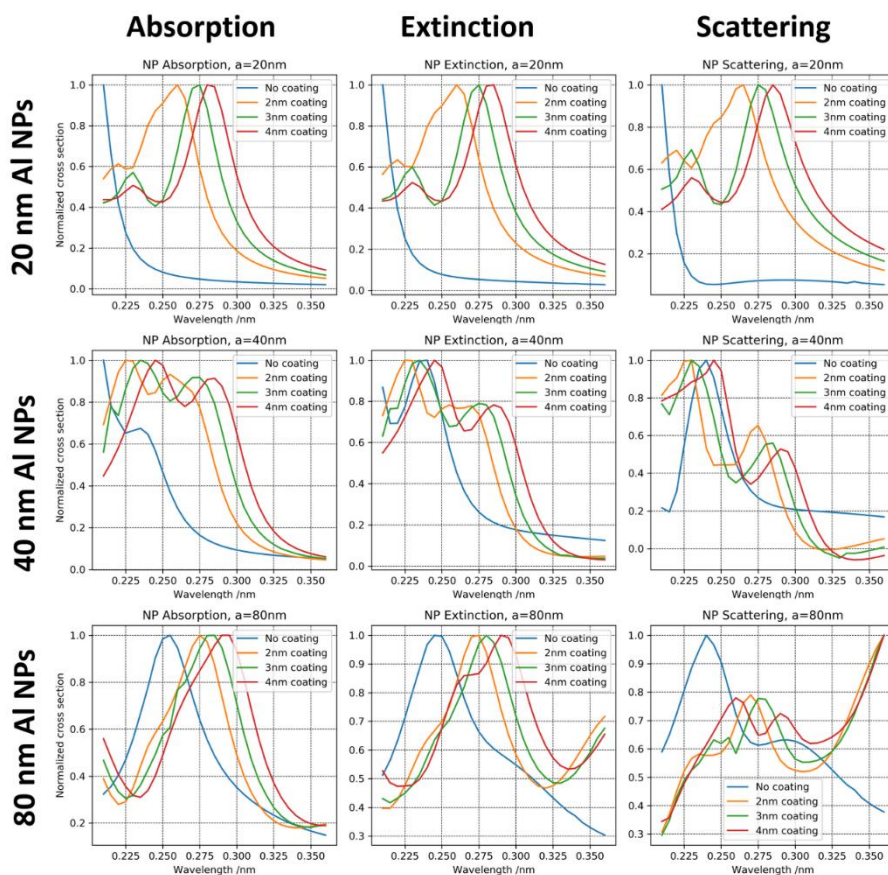


**Figure 55** Simulated absorption, extinction and scattering cross sections of octahedral Al NPs on a SiO<sub>2</sub> surface, with Al<sub>2</sub>O<sub>3</sub> coatings of varying thickness (see Numerical Methods for details).

In order to determine the absorption, extinction and scattering cross sections of octahedral Al NPs on a SiO<sub>2</sub> surface, with Al<sub>2</sub>O<sub>3</sub> coatings of varying thickness (**Figure 55**), simulation was performed (in cooperation with University of Southern Denmark). Since particle scattering and particle plasmonics phenomena are largely governed by the particle scattering, absorption and hence extinction cross section, we modelled these quantities in order to support our experimental findings. To this end, we performed finite-element modelling (FEM) simulations with the commercially available software COMSOL Multiphysics. The NPs on the surface are surrounded by perfectly matched layers (PML) to mimic scattering boundary conditions in all cartesian directions, and a two-port arrangement excites the structure from the top by normally incident, linearly polarized light of various frequencies. By a two-step simulation procedure, we extract the *scattered* electromagnetic field, that is, the electromagnetic field perturbation induced by the Al NP, from the excited total electromagnetic field. With the resulting scattering Poynting vector  $S_{sc}$  we calculate the scattering cross section  $\sigma_{sc}$  by integrating  $S_{sc}$  over the closed particle surface, while the absorption cross section  $\sigma_{abs}$  is given by the (particle-)volume integral over the power loss density. Finally, the extinction cross section  $\sigma_{ext}$  comprises the sum of the preceding ones:  $\sigma_{sc} + \sigma_{abs} = \sigma_{ext}$ . All quantities are usually normalized by the incident light energy.

As clearly seen in the calculated spectra, the presence of a 2 nm surface oxide redshifts the plasmon resonance significantly (**Figure 56a**). While 20 nm Al NPs exhibited a sharp plasmon peak, the increase in the particle size led to redshift and broader absorption spectra (**Figure 56b-d**) [26]. The difference between the calculated and experimental spectra may arise due to particle-particle interactions. For instance, in SEM images (given as insets in **Figure 56b-d**) Al NPs are seen in the form of self-assembled aggregates rather than isolated NPs.

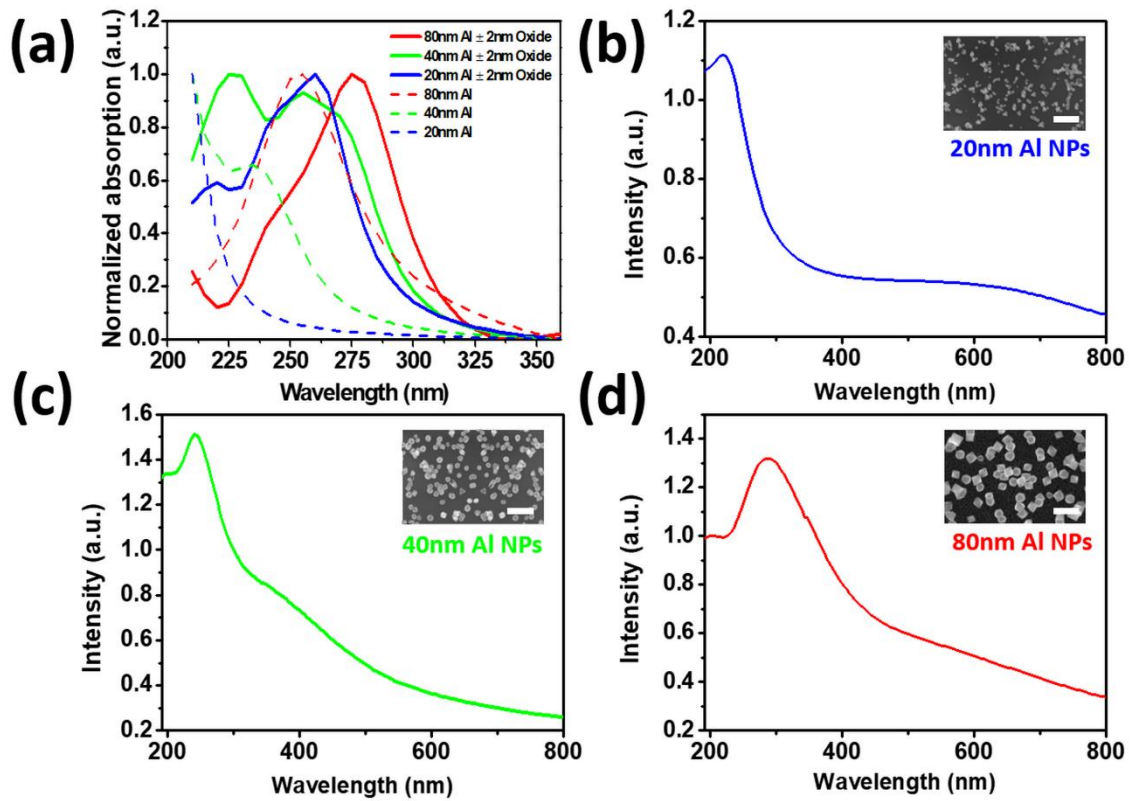


**Figure 56** (a) Simulated (with and without 2 nm oxide cover) and (b-d) experimental absorption spectra of Al NPs with primary sizes of  $20\pm 3$  nm,  $40\pm 3$  nm and  $80\pm 5$  nm, respectively (insets show SEM images of corresponding Al NPs with a scale bar of 200 nm).

### 6.2.3. Photocatalytic Performance of Al/TiO<sub>2</sub> Hybrid Layers

We deposited Al NPs on sputter-deposited TiO<sub>2</sub> films to reveal the NP influence on photocatalysis (while keeping the surface coverage of Al NPs as comparable as possible at 30-35 %, the particle size was systematically altered as presented in **Figure 57**). A diluted aqueous solution of methylene blue (MB) was spin coated on prepared surfaces and the photocatalytic reaction was monitored by the change of the MB absorbance at 580 nm under UV irradiation (using UV LEDs operating at wavelengths of 280 nm and 365 nm) [116]. **Figure 58a-b** show the photocatalytic bleaching of MB on bare and Al NPs decorated TiO<sub>2</sub> layers at two different wavelengths, respectively.

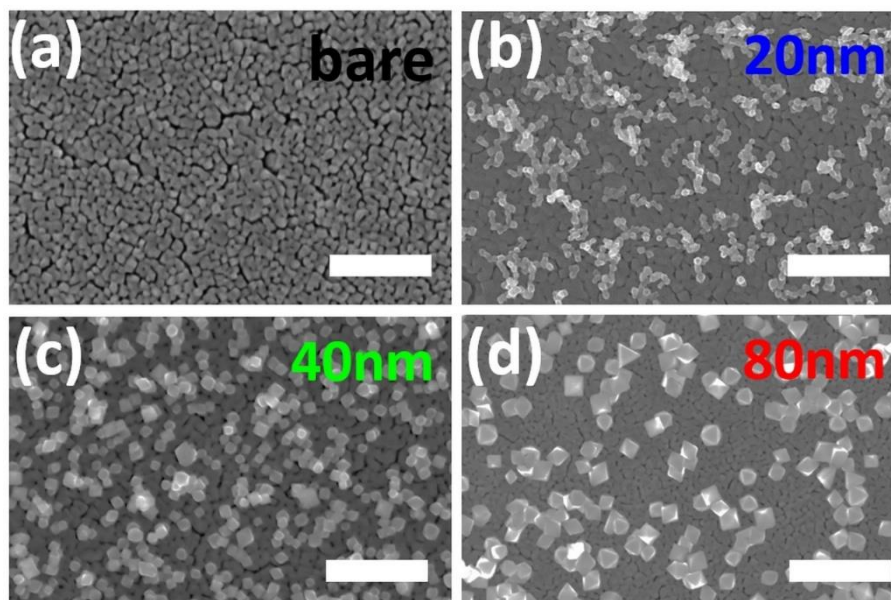


**Figure 57** SEM images of (a) bare TiO<sub>2</sub> and (b-d) Al NPs with primary size of 20 nm, 40 nm and 80 nm decorated TiO<sub>2</sub> films, respectively (scale bar: 300 nm).

Plasmonic Al NPs/TiO<sub>2</sub> hybrid layers exhibited lower photocatalytic activity at 365 nm UV irradiation in comparison to the bare TiO<sub>2</sub> layer (**Figure 58a**). In contrast, the photocatalytic performance of plasmonic Al NPs/TiO<sub>2</sub> hybrid layers significantly increased at 280 nm UV irradiation (**Figure 58b**). A TiO<sub>2</sub> layer decorated with 20 nm Al NPs exhibited the highest photocatalytic activity. Honda et al. similarly demonstrated a significant enhancement of TiO<sub>2</sub> photocatalysis by incorporating Al NPs [117]. On the other hand, they reported a recovery in the MB absorbance after switching off the UV irradiation. We also observed a similar recovery (**Figure 58b**, indicated with the dashed line) and this may be attributed to the conversion of MB to its colorless form leuco-MB (LMB). Recently, we showed a detailed analysis of such a phenomenon <sup>6</sup>, where the decomposition of a 60-80 nm thick MB layer even took several minutes rather than seconds as Honda et al. claimed [50]. Therefore, the sudden change in the MB absorbance (within seconds) cannot be described as photocatalytic bleaching. As shown in **Figure 58c**, the absorption went down drastically within 20 seconds on TiO<sub>2</sub> layer decorated with 20 nm Al NPs (in-situ UV-Vis analysis), which is even much faster than the time interval reported by Honda et al [50]. Thus, to monitor irreversible photocatalytic mineralization of MB, longer irradiation and observation time periods are mandatory.



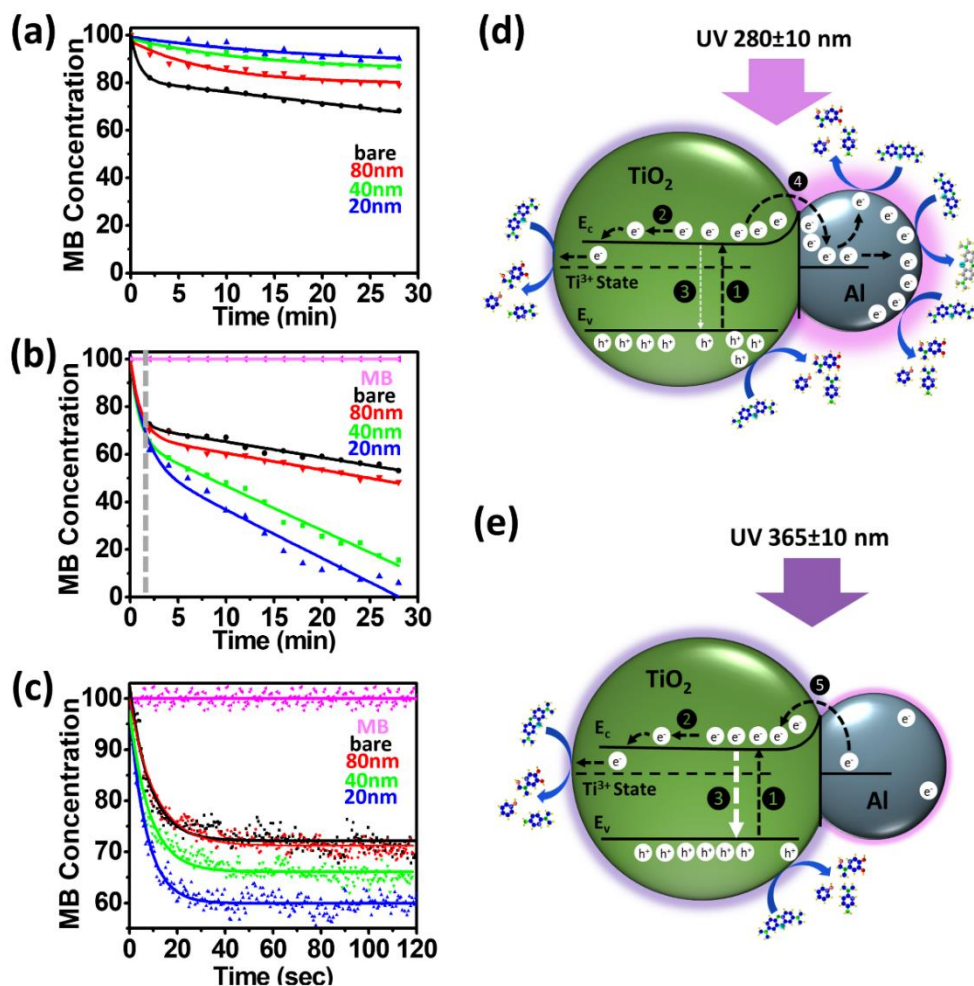


**Figure 58** (a) Photocatalytic bleaching of MB at 365±10 nm UV irradiation by Al/TiO<sub>2</sub> hybrid structures. Photocatalytic bleaching of MB at 280±10 nm UV irradiation (b) at long-term (c) at short-term by Al/TiO<sub>2</sub> hybrid structures. Main mechanisms observed in photocatalytic bleaching of MB by Al/TiO<sub>2</sub> hybrid structures upon (d) 280±10 nm and (e) 365±10 nm ①: Electron-hole generation, ②: Reduction of Ti<sup>4+</sup> cations to Ti<sup>3+</sup> state, ③: Recombination, ④: Trapping of electrons by Al NPs and ⑤ Injection of electrons by Al NPs.

The difference between photocatalytic performance at 365 nm and 280 nm UV irradiation can be explained by two different mechanisms as depicted schematically in **Figure 58d**. At both wavelengths, electron-hole pairs are generated (Mechanism 1, **Figure 58d-e**) since in both cases bare TiO<sub>2</sub> exhibit photocatalytic activity (**Figure 58a-b**). The low photocatalytic activity of the deposited TiO<sub>2</sub> layer can be explained by the limited thickness and the lack of a high surface area (due to the lack of dense crack networks in such thin layers, as we presented recently [96]). Photogenerated electrons can reduce Ti<sup>4+</sup> cations to the Ti<sup>3+</sup> state and this may be followed by the degradation of MB (by directly attacking acceptors, as shown by Mechanism 2, **Figure 58d-e**) [118]. On the one hand, some photogenerated electrons from TiO<sub>2</sub> may overcome the SB and be trapped and localized in adjacent Al NPs (Mechanism 4, **Figure 58d**) [49]. These electrons may have the chance to gather on the surface of Al NPs (LSPR induced movement to the surface) and enhance the degradation of MB by promoting interaction with surrounding acceptors (**Figure 58d**). On

the other hand, some of trapped electrons can be injected back to TiO<sub>2</sub> (Mechanism 5, *Figure 58e*) which significantly triggers electron-hole recombination [49], thus negatively influencing the photocatalytic effect. At 280 nm UV irradiation, Mechanism 4 seems to dominate since the irradiation wavelength matches well with the plasmon absorption of Al NPs. But at 365 nm UV irradiation, the effect of LSPR is not strong enough to trigger the movement of trapped electrons to the surface of Al NPs. Rather, the Mechanism 5 (injection of electrons back to TiO<sub>2</sub>) possibly dominates and reduces the overall photocatalytic activity. It should be kept in mind that in both cases (280 nm and 365 nm irradiation) Mechanism 4 and Mechanism 5 coexist, but depending on the corresponding wavelength, one of them dominates.

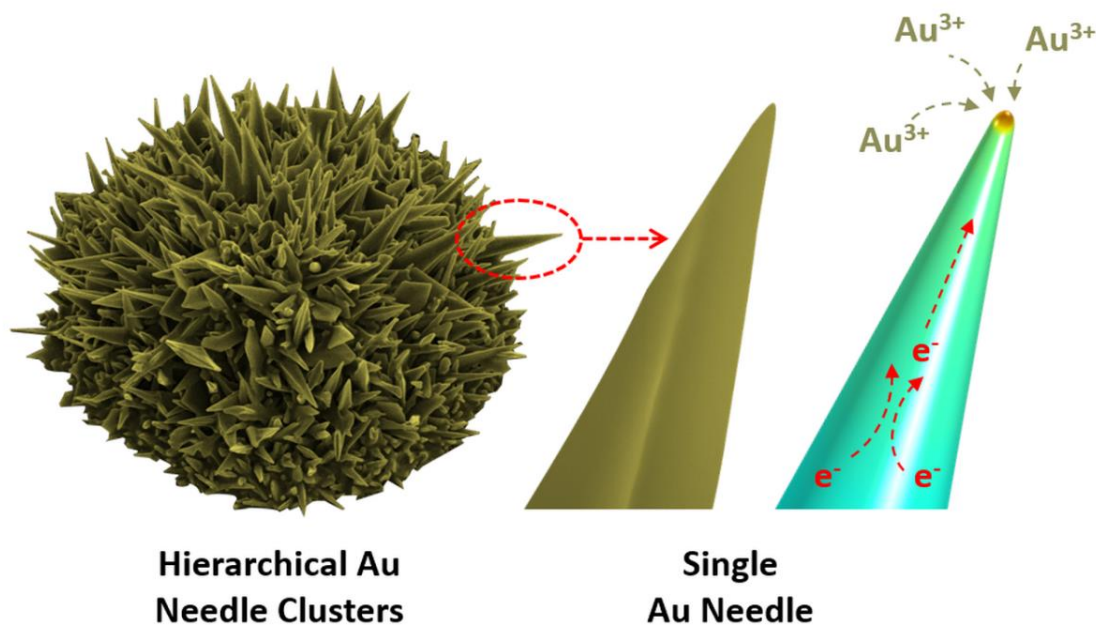
One can think about the shading effect of Al NPs on the TiO<sub>2</sub> surface, thus reducing the UV light-irradiated area during 365 nm UV irradiation. But then 80 nm Al NPs should have exhibited the lowest photocatalytic effect; conversely, at 365 nm UV irradiation 80 nm Al NPs exhibited slightly higher photocatalytic performance in comparison to 20 nm and 40 nm Al NPs. This may be explained by the injection of some electrons to Al NPs (Mechanism 4, *Figure 58d*) since the redshifted plasmon peak of 80 nm Al NPs provides relatively higher absorption (in comparison to 20 nm and 40 nm Al NPs) at 365 nm. But in all cases, the second mechanism seems to dominate under UV irradiation at a wavelength slightly further from the plasmonic absorption peak of Al NPs. These findings are in accordance with those of Lin et al. who similarly presented two mechanisms by selectively activating Au NPs and TiO<sub>2</sub> using two different wavelengths of 525 nm and 365 nm, respectively.[49]

### 6.3. Conclusion

The research on plasmonic photocatalysis has progressed steadily, but still the underlying mechanism has not yet been fully understood. Here, we could demonstrate for the first time the coexistence of effects both negative (injection of electron from Al NPs) and positive (trapping of electrons by Al NPs) of UV plasmonics on the photocatalytic activity of TiO<sub>2</sub>. We are aware that LSPR can influence the photocatalysis by various mechanisms, including sensitization (shifting absorption of TiO<sub>2</sub>), tuning bandgap energy (e.g. SB barrier formation), radiative and non-radiative decays and most of the time these mechanisms can co-exist. Therefore, the current study assists in understanding the mechanism of UV plasmonic photocatalysis under UV irradiation, which may help in designing new types of photocatalysts.

# Chapter 7. Photocatalytic Growth of Hierarchical Au Needle-Clusters on Highly Active TiO<sub>2</sub> Thin Film

In this chapter, the abstract, results and discussion as well as conclusion of the third research paper are presented. This includes, synthesis of Au structures on TiO<sub>2</sub> films. Hereafter, the effect of different parameters like intensity of UV or deposition time are analyzed by using SEM and HIM microscopy. Then, effect of different photocatalytically active and crystalline TiO<sub>2</sub> films (analyzed by MB bleaching and Raman spectroscopy, respectively) on the Au loading behavior was observed. Finally, the selective loading of Au structures on highly active TiO<sub>2</sub> films with special UV shadow mask is shown. Preparation method of TiO<sub>2</sub> thin films is already described in *section 4.1*.



## 7.1. Abstract

Hierarchical gold (Au) structures with sharp edges garner a strong interest for nano-electronics, nano-energy harvesting devices and nano-biomedical applications due the exceptional strong electric field (hot spot) enhancement at their tips. Herein, we report a facile method to synthesize hierarchical Au needle-clusters (HAuNCs) on highly active titanium-oxide (TiO<sub>2</sub>) thin film. Different than surfactant-directed photochemical assisted synthesis methods, we demonstrate a photocatalytic deposition approach, which allowed positioning and patterning of HAuNCs on TiO<sub>2</sub> target without using any surfactant or stabilizer. This green synthesis approach enabled us to control the size and the geometry of deposited HAuNCs by simply altering the photocatalytic activity of TiO<sub>2</sub> target, UV light intensity and irradiation time. Results and Discussion

## 7.2. Results and Discussion

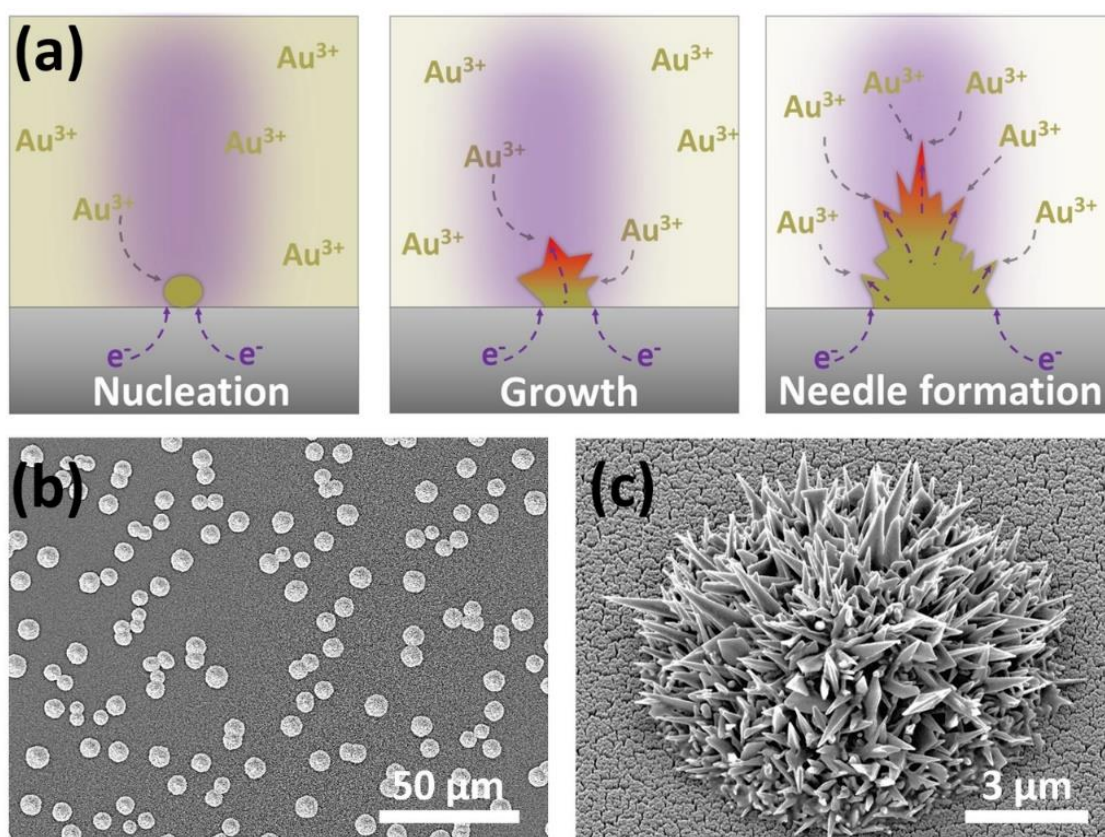
### 7.2.1. Photocatalytic Deposition of HAuNCs

In a typical experiment 600 nm layer of TiO<sub>2</sub> was sputter-deposited onto a silicon wafer according to the method we established [119]. Subsequently, we vertically dipped the prepared sample into a quartz cuvette filled with the aqueous HAuCl<sub>4</sub> solution. We used a UV-LED, operating at a wavelength of 365 nm and a UV light intensity of 4.5 mW/cm<sup>2</sup> to irradiate the sample surface through a UV-transparent quartz cuvette. The scheme given in shows the basic growth mechanism of a single HAuNC. First, UV irradiation generates electron-hole pairs in TiO<sub>2</sub> film and then Au<sup>3+</sup> ions (in aqueous solution) are reduced into a stable Au cluster by such densely generated electrons. The relative decrease of Au<sup>3+</sup> concentration on the surface, where first embryonic Au cluster nucleate, seems to promote the diffusion of more Au<sup>3+</sup> ions (from higher to lower concentration regions), followed by preferential piling of Au clusters into needle-like structures (HAuNCs shown in **Figure 59b**). We observed that the sharpness of such needle-like structures (**Figure 59c**) increased by the irradiation time which might be attributed to the high electron density at sharp edges (**Figure 60a-b**) promoting the preferential reduction of Au<sup>3+</sup>. Safei et al. showed the density of electrons was exceptionally high at sharp tips of branched Au nanostructures [120].

In a typical experiment we sputter-deposited a 600 nm thick TiO<sub>2</sub> layer onto a silicon wafer according to the method we reported earlier [119]. Subsequently, we vertically dipped the prepared sample into a quartz cuvette filled with the aqueous HAuCl<sub>4</sub> solution. We used a UV-LED, operating at a wavelength of 365 nm and a UV light intensity of 4.5 mW/cm<sup>2</sup>



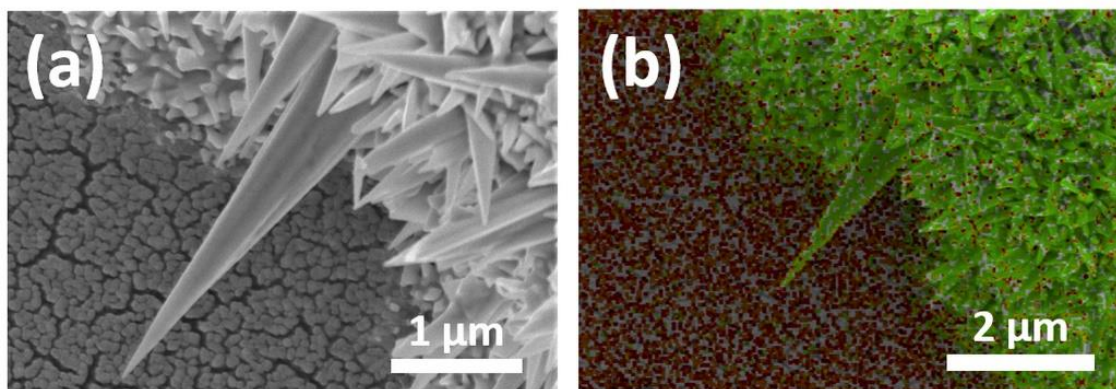
to irradiate the sample surface through a UV-transparent quartz cuvette. The scheme given in **Figure 59a** shows the basic growth mechanism of a single HAuNC. First, UV irradiation generates electron-hole pairs in TiO<sub>2</sub> film and then Au<sup>3+</sup> ions (in aqueous solution) are reduced into a stable Au cluster by such densely generated electrons. The relative decrease of Au<sup>3+</sup> concentration on the surface, where first embryonic Au cluster nucleate, seems to promote the diffusion of more Au<sup>3+</sup> ions (from higher to lower concentration regions), followed by preferential piling of Au clusters into needle-like structures (HAuNCs shown in **Figure 59b**). We observed that the sharpness of such needle-like structures (**Figure 59c**) increased by the irradiation time, which might be attributed to the high electron density at sharp edges (**Figure 60a-b**), promoting the preferential reduction of Au<sup>3+</sup>. As Safei et al. showed the density of electrons was exceptionally high at sharp tips of branched Au nanostructures [121].



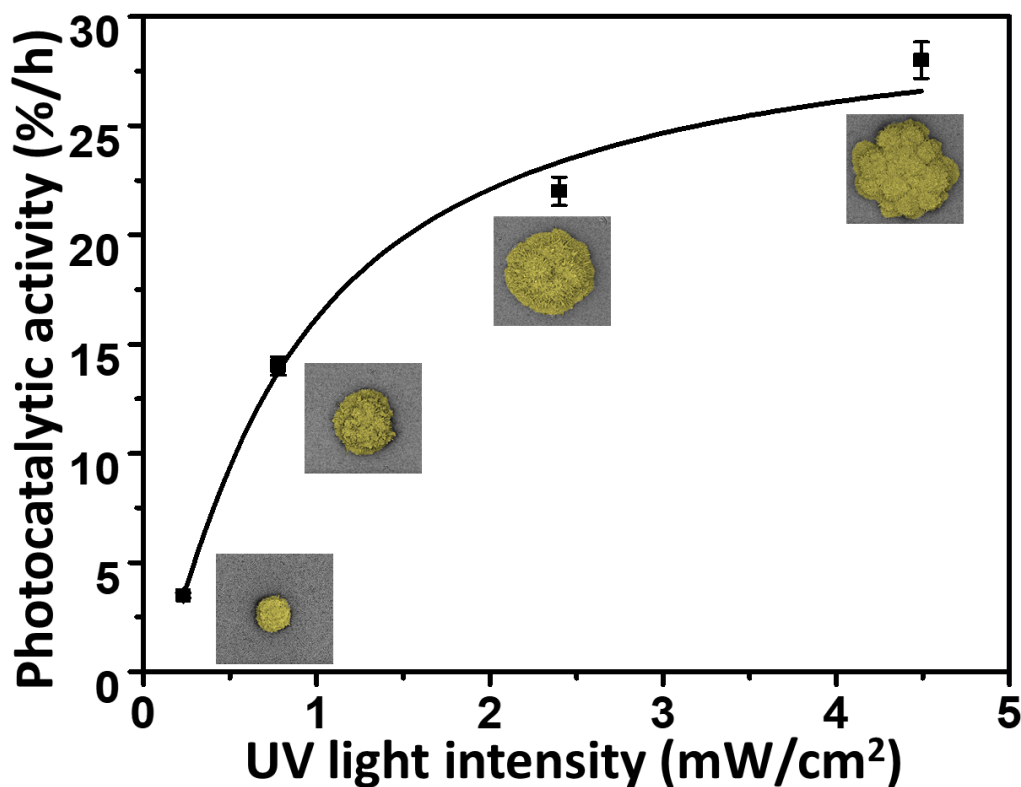
**Figure 59(a)** Schematic representation of HAuNC growth mechanism, **(b)** SEM images of HAuNCs deposited on TiO<sub>2</sub>, **(c)** HIM image of a single HAuNC.

It is known that higher UV light intensities lead to higher density of electron-hole generation in TiO<sub>2</sub> [119]. Therefore, we altered the UV light intensity to understand its influence on the growth of HAuNCs. In order to verify the change in the photocatalytic performance of TiO<sub>2</sub> by UV light intensity we immersed the prepared TiO<sub>2</sub> sample in an aqueous methylene blue (MB) solution and monitored the change in its absorption (at 664

nm as shown in **Figure 61**), as we described in detail previously [119]. Photocatalytic performances (photocatalytic bleaching of MB) at different light intensities were correlated with the morphology of HAuNCs as shown by insets given in **Figure 61** (achieved at corresponding light intensities). Sharper structures were observed at UV light intensity above  $2.4 \text{ mW/cm}^2$ , at which highest photocatalytic activities (which correspond to MB bleaching rate of 23 - 30 % per hour) were also achieved. Therefore, the final morphology of HAuNCs mainly depends on the density of the photo-generated electrons in  $\text{TiO}_2$  as well as the geometry of early embryonic Au clusters.

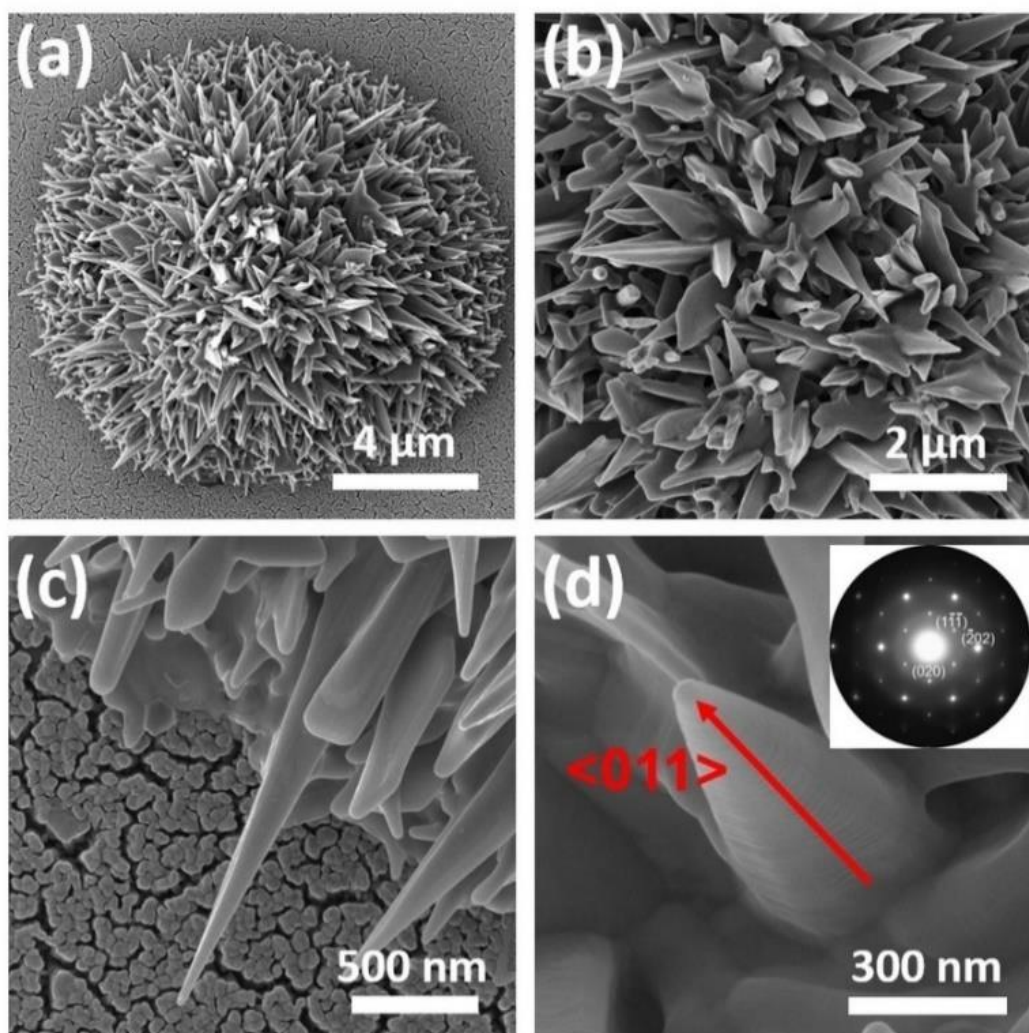


**Figure 60**(a) SEM image of a HAuNC and (b) EDX compositional mapping of HAuNCs (green and red areas represent presence of Au and  $\text{TiO}_2$ , respectively).



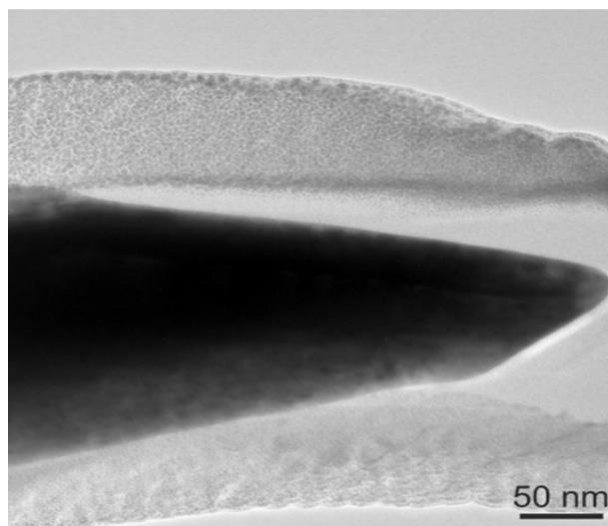
**Figure 61** Photocatalytic activity analysis (determined by the MB degradation) at different UV light intensities (inset shows SEM images of HAuNCs prepared at corresponding UV light intensity).

We examined the morphology of deposited HAuNCs in detail using Helium Ion Microscopy (HIM), and the corresponding images are presented in *Figure 62*. *Figure 62a* shows the low magnification HIM image of a single HAuNC, where needle-like structures are apparent with tip radius of 5–20 nm and length of 1–2  $\mu\text{m}$  (*Figure 62b*). At high resolution images, (*Figure 62c-d*), sharp needle-like Au nanostructures are clearly seen. After Focused Ion Beam (FIB) milling, we investigated the crystallinity and the growth direction of a single Au needle (taken from HAuNCs). The  $\langle 011 \rangle$  growth direction was confirmed by multiple selected area diffraction (SAED) patterns (inset, *Figure 62d*) in different zone axis from the depicted needle (see *Figure 63*). The single crystallinity was proven by SAED from different positions along the growth direction. Although the sample was prepared in cross section (FIB,) the sample thickness impedes further analysis by HRTEM imaging.



*Figure 62* HIM images of (a) a single HAuNC at low magnification, (b) needle-like Au structures which form hedgehog-like microstructure and (c-d) high magnification series showing needle-like Au nanostructures. Inset indicates SAED pattern ([101] zone axis) and the arrow represents the  $\langle 011 \rangle$  growth direction.

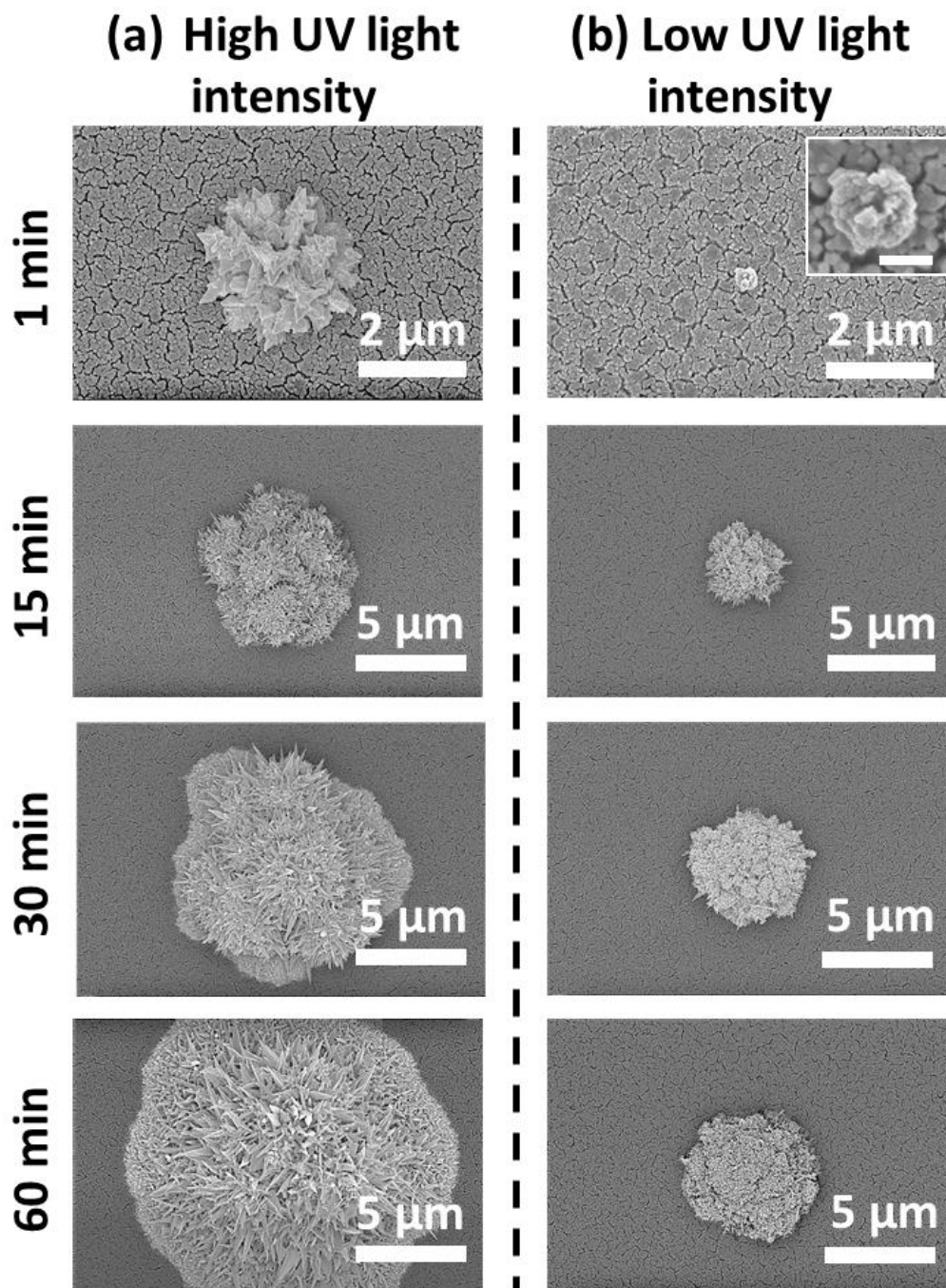




**Figure 63** TEM image of a single Au needle after Focused Ion Beam (FIB) milling.

### 7.2.2. The Influence of UV Light Intensity and Irradiation Time on the Growth of HAuNCs

We systematically altered the UV irradiation time (two different sets of samples exposed to *(a)* high-4.5 mW/cm<sup>2</sup> and *(b)* low-0.25 mW/cm<sup>2</sup> UV light intensity) to reveal details of the growth mechanism of HAuNCs (corresponding SEM images are given in **Figure 64a-b**). The Au atoms concentration increased gradually (by the UV irradiation time) as the Au<sup>3+</sup> ions got reduced. We have shown that the critical nucleus size of noble metals on dielectric surfaces is as small as a single atom.[122] Thus, already two metal atoms form a stable nucleus if they encounter each other. This is also expected for metal atoms in solution. When the Au atom concentration reached supersaturation they possibly formed aggregates, turning into small clusters through the heterogeneous nucleation (on the TiO<sub>2</sub> thin film). Once formed, these nuclei rapidly grew into larger sized nanocrystals within a short time (**Figure 64a**) and finally a hedgehog-like morphology was achieved. UV light intensity played a major role on the final morphology of the deposited Au nanostructures. While the high UV light intensity led to a fast nucleation and high growth rate (led to formation of larger Au nanostructures within a short time as shown in **Figure 64a**) we observed formation of much smaller Au clusters at low UV light intensity (**Figure 64b**). In addition, nucleated clusters got sharper by the time at high UV light intensity whereas less sharp and poorly ordered Au nanostructures formed at low UV light intensity.

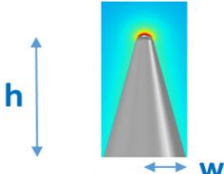
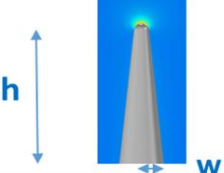
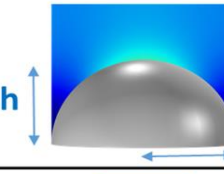
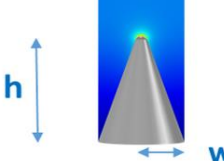


**Figure 64** SEM images of HAuNCs deposited at different irradiation time intervals (1-60 min) at (a) high UV light intensity ( $4.5 \text{ mW/cm}^2$ ) and (b) low UV light intensity ( $0.25 \text{ mW/cm}^2$ ) (inset scalebar: 200 nm)

In order to reveal the difference in the growth of Au nanostructures at high and low UV light intensity, by simulating the formation of the local electrical field enhancement (LEFE) around such structures at early and final growth stages using an electrochemical model[121] as shown in **Figure 65** (the morphology of Au particles given at **Figure 64** have been taken as structure model prototypes). Structures observed after 1 min irradiation were used to reveal the “early stage growth” mechanism. Whereas, sharper structures observed

after 60 min irradiation were taken as models for evaluating the “final stage growth” mechanism. Details are provided in *Table 3*.

*Table 3* Description of the model structures for the electrochemical simulation.

Representative structure model	Definition	Aspect Ratio (AR: h/w) h: height w: half width
	This model is created by considering the morphology of a single Au needle deposited after 1 min irradiation (high intensity) as shown in Figure 3a.	4
	This model is created by considering the morphology of a single Au needle deposited after 60 min irradiation (high intensity) as shown in Figure 3a.	10
	This model is created by considering the morphology of a single Au nanostructure deposited after 1 min irradiation (low intensity) as shown in Figure 3b.	-
	This model is created by considering the morphology of a single Au needle deposited after 60 min irradiation (low intensity) as shown in Figure 3b.	3

Following a fast nucleation (promoted by high density of electron/hole generation) at high UV light intensity, sharp Au structures (*Figure 64a*, 1 min) with an AR of 4 lead to a significant LEFE (*Figure 65a*, early stage). It is believed that high LEFE ( $E = 4.7 E_0$ , where  $E_0 = 1.33 \times 10^6$  V/m is the *reference* electric field magnitude for a 300 nm thick capacitor without any nanostructure present) enhances further accumulation of  $\text{Au}^{3+}$  ions and the subsequent promotion of the preferential reduction around sharp regions. In contrast, at low UV light intensity, the nucleation was slow (less Au accumulation led much smaller particles) and embryonic clusters seemed to exhibit a globular morphology (*Figure 64b*, 1 min), which we addressed to the lower electron/hole generation density. The lack of sharper regions led to a homogenous distribution of an electrical field (*Figure 65b*, early stage) rather than a local enhancement limiting the preferential reduction. Clearly AR of sharp structures (final stage) deposited at high UV light intensity is significantly higher than those deposited at low UV light intensity. A more detailed analysis reveals that the tip radius and AR play a major role on the LEFE at needle-like Au structures (*Figure 66*).

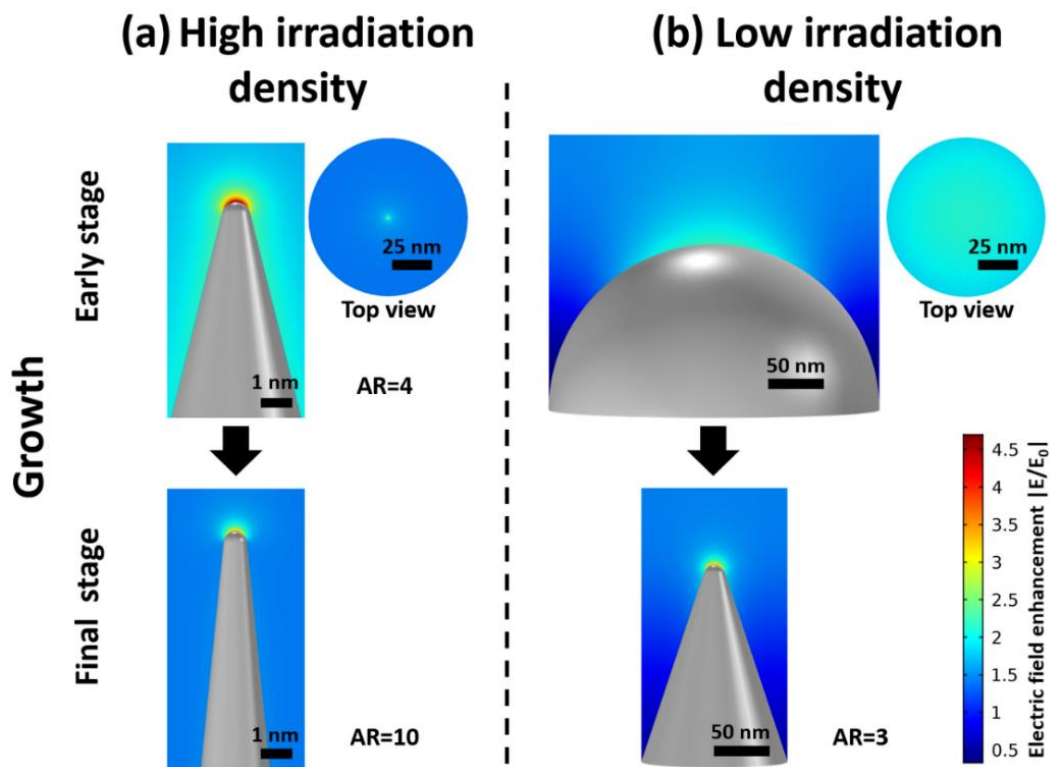


**Figure 65** Computed local electric field concentration around deposited Au nanostructures at (a) high UV light intensity (magnified images of the tip from a single needle as the model structure for early and final stage growth) and (b) low UV light intensity (spherical particle as the model for the early stage growth and needle-like geometry as the model for the final stage growth). In calculations,  $E_0 = 1.33 \times 10^6$  V/m and all structures correspond to morphologies visualized by SEM (**Figure 64**). Details are provided in **Table 3**.

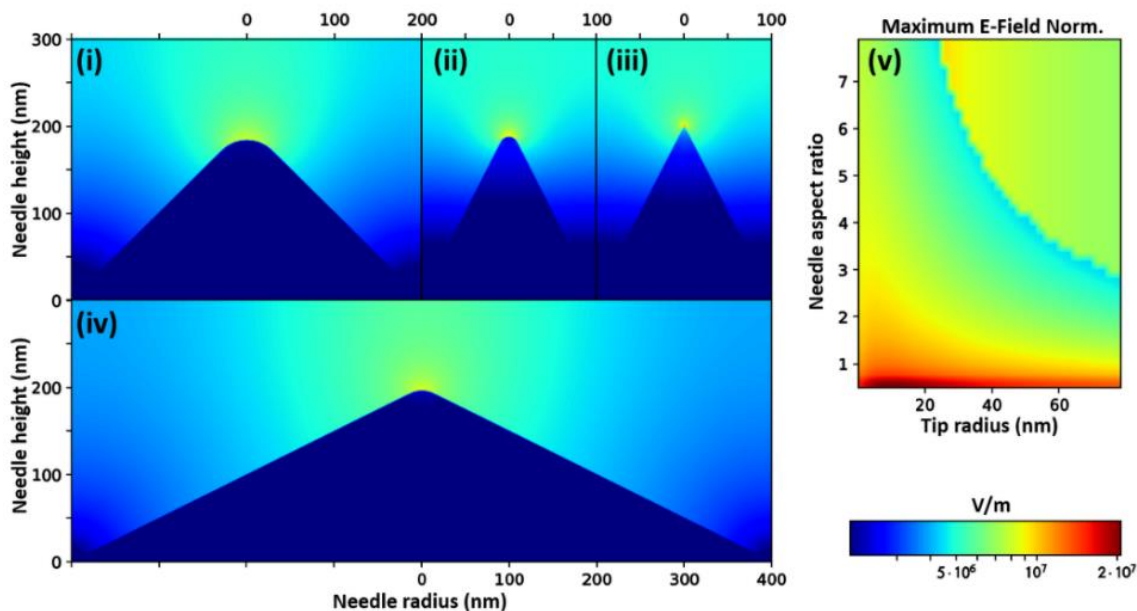


**Figure 66** Electrical field (E-field) magnitude (cut plane), from numerical (FEM) investigations of Au nano-needles (of fixed 200 nm height) inside a water-filled capacitor arrangement (300 nm height, 1 V external voltage). The left display shows the E-field magnitude around (and inside) the needles for varying aspect ratio (AR, calculated by needle height (of the corresponding perfect needle (tip radius=0)) divided by needle half-width) and needle tip radii R: (i)  $R=40$  nm and  $AR=1$ , (ii)  $R=10$  nm and  $AR=2$ , (iii)  $R=0.5$  nm  $AR=2$ , (iv)  $R=30$  nm and  $AR=1/2$ . The right display (v) shows the maximum E-field norm (on the needle tip) for swept aspect ratios and tip radii. For comparability, all plots obey the same, logarithmic color scale.

### 7.2.3. Controlling the Growth of H AuNCs by the Photocatalytic Activity of TiO<sub>2</sub>

In most of photocatalytic reduction studies the crystallinity, therefore the activity of the base material (to be loaded with Au), has not been evaluated in detail and its influence on the growth Au morphology is undermined. In order to evaluate the effect of the photocatalytic activity of the TiO<sub>2</sub> target on the growth mechanism of H AuNCs, we prepared a series of TiO<sub>2</sub> films which were composed of different crystal structures (heat-treated at different temperatures).

As depicted in **Figure 67**, TiO<sub>2</sub> film heat-treated at 550-650 °C exhibited the highest photocatalytic activity (photocatalytic bleaching of MB). Raman spectra (**Figure 68**) of the deposited layers also showed a good correlation with the photocatalytic activity analysis. The increase in the anatase content led to higher photocatalytic activity (**Figure 67**) and promoted the growth of much sharper and highly ordered Au nanostructures (**Figure 69a-b**). In contrast, we did not observe the formation of any Au nanostructure on amorphous and rutile (containing limited amount of anatase) TiO<sub>2</sub> films (**Figure 69a-b**). Our systematic analysis showed that crystallinity, UV light intensity and irradiation time were the main process parameters to control the size and geometry of deposited H AuNCs.

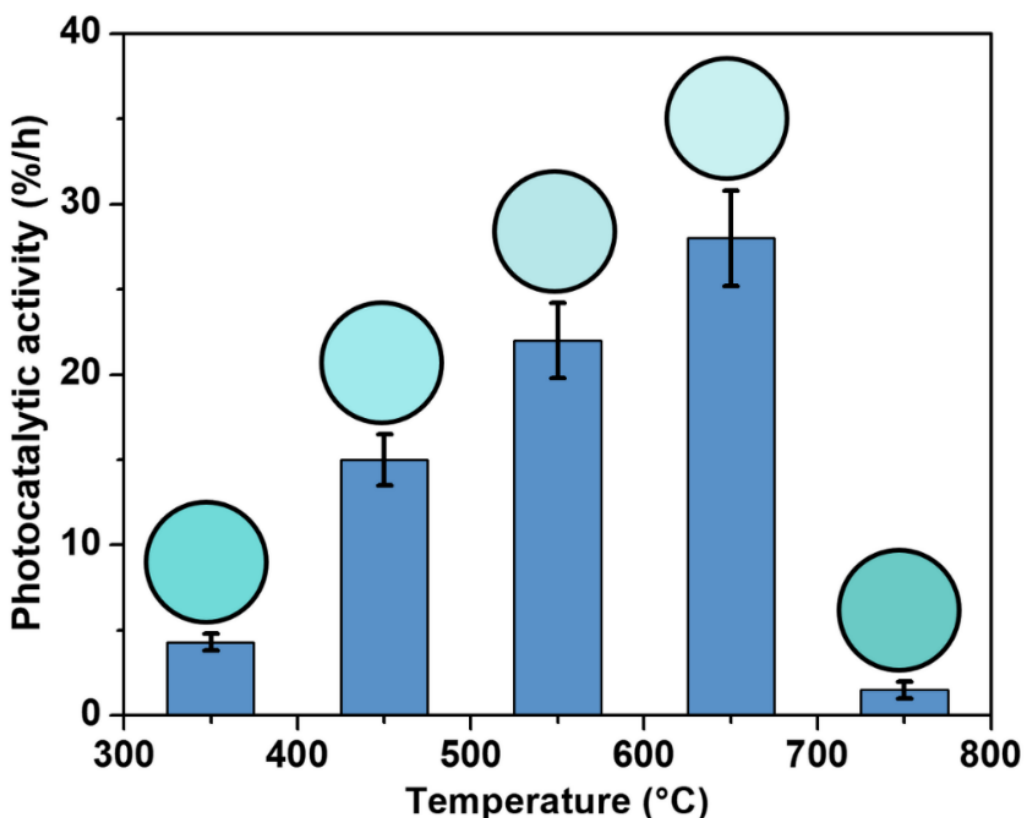


**Figure 67** Photocatalytic activity of TiO<sub>2</sub> thin films heat-treated at different temperatures (the circular insets show the change in the color of MB after 1h UV irradiation).



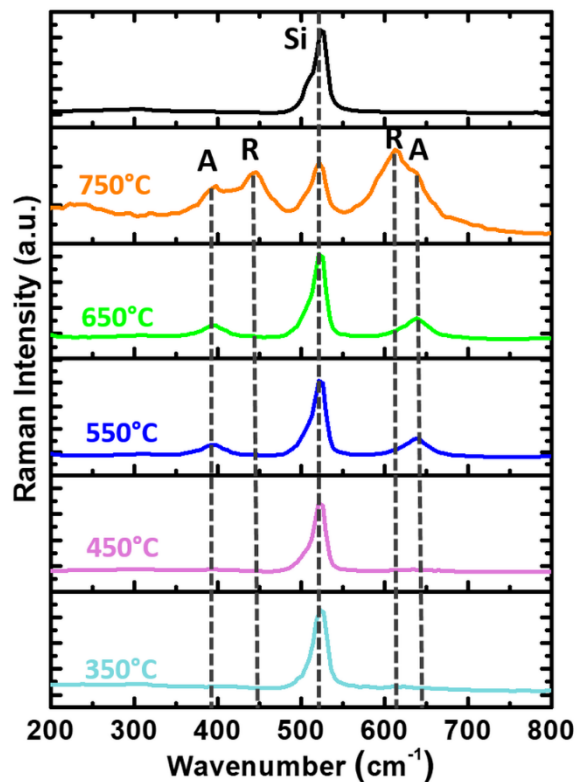


**Figure 68** Raman spectra of TiO<sub>2</sub> thin films heat-treated at different temperatures.

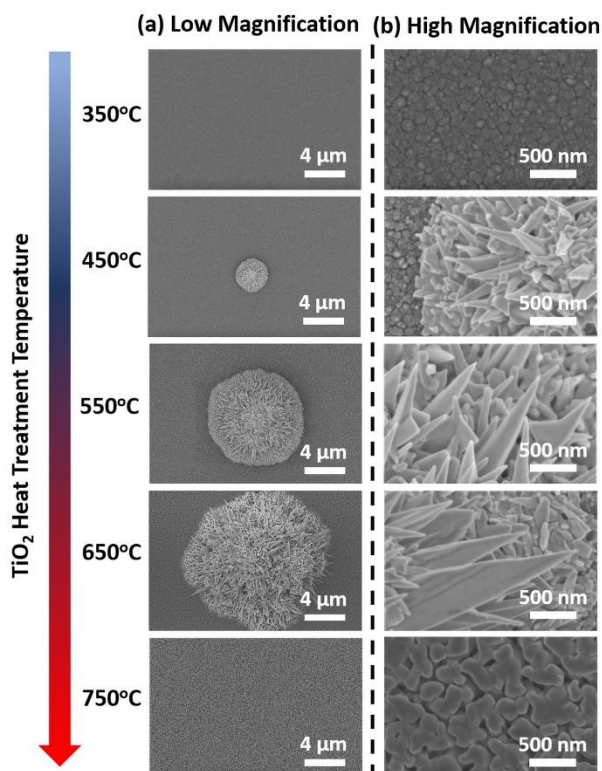


**Figure 69** SEM images of photocatalytic deposition of Au after 1h UV-irradiation (4.5 mW/cm<sup>2</sup>) on TiO<sub>2</sub> thin films heat-treated at different temperatures (*a*) at low magnification and (*b*) at high magnification.

## 7.2.4. Patterning TiO<sub>2</sub> Target by Selective Photocatalytic Deposition of HAuNCs

The presented approach allowed positioning and patterning HAuNCs on an active TiO<sub>2</sub> layer with help of a simple polymer mask (shown in *Figure 70a*), as presented in the scheme given in *Figure 71*. SEM images of HAuNCs deposited after 30 min UV irradiation through the polymer mask are depicted in *Figure 72a*. Corresponding elemental mapping imaging (*Figure 70b*) shows clearly that Au<sup>3+</sup> ions were reduced selectively on UV irradiated portions of TiO<sub>2</sub> layer. At a closer look one can see that HAuNCs are composed of extremely sharp needle-like structures (*Figure 72b*).

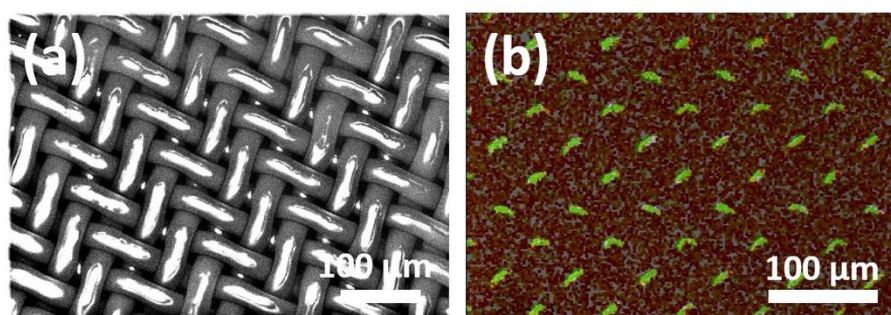


*Figure 70* (a) SEM image of the polymer mask used for patterning of TiO<sub>2</sub> thin film with HAuNCs and (b) elemental mapping analysis (by EDX) of TiO<sub>2</sub> thin film patterned with HAuNCs arrays (green and red areas represent presence of Au and TiO<sub>2</sub>, respectively).

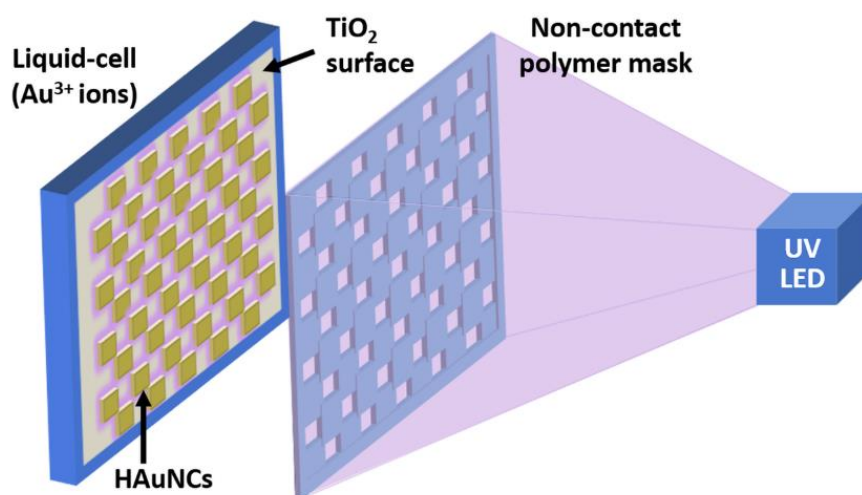


*Figure 71* Schematic representation of photocatalytic patterning on TiO<sub>2</sub> thin film with HAuNCs using a non-contact polymer mask.

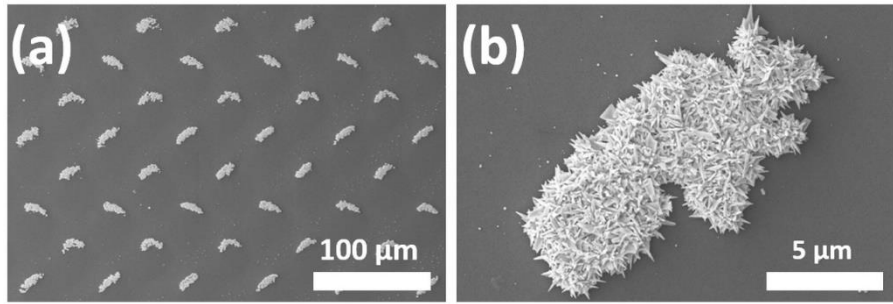


**Figure 72** SEM images of (a) periodic HAuNCs arrays and (b) a single HAuNC.

### 7.3. Conclusion

In conclusion, we demonstrated a facile method to fabricate HAuNCs by photocatalytic reduction of  $\text{Au}^{3+}$  ions on  $\text{TiO}_2$  film. This method allowed positioning and patterning of HAuNCs without using any surfactant or stabilizer. This green synthesis approach enables controlling the size and the geometry of deposited HAuNCs by simply altering the photocatalytic activity of  $\text{TiO}_2$  target, UV light intensity and irradiation time. **Figure 73** illustrates an understanding of the HAuNC growth mechanism and the influence of process parameters (photocatalytic activity of  $\text{TiO}_2$  target, UV light intensity and irradiation time) on the growth.

Local irradiation of the active  $\text{TiO}_2$  thin film through a simple non-contact mask led to local patterning with extremely sharp needle-like Au nanostructures, which may find application especially in catalysis, plasmonics and biomedical technologies (probing and manipulating biological processes).

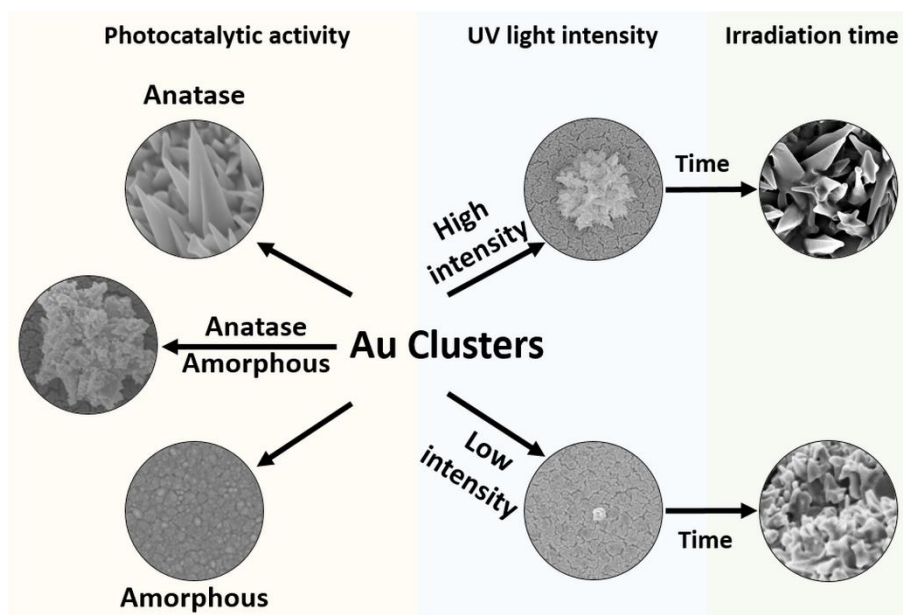


**Figure 73** Proposed synthesis pathway for controlling the growth and morphology of HAuNCs.

# Chapter 8. Summary

This dissertation includes three research papers outlined as follows:

1. A comparative study of photocatalysis on highly active columnar TiO<sub>2</sub> nanostructures in-air and in-solution.
2. The Role of UV plasmonics on photocatalytic performance of TiO<sub>2</sub> decorated with Al nanoparticles.
3. Photocatalytic growth of Hierarchical Au needle-clusters on highly active TiO<sub>2</sub> thin film.

## Conclusion:

- High AR columnar TiO<sub>2</sub> thin films have been prepared by pulsed DC reactive magnetron sputtering.
- Self-organized nanocrack networks on TiO<sub>2</sub> films with improved surface area and high photocatalytic efficiency have been achieved by fast heating and cooling (heat-treatment) process.
- A new and fast analytical method based on characterization conditions (in-air or dry conditions) was developed to observe on-site photocatalytic activity of thin films and compared by using the standard analytical method (in-aqueous solution or wet conditions).
- Photocatalytic activity of sputter-deposited TiO<sub>2</sub> thin films was compared with a reference sample (standard P25 TiO<sub>2</sub>) using two analytical methods (standard and newly developed). Sputter-deposited TiO<sub>2</sub> thin films exhibited 3-times higher photocatalytic activity.
- First time, reversible and irreversible conversion of MB $\rightleftharpoons$ LMB and MB photocatalytic bleaching (induced by TiO<sub>2</sub>) have been observed simultaneously.
- Al NPs with controlled size, shape, crystallinity and plasmonic properties were produced by GAS technique.
- High stability of Al NPs was achieved by controlled oxidation via reactive DC sputtering using GAS synthesis approach.
- Enhanced photocatalytic efficiency was achieved by plasmonic Al NPs decorated on highly transparent TiO<sub>2</sub> thin films, compared to pristine highly transparent TiO<sub>2</sub> thin films.

- A facile (surfactant free) method was developed to synthesize hierarchical Au structures on TiO<sub>2</sub> thin film.
- Au micro- and nanostructures with controlled size, morphology and crystallinity were achieved by controlling the reduction of Au<sup>+3</sup> on TiO<sub>2</sub> surface.
- Sharp hierarchical (AR: 10) Au nanostructures were attained on highly photocatalytic active columnar TiO<sub>2</sub> surfaces.
- Selective surface patterning by Au structures (on TiO<sub>2</sub>) was achieved through selective photocatalytic activation of TiO<sub>2</sub> thin film.

# Chapter 9. Outlook

Following studies, which possibly will be continued by new M.Sc. and PhD candidates, will lead to a better understanding of the proposed mechanisms and as well as further functional applications:

- Tuning plasmonic properties of Al NPs by controlling their size and encapsulating oxide thickness.
- Fabrication of novel surfaces composed of Al NPs for Surface Enhanced Raman scattering (SERS) applications (operating at UV to near-infrared spectrum).
- Synthesis of multilayer e.g.  $\text{TiO}_2/\text{Al}/\text{TiO}_2$  or  $\text{Al}/\text{TiO}_2/\text{Al}$  structures by reactive sputtering in combination with the GAS technique (a preliminary study is shown in **Figure 74** by SEM images of  $\text{TiO}_2/\text{Al}/\text{TiO}_2$  multilayers).

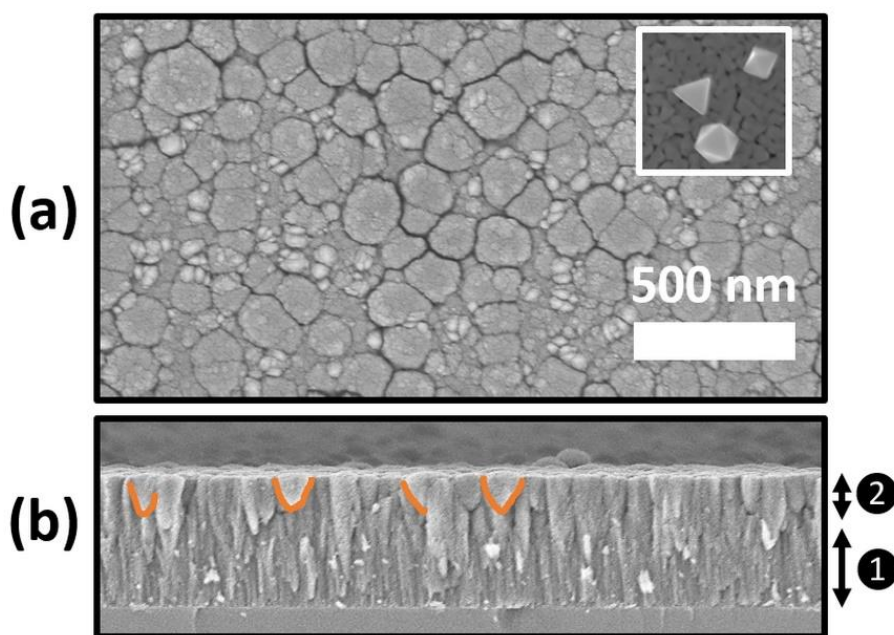


**Figure 74** (a) SEM micrograph of multilayers  $\text{TiO}_2\text{-Al-TiO}_2$  structures (inset shows SEM image of Al decorated NPs over the bottom  $\text{TiO}_2$  layer) (b) cross-sectional view of SEM micrograph, ① represents the bottom  $\text{TiO}_2$  layer and ② represents the Al NPs covered with  $\text{TiO}_2$  top layer (marked orange color areas are the Al NPs covered with sputtered  $\text{TiO}_2$  film)

- Design and preparation of  $\text{CeO}_2\text{-TiO}_2$  hybrid thin films by co-sputtering from Ti and Ce targets for high photocatalytic applications.
- Incorporation of Al clusters in co-deposited  $\text{CeO}_2\text{-TiO}_2$  hybrid thin films to enhance photocatalytic performance.
- The Al NPs will be used to develop broadband UV absorbers covering not only UV-A but also UV-B and a part of UV-C.



# Bibliography

- [1] C.F. Goodeve, J.A. Kitchener, Photosensitisation by Titanium Dioxide, *Trans. Faraday Soc.* 34 (1938) 570–579.
- [2] A. Fujishima, K. Honda, Electrochemical Photolysis of Water at a Semiconductor Electrode, *Nature*. 238 (1972) 37–38.
- [3] A.O. Ibhaddon, P. Fitzpatrick, Heterogeneous Photocatalysis: Recent Advances and Applications, *Catalysts*. 3 (2013) 189–218.
- [4] M. Gagliardi, Photocatalysts: Technologies and Global Markets, BCC Research Report, 2015.
- [5] A.T. Mecherikunnel, J.C. Richmond, Spectral Distribution of Solar Radiation, Technical Memorandum, 1980.
- [6] T. Luttrell, S. Halpegamage, J. Tao, A. Kramer, E. Sutter, M. Batzill, Why is anatase a better photocatalyst TiO<sub>2</sub> films, *Sci. Rep.* 4 (2014) 1–8.
- [7] R. Thiruvenkatachari, S. Vigneswaran, I.S. Moon, A review on UV/TiO<sub>2</sub> photocatalytic oxidation process, *Korean J. Chem. Eng.* 25 (2008) 64–72.
- [8] S. Shuang, R. Lv, Z. Xie, Z. Zhang, Surface Plasmon Enhanced Photocatalysis of Au/Pt-decorated TiO<sub>2</sub> Nanopillar Arrays, *Sci. Rep.* 6 (2016) 26670.
- [9] N. Corrigan, S. Shanmugam, C. Boyer, Photocatalysis in organic and polymer synthesis, *Chem. Soc. Rev.* 45 (2016) 6165–6212.
- [10] I.A. Sayed, G.E. Kenny, Effects of Reducing Agents, Catalase, and Reuse of Medium on Toxicity of Media for Growth of *Ureaplasma urealyticum*, *J. Infect. Dis.* 139 (1979) 720–724.
- [11] E.T. Wahyuni, A. Kuncaka, S. Sutarno, Application of Photocatalytic Reduction Method with TiO<sub>2</sub> for Gold Recovery, *Am. J. Appl. Chem.* 3 (2015) 207–211.
- [12] X. Zhang, L. Song, X. Zeng, M. Li, Effects of Electron Donors on the TiO<sub>2</sub> Photocatalytic Reduction of Heavy Metal Ions under Visible Light, *Energy Procedia*. 17 (2012) 422–428.
- [13] E. Albiter, M.A. Valenzuela, S. Alfaro, G. Valverde-aguilar, F.M. Martí'nez-Pallares, Photocatalytic deposition of Ag nanoparticles on TiO<sub>2</sub>: Metal precursor effect on the structural and photoactivity properties, *J. Saudi Chem. Soc.* 19 (2015) 563–573.
- [14] [www.sciencedirect.com](http://www.sciencedirect.com), Search results for: Photocatalysis and TiO<sub>2</sub> Photocatalysis, (2018).
- [15] M. Skocaj, M. Filipic, J. Petkovic, S. Novak, Titanium dioxide in our everyday life; is it safe?, *Radiol. Oncol.* 45 (2015) 227–247.
- [16] E. Santos, N.K. Kuromoto, A. Soares, Mechanical properties of titania films used as biomaterials, *Mater. Chem. Phys.* 102 (2007) 92–97.
- [17] A. Sodagar, M. Sadegh, A. Akhouni, A. Bahador, Effect of TiO<sub>2</sub> nanoparticles incorporation on antibacterial properties and shear bond strength of dental composite used in Orthodontics, *Dent. Press J Orthod.* 22 (2017) 67–74.
- [18] D. Press, Titanium dioxide and zinc oxide nanoparticles in sunscreens: focus on their safety and effectiveness, *Nanotechnol. Sci. Appl.* 4 (2011) 95–112.
- [19] J.H. Braun, A. Baidins, R.E. Marganski, TiO<sub>2</sub> pigment technology: a review, *Prog.*

Org. Coatings. 20 (1992) 105–138.

- [20] S. Banerjee, D.D. Dionysiou, S.C. Pillai, Self-cleaning applications of TiO<sub>2</sub> by photo-induced hydrophilicity and photocatalysis, *Appl. Catal. B Environ.* 176–177 (2015) 396–428.
- [21] G. Bolte, *Nanotechnology in Construction* 3, 2009.
- [22] Y. Yilmaz, *Phthalocyanines and Some Current Applications*, 2017.
- [23] A. Biswas, O.C. Aktas, U. Schürmann, U. Saeed, V. Zaporojtchenko, U. Saeed, V. Zaporojtchenko, F. Faupel, Tunable multiple plasmon resonance wavelengths response from multicomponent polymer-metal nanocomposite systems., *Appl. Phys. Lett.* 84 (2004) 2655–2657.
- [24] H.T. Beyene, V.S.K. Chakravadhanula, C. Hanisch, M. Elbahri, T. Strunskus, V. Zaporojtchenko, L. Kienle, F. Faupel, Preparation and plasmonic properties of polymer-based composites containing Ag – Au alloy nanoparticles produced by vapor phase co-deposition, *J. Mater Sci.* 45 (2010) 5865–5871.
- [25] M.J. McClain, A.E. Schlather, E. Ringe, N.S. King, L. Liu, A. Manjavacas, M.W. Knight, I. Kumar, K.H. Whitmire, H.O. Everitt, P. Nordlander, N.J. Halas, Aluminum Nanocrystals, *Nano Lett.* 15 (2015) 2751–2755.
- [26] M.W. Knight, N.S. King, L. Liu, H.O. Everitt, P. Nordlander, N.J. Halas, Aluminum for Plasmonics, *ACS Nano.* 8 (2014) 834–840.
- [27] M.W. Knight, L. Liu, Y. Wang, L. Brown, S. Mukherjee, N.S. King, H.O. Everitt, P. Nordlander, N.J. Halas, Aluminum plasmonic nanoantennas, *Nano Lett.* 12 (2012) 6000–6004.
- [28] S.K. Jha, Z. Ahmed, M. Agio, Y. Ekinici, J.F. Löffler, Deep-UV surface-enhanced resonance Raman scattering of adenine on aluminum nanoparticle arrays, *J. Am. Chem. Soc.* 134 (2012) 1966–1969.
- [29] S.J. Tan, L. Zhang, D. Zhu, X.M. Goh, Y.M. Wang, K. Kumar, C.W. Qiu, J.K.W. Yang, Plasmonic color palettes for photorealistic printing with aluminum nanostructures, *Nano Lett.* 14 (2014) 4023–4029.
- [30] M. Zayat, P. Garcia-parejo, D. Levy, Preventing UV-light damage of light sensitive materials using a highly protective UV-absorbing coating, *Chem. Soc. Rev.* 36 (2007) 1270–1281.
- [31] Harpercollins, *Collins English Dictionary-Complete and Unabridged edition*, (2014).
- [32] N. Costa, A. Cartaxo, *Advances in Lasers and Electro Optics: Chapter 13, The Intersubband Approach to Si-based Lasers*, 2010.
- [33] V.A. Online, J. Chang, E.R. Waclawik, Colloidal semiconductor nanocrystals: controlled synthesis and surface chemistry in organic media, *RSC Adv.* 4 (2014) 23505–23527.
- [34] S. Bai, W. Jiang, Z. Li, Y. Xiong, *Surface and Interface Engineering in Photocatalysis*, *Chem Nano Mat.* 1 (2015) 223–239.
- [35] J. Schneider, M. Matsuoka, M. Takeuchi, J. Zhang, Y. Horiuchi, M. Anpo, D.W. Bahnemann, Understanding TiO<sub>2</sub> Photocatalysis: Mechanisms and Materials, *Chem. Rev.* 114 (2014) 9919–9986.
- [36] H.C. Junqueira, D. Severino, L.G. Dias, M.S. Gugliotti, M.S. Baptista, Modulation of methylene blue photochemical properties based on adsorption at aqueous micelle interfaces, *Phys. Chem. Chem. Phys.* 4 (2002) 2320–2328.



- [37] A. Houas, H. Lachheb, M. Ksibi, E. Elalouui, C. Guillard, J.-M. Herrmann, Photocatalytic degradation pathway of methylene blue in water, *Appl. Catal. B Environ.* 31 (2001) 145–157.
- [38] A. Mills, C. O'Rourke, Adsorption and destruction of methylene blue by semiconductor photocatalysis, *Green.* 1 (2011) 105–113.
- [39] W. Wang, N. Xie, L. He, Y. Yin, Photocatalytic colour switching of redox dyes for ink-free light-printable rewritable paper, *Nat. Commun.* 5 (2014).
- [40] A.J. Hallock, E.S.F. Berman, R.N. Zare, Ultratrace kinetic measurements of the reduction of methylene blue, *J. Am. Chem. Soc.* 125 (2003) 1158–1159.
- [41] R. Dagher, P. Drogui, D. Robert, Modified TiO<sub>2</sub> For Environmental Photocatalytic Applications: A Review, *Ind. Eng. Chem. Res.* 52 (2013) 3581–3599.
- [42] S. Veziroglu, M. Kuru, M.Z. Ghorri, F.K. Dokan, A.M. Hinz, T. Strunskus, F. Faupel, O.C. Aktas, Ultra-fast degradation of methylene blue by Au/ZnO-CeO<sub>2</sub> nano-hybrid catalyst, *Mater. Lett.* 209 (2017) 486–491.
- [43] I. Alessandri, Enhancing Raman Scattering without Plasmons: Unprecedented Sensitivity Achieved by TiO<sub>2</sub> Shell-Based Resonators, *J. Am. Chem. Soc.* 135 (2013) 5541–5544.
- [44] M.K. Hedayati, F. Faupel, M. Elbahri, Review of Plasmonic Nanocomposite Metamaterial Absorber, *Materials (Basel).* 7 (2014) 1221–1248.
- [45] M.K. Hedayati, A.U. Zillohu, T. Strunskus, F. Faupel, M. Elbahri, M.K. Hedayati, A.U. Zillohu, T. Strunskus, F. Faupel, M. Elbahri, Plasmonic tunable metamaterial absorber as ultraviolet protection film, *Appl. Phys. Lett.* 104 (2014) 11–16.
- [46] J. Zhang, L. Zhang, W. Xu, Surface plasmon polaritons: physics and applications, *J. Phys. D. Appl. Phys.* 45 (2012) 113001.
- [47] H. Search, C. Journals, A. Contact, M. Iopscience, I.P. Address, Equal intensity double plasmon resonance of bimetallic quasi-nanocomposites based on sandwich geometry, *Nanotechnology.* 19 (2008) 1–5.
- [48] F. Faupel, V. Zaporozhchenko, T. Strunskus, Metal-Polymer Nanocomposites for Functional Applications, *Adv. Eng. Mater.* 12 (2010) 1177–1190.
- [49] Z. Lin, X. Wang, J. Liu, Z. Tian, L. Dai, B. He, C. Han, Y. Wu, Z. Zeng, Z. Hu, On the role of localized surface plasmon resonance in UV-Vis light irradiated Au/TiO<sub>2</sub> photocatalysis systems: pros and cons, *Nanoscale.* 7 (2015) 4114–4123.
- [50] M. Honda, Y. Kumamoto, A. Taguchi, Y. Saito, S. Kawata, Plasmon-enhanced UV photocatalysis, *Appl. Phys. Lett.* 104 (2014) 061108.
- [51] A. Piot, S.K. Earl, C. Ng, S. Dligatch, A. Roberts, T.J. Davis, D.E. Gómez, Collective excitation of plasmonic hot-spots for enhanced hot charge carrier transfer in metal/semiconductor contacts, *Nanoscale.* 7 (2015) 8294–8298.
- [52] S. Tian, O. Neumann, M.J. McClain, X. Yang, L. Zhou, C. Zhang, P. Nordlander, N.J. Halas, Aluminum nanocrystals: A sustainable substrate for quantitative SERS-Based DNA Detection, *Nano Lett.* 17 (2017) 5071–5077.
- [53] M. Abdulla-Al-Mamun, Y. Kusumoto, T. Zannat, M.S. Islam, Synergistic enhanced photocatalytic and photothermal activity of Au@TiO<sub>2</sub> nanopellets against human epithelial carcinoma cells, *Phys. Chem. Chem. Phys.* 13 (2011) 21026.
- [54] M.M. Khan, J. Lee, M.H. Cho, Journal of Industrial and Engineering Chemistry Au @ TiO<sub>2</sub> nanocomposites for the catalytic degradation of methyl orange and methylene blue : An electron relay effect, *J. Ind. Eng. Chem.* 20 (2014) 1584–1590.

- [55] W.R. Grove, On the Electro-Chemical Polarity of Gases, *Philos. Trans. R. Soc. London.* 142 (1852) 87–101.
- [56] I. Langmuir, The mechanism of the surface phenomena of flotation, *Trans. Faraday Soc.* 15 (1920) 62.
- [57] R. Behrisch, W. Eckstein, Sputtering by Particle Bombardment: Experiments and Computer Calculations from Threshold to MeV energies, *Top. Appl. Phys.* 110 (2007) 1–526.
- [58] Y. Huttel, *Gas-Phase Synthesis of Nanoparticles*, 2017.
- [59] B. Window, N. Savvides, Charged particle fluxes from planar magnetron sputtering sources, *J. Vac. Sci. Technol. A Vacuum, Surfaces, Film.* 4 (1986) 196–202.
- [60] E. Alfonso, J. Olaya, G. Cubillos, Thin Film Growth Through Sputtering Technique and Its Applications, in: *Cryst. - Sci. Technol., InTech*, 2012.
- [61] B.A. Movchan, A. V Demchishin, Investigation of the structure and B A Movchan, A V Demchishin properties of thick vacuum- deposited films of nickel, titanium, tungsten, alumina and zirconium dioxide, *Fiz. Met. I Metalloved.* 28 (1969) 653–660.
- [62] J.A. Thornton, Influence of apparatus geometry and deposition conditions on the structure and topography of thick sputtered coatings, *J. Vac. Sci. Technol.* 11 (1974) 666–670.
- [63] E. Alfonso, G. Cubillos, J. Olaya, *Thin Film Growth Through Sputtering Technique and Its Applications*, 2012.
- [64] R. Messier, Revised structure zone model for thin film physical structure, *J. Vac. Sci. Technol. A Vacuum, Surfaces, Film.* 2 (1984) 500.
- [65] T. Karabacak, J.P. Singh, Y.-P. Zhao, G.-C. Wang, T.-M. Lu, Scaling during shadowing growth of isolated nanocolumns, *Phys. Rev. B.* 68 (2003) 125408.
- [66] K.S. Sree Harsha, Dry Etching, in: *Princ. Vap. Depos. Thin Film.*, Elsevier, 2006: pp. 1073–1134.
- [67] S.A. Koch, R.H. te Velde, G. Palasantzas, J.T.M. De Hosson, Magnetic versus structural properties of Co nanocluster thin films: A magnetic force microscopy study, *Appl. Phys. Lett.* 84 (2004) 556–558.
- [68] T. Vystavel, G. Palasantzas, S.A. Koch, J.T.M. De Hosson, Nanosized iron clusters investigated with in situ transmission electron microscopy, *Appl. Phys. Lett.* 82 (2003) 197–199.
- [69] O. Polonskyi, O. Kylián, M. Drábik, J. Kousal, P. Solař, A. Artemenko, J. Čechvala, A. Choukourov, D. Slavínská, H. Biederman, Deposition of Al nanoparticles and their nanocomposites using a gas aggregation cluster source, *J. Mater. Sci.* 49 (2014) 3352–3360.
- [70] J. Kousal, O. Polonskyi, O. Kylián, A. Choukourov, A. Artemenko, J. Pešička, D. Slavínská, H. Biederman, Characterization of nanoparticle flow produced by gas aggregation source, *Vacuum.* 96 (2013) 32–38.
- [71] E.E. Finney, R.G. Finke, Nanocluster nucleation and growth kinetic and mechanistic studies: A review emphasizing transition-metal nanoclusters, *J. Colloid Interface Sci.* 317 (2008) 351–374.
- [72] M. Khojasteh, V. V. Kresin, Influence of source parameters on the growth of metal nanoparticles by sputter-gas-aggregation, *Appl. Nanosci.* 7 (2017) 875–883.

- [73] T. Peter, O. Polonskyi, B. Gojdka, A. Mohammad Ahadi, T. Strunskus, V. Zaporozhchenko, H. Biederman, F. Faupel, Influence of reactive gas admixture on transition metal cluster nucleation in a gas aggregation cluster source, *J. Appl. Phys.* 112 (2012) 114321 (1-6).
- [74] S. Drache, V. Stranak, F. Berg, Z. Hubicka, M. Tichy, C.A. Helm, R. Hippler, Pulsed gas aggregation for improved nanocluster growth and flux, *Phys. Status Solidi.* 211 (2014) 1189–1193.
- [75] A Dictionary of Chemistry 6th Edition, Stark-Einstein-Law. (2008).
- [76] E.L. Wehry, Photochemical behaviour of transition-metal complexes, *Q. Rev. Chem. Soc.* 21 (1967) 213.
- [77] T.H. Fleisch, G.W. Zajac, J.O. Schreiner, G.J. Mains, An XPS study of the UV photoreduction of transition and noble metal oxides, *Appl. Surf. Sci.* 26 (1986) 488–497.
- [78] X. Liu, J. Iocozzia, Y. Wang, X. Cui, Y. Chen, S. Zhao, Z. Li, Z. Lin, Noble metal–metal oxide nanohybrids with tailored nanostructures for efficient solar energy conversion, photocatalysis and environmental remediation, *Energy Environ. Sci.* 10 (2017) 402–434.
- [79] P.A. Morris Hotsenpiller, J.D. Bolt, W.E. Farneth, J.B. Lowekamp, G.S. Rohrer, Orientation Dependence of Photochemical Reactions on TiO<sub>2</sub> Surfaces, *J. Phys. Chem. B.* 102 (1998) 3216–3226.
- [80] R. Djellabi, M.F. Ghorab, Photoreduction of toxic chromium using TiO<sub>2</sub> - immobilized under natural sunlight: effects of some hole scavengers and process parameters, *Desalin. Water Treat.* 55 (2015) 1900–1907.
- [81] R. Kydd, J. Scott, W.Y. Teoh, K. Chiang, R. Amal, Understanding photocatalytic metallization of preadsorbed ionic gold on titania, ceria, and Zirconia, *Langmuir.* 26 (2010) 2099–2106.
- [82] R. Robbins, Scanning Electron Microscope Operation Zeiss Supra-40, 2015.
- [83] J.F. Moulder, W.F. Stickle, P.E. Sobol, K.D. Bomben, Handbook of X-ray photoelectron spectroscopy: a reference book of standard spectra for identification and interpretation of XPS data, 1992.
- [84] V. Everts, A. Niehof, W. Tigchelaar-Gutter, W. Beertsen, Transmission Electron Microscopy of Bone, in: *Mater. Sci.*, 2012: pp. 351–363.
- [85] Y. Ozaki, S. Šašić, Introduction to Raman Spectroscopy, *Pharm. Appl. Raman Spectrosc.* (2007) 1–28.
- [86] G. Hlawacek, V. Veligura, R. van Gastel, B. Poelsema, Helium ion microscopy, *J. Vac. Sci. Technol. B, Nanotechnol. Microelectron. Mater. Process. Meas. Phenom.* 32 (2014) 020801.
- [87] A. Mills, C. Hill, P.K.J. Robertson, Overview of the current ISO tests for photocatalytic materials, *J. Photochem. Photobiol. A Chem.* 237 (2012) 7–23.
- [88] A. Hernández-Ramírez, I. Medina-Ramírez, Photocatalytic Semiconductors, 2015.
- [89] A.J. Julson, D.F. Ollis, Kinetics of dye decolorization in an air–solid system, *Appl. Catal. B Environ.* 65 (2006) 315–325.
- [90] A. Mills, Photocatalyst Products and Testing Centre, Queens University Belfast, (2018).
- [91] A. Mills, J. Wang, Photobleaching of methylene blue sensitised by TiO<sub>2</sub>: an

- ambiguous system?, *J. Photochem. Photobiol. A Chem.* 127 (1999) 123–134.
- [92] A. Mills, J. Hepburn, M. McFarlane, A novel, fast-responding, indicator ink for thin film photocatalytic surfaces, *ACS Appl. Mater. Interfaces.* 1 (2009) 1163–1165.
- [93] H. Haberland, M. Karrais, M. Mall, Y. Thurner, Thin films from energetic cluster impact: A feasibility study, *J. Vac. Sci. Technol. A Vacuum, Surfaces, Film.* 10 (1992) 3266–3271.
- [94] J.F. Moulder, W.F. Stickle, P.E. Sobol, K.D. Bomben, *Handbook of X-ray Photoelectron Spectroscopy* Edited by, (1992) 261.
- [95] I. Petrov, P.B. Barna, L. Hultman, J.E. Greene, Microstructural evolution during film growth, *J. Vac. Sci. Technol. A Vacuum, Surfaces, Film.* 21 (2003) S117–S128.
- [96] B. Henkel, A. Vahl, O.C. Aktas, T. Strunskus, F. Faupel, Self-organized nanocrack networks: a pathway to enlarge catalytic surface area in sputtered ceramic thin films, showcased for photocatalytic TiO<sub>2</sub>, *Nanotechnology.* 29 (2018) 035703.
- [97] I. Tamiolakis, S. Fountoulaki, N. Vordos, I.N. Lykakis, G.S. Armatas, Mesoporous Au-TiO<sub>2</sub> nanoparticle assemblies as efficient catalysts for the chemoselective reduction of nitro compounds, *J. Mater. Chem. A.* 1 (2013) 14311–14319.
- [98] O. Frank, M. Zupalova, B. Laskova, J. Kürti, J. Koltai, L. Kavan, Raman spectra of titanium dioxide (anatase, rutile) with identified oxygen isotopes (16, 17, 18), *Phys. Chem. Chem. Phys.* 14 (2012) 14567.
- [99] D. Heger, J. Jirkovský, P. Klán, Aggregation of methylene blue in frozen aqueous solutions studied by absorption spectroscopy, *J. Phys. Chem. A.* 109 (2005) 6702–6709.
- [100] R. Ishizaki, R. Katoh, Fast-response humidity-sensing films based on methylene blue aggregates formed on nanoporous semiconductor films, *Chem. Phys. Lett.* 652 (2016) 36–39.
- [101] S.-K. Lee, A. Mills, Novel photochemistry of leuco-Methylene Blue, *Chem. Commun.* (2003) 2366.
- [102] A. Mills, A. Cusick, J. Hepburn, The Kinetics of Semiconductor Photocatalysis in Activity-Indicator Films, *J. Adv. Oxid. Technol.* 12 (2009).
- [103] A.J. Julson, D.F. Ollis, Kinetics of dye decolorization in an air-solid system, *Appl. Catal. B Environ.* 65 (2006) 315–325.
- [104] A. Mills, A. Cusick, J. Hepburn, The Kinetics of Semiconductor Photocatalysis in Activity-Indicator Films, (2009).
- [105] X. Yang, L. Xiong, X. Hu, Photocatalytic reaction and degradation of methylene blue on TiO<sub>2</sub> films in vacuum: an X-ray photoelectron spectroscopy study, *Res Chem Intermed.* 38 (2012) 67–75.
- [106] H. Park, Y. Park, W. Kim, W. Choi, *Journal of Photochemistry and Photobiology C: Photochemistry Reviews* Surface modification of TiO<sub>2</sub> photocatalyst for environmental applications, *J. Photochem. Photobiol. C Photochem. Rev.* 15 (2013) 1–20.
- [107] D. Ollis, Photocatalyzed and photosensitized conversion of organic dyes on porous and non-porous air-solid surfaces: Kinetic models reconsidered, *Appl. Catal. B Environ.* 165 (2015) 111–116.
- [108] K. Doushita, T. Kawahara, Evaluation of photocatalytic activity by dye decomposition, *J. Sol-Gel Sci. Technol.* 22 (2001) 91–98.

- [109] J. Sun, L. Gao, Q. Zhang, Synthesizing and Comparing the Photocatalytic Properties of High Surface Area Rutile and Anatase Titania Nanoparticles, *J. Am. Ceram. Soc.* 86 (2003) 1677–1682.
- [110] A. Houas, Photocatalytic degradation pathway of methylene blue in water, *Appl. Catal. B Environ.* 31 (2001) 145–157.
- [111] A.M. Ahadi, V. Zaporojtchenko, T. Peter, O. Polonskyi, T. Strunskus, F. Faupel, Role of oxygen admixture in stabilizing TiO<sub>x</sub>nanoparticle deposition from a gas aggregation source, *J. Nanoparticle Res.* 15 (2013) 2125.
- [112] O. Polonskyi, T. Peter, A. Mohammad Ahadi, A. Hinz, T. Strunskus, V. Zaporojtchenko, H. Biederman, F. Faupel, Huge increase in gas phase nanoparticle generation by pulsed direct current sputtering in a reactive gas admixture, *Appl. Phys. Lett.* 103 (2013) 033118.
- [113] A.M. Ahadi, V. Zaporojtchenko, T. Peter, O. Polonskyi, T. Strunskus, F. Faupel, Role of oxygen admixture in stabilizing TiO<sub>x</sub> nanoparticle deposition from a gas aggregation source, *J. Nanoparticle Res.* 15 (2013) 2125 (1-11).
- [114] A. Shelemin, O. Kylián, J. Hanuš, A. Choukourov, I. Melnichuk, A. Serov, D. Slavínská, H. Biederman, Preparation of metal oxide nanoparticles by gas aggregation cluster source, *Vacuum.* 120 (2015) 162–169.
- [115] M. Veith, K. Andres, S. Faber, J. Blin, M. Zimmer, Y. Wolf, H. Schnockel, R. Koppe, R. de Masi, S. Hufner, The metastable, glasslike solid-state phase of HAIO and its transformation to Al/Al<sub>2</sub>O<sub>3</sub> using a CO<sub>2</sub> laser, *Eur. J. Inorg. Chem.* (2003) 4387–4393.
- [116] M.Z. Ghorri, S. Veziroglu, B. Henkel, A. Vahl, O. Polonskyi, T. Strunskus, F. Faupel, O.C. Aktas, A comparative study of photocatalysis on highly active columnar TiO<sub>2</sub> nanostructures in-air and in-solution, *Sol. Energy Mater. Sol. Cells.* 178 (2018) 170–178.
- [117] M. Honda, Y. Kumamoto, A. Taguchi, Y. Saito, S. Kawata, Efficient UV photocatalysis assisted by densely distributed aluminum nanoparticles, *J. Phys. D: Appl. Phys.* 48 (2015) 184006.
- [118] L.-B. Xiong, J.-L. Li, B. Yang, Y. Yu, Ti<sup>3+</sup> in the Surface of Titanium Dioxide: Generation, Properties and Photocatalytic Application, *J. Nanomater.* 2012 (2012) 1–13.
- [119] B. Henkel, T. Neubert, S. Zabel, C. Lamprecht, C. Selhuber-Unkel, K. Rätzke, T. Strunskus, M. Vergöhl, F. Faupel, Photocatalytic properties of titania thin films prepared by sputtering versus evaporation and aging of induced oxygen vacancy defects, *Appl. Catal. B Environ.* 180 (2016) 362–371.
- [120] A. Piot, S.K. Earl, C. Ng, S. Dligatch, A. Roberts, T.J. Davis, D.E. Gómez, Collective excitation of plasmonic hot-spots for enhanced hot charge carrier transfer in metal/semiconductor contacts, *Nanoscale.* 7 (2015) 8294–8298.
- [121] T. Saberi Safaei, A. Mepham, X. Zheng, Y. Pang, C.-T. Dinh, M. Liu, D. Sinton, S.O. Kelley, E.H. Sargent, High-Density Nanosharp Microstructures Enable Efficient CO<sub>2</sub> Electroreduction, *Nano Lett.* 16 (2016) 7224–7228.
- [122] V. Zaporojtchenko, J. Zekonyte, A. Biswas, F. Faupel, Controlled growth of nano-size metal clusters on polymers by using VPD method, *Surf. Sci.* 532–535 (2003) 300–305.